Observation of an Excess in the Search for the Standard Model Higgs Boson at ALEPH

by

Jason A. Nielsen

A dissertation submitted in partial fulfillment of
the requirements for the degree of

Doctor of Philosophy
(Physics)

at the
University of Wisconsin-Madison
2001

© Copyright by Jason A. Nielsen 2001

All Rights Reserved

Contents

1 The Standard Model Higgs Boson **1**
1.1 The Standard Model of Electroweak Interactions 2
1.1.1 Fundamental Subatomic Particles 2
1.1.2 Gauge Theory of Electroweak Interactions 3
1.1.3 The Higgs Mechanism 4
1.1.4 Generation of Particle Masses 7
1.2 The Higgs Boson in the Standard Model 8
1.2.1 Constraints on the Higgs Boson Mass 8
1.2.2 Higgs Boson Production at LEP 11
1.2.3 Higgs Boson Decays 12
1.3 Higgs Boson Searches at LEP 12

2 The ALEPH Detector at LEP **17**
2.1 The LEP Collider 17
2.2 The ALEPH Experiment 21
2.2.1 The Vertex Detector 21
2.2.2 The Inner Tracking Chamber 24
2.2.3 The Time Projection Chamber 26
2.2.4 The Electromagnetic Calorimeter 29
2.2.5 The ALEPH Solenoid 30
2.2.6 The Hadron Calorimeter and Muon Chambers 30
2.2.7 The Luminosity Calorimeters 31
2.2.8 The Trigger System 32

3 Analysis Tools **35**
3.1 Event Reconstruction 35
3.2 Monte Carlo Simulation 36
3.3 Electron and Muon Identification 38
3.3.1 Electron Identification 38
3.3.2 Muon Identification 40
3.4 Energy Flow Algorithm 40
3.5 Tagging Jets from b Quarks 42

4 Event Selection for Final States with Four Jets **47**
4.1 Preselection 47
4.2 Selection of Final States with Four b Quarks 48
4.3 Selection of Final States from Two b Quarks 50
4.4 Jet Pairing and Mass Reconstruction 52
4.5 Results from Selection 55
4.6 Discussion of Candidates from the Four-Jet Selection 58

5 Event Selection for Final States with Tau Lepton Pairs **65**
5.1 Preselection 65
5.2 Tau Lepton Identification 66
5.3 Selection of $HZ \to \tau^+\tau^- q\bar{q}$ and $HZ \to b\bar{b}\tau^+\tau^-$ Final States 71
5.4 Overlap between Selections 72
5.5 Results from Selections 74
5.6 Discussion of Tau Pair Candidates 74

6 Event Selections with Neutrino, Electron, or Muon Pairs **79**
6.1 Event Selection for Final States with Neutrino Pairs 79
6.1.1 Preselection 80
6.1.2 Neural Network Selection 81
6.1.3 Results from Selection 82
6.2 Event Selection for Electron or Muon Pairs 84
6.2.1 Lepton Identification 85
6.2.2 Mass Reconstruction 86
6.2.3 Event Selection 87
6.2.4 Results from Selection 88
6.3 Discussion of Electron Pair Candidate 89

7 Statistical Interpretation and Combination of Results **91**
7.1 Confidence Level Calculation using a Test Statistic 91
7.2 The Likelihood Ratio as Test Statistic 92
7.3 Test Statistic Distributions for Event Ensembles 95
7.4 Confidence Integral Calculations 99
7.5 Higgs Boson Mass Limit Calculations 105
7.6 Effects of Statistical and Systematic Uncertainties 109

8 Summary and Outlook **113**
8.1 Combined Results of Higgs Searches at LEP 113
8.2 Future Higgs Boson Searches 115
8.2.1 Higgs Boson Searches at the Tevatron 115
8.2.2 Higgs Boson Searches at the LHC 117
8.3 Conclusion 119

A Confidence Level Calculations using the Fourier Transform 121
A.1 Ensemble Test Statistic Distributions 121
A.2 Combination of Search Channels 125
A.3 Discussion on Systematic Uncertainties 128
A.4 Summary 129

Acknowledgements

I gratefully acknowledge the support and influence of my adviser Sau Lan Wu, who not only labored to provide a stimulating work environment with outstanding resources, but also supplied valuable advice and counsel. Her dedication to research and her uncompromising principles have made a distinct impression on me.

I have benefited greatly from working with the past and present members of the Wisconsin group at CERN: Steve Armstrong, Kyle Cranmer, Pete Elmer, Douglas Ferguson, Yuanning Gao, Saúl González, Tom Greening, Owen Hayes, Hongbo Hu, Shan Jin, Jen Kile, Günter Mamier, Pete McNamara, Jane Nachtman, Yibin Pan, Youssef Saadi, Michael Schmitt, Ian Scott, John Walsh, Jinwei Wu, Xidong Wu, and Haimo Zobernig. The administrative support provided by Beth Peoc'h, Antonella Lofranco, Brian Rathgeber, and Shao Ning was also invaluable.

I am indebted to Karl Berkelman, Douglas Ferguson, Yuanning Gao, and Saúl González for their comments on drafts of this dissertation. Any errors which remain are of course mine alone.

My very special thanks go to my family, who have provided tremendous long-distance support and encouragement throughout the years.

Geneva, Switzerland

July 2001

Chapter 1

The Standard Model Higgs Boson

The mechanism of electroweak symmetry breaking is one of the central mysteries in contemporary particle physics. The standard model of electroweak interactions predicts the existence of a fundamental scalar boson as a remnant of spontaneous symmetry breaking via the Higgs mechanism. Among the many previous experimental searches performed over the past thirty years, none has found any evidence of the Higgs boson. This dissertation reports an observed excess from the most sensitive search yet performed for the standard model Higgs boson.

The basic strategy of the search for the Higgs boson is rather simple. Using the expected characteristics of Higgs boson production and decay, candidate events are selected from the collected data. A certain number of these events are expected even if no Higgs bosons are produced; however, an excess of such candidate events could be evidence for Higgs boson production on top of the background expectation. The search results are subjected to a statistical analysis in an effort to answer just how significant any observed excess may be.

This dissertation is organized into four main parts. The remainder of this chapter emphasizes the central role of the Higgs boson in the standard model. The next

two chapters present the experimental apparatus and the event reconstruction and simulation tools. Then, three chapters detail the searches in the four-jet channel, the tau lepton channels, and the missing-energy and electron and muon channels. Finally, two chapters report the interpretation of the combined search results as an excess and the relationship between this and other searches for the standard model Higgs boson.

1.1 The Standard Model of Electroweak Interactions

Many of the properties of the fundamental subatomic particles and of their interactions are described by a standard model. A product of interplay between theory and experiment, the model has been successful both in interpreting existing experimental data and in predicting new results.

1.1.1 Fundamental Subatomic Particles

The fundamental particles are subject to four forces, each of which is transmitted by one or more gauge bosons. The electromagnetic force, the strong force, and gravity are mediated by massless photons, gluons, and gravitons, respectively. The weak force is mediated by the W^+, W^-, and Z bosons.

Besides the gauge bosons, two other types of fundamental particles exist. The six quarks are the constituents of hadrons. The leptons include the electron, muon, and tau lepton along with their corresponding neutrinos. The properties of the fundamental fermions are summarized in Table 1.1.

The underlying symmetries of the gauge theories which describe particle interactions encourage the unification of the theories. In particular, a model unifying the

quark	charge (e)	mass (GeV/c^2)	lepton	charge (e)	mass (MeV/c^2)
u	+2/3	0.001 to 0.005	e	-1	0.51100
d	−1/3	0.003 to 0.009	ν_e	0	$< 3 \times 10^{-6}$
c	+2/3	1.15 to 1.35	μ	-1	105.66
s	−1/3	0.075 to 0.170	ν_μ	0	< 0.19
t	+2/3	174.3 ± 5.1	τ	-1	1777.0
b	−1/3	4.0 to 4.4	ν_τ	0	< 18.2

Table 1.1: Fundamental properties of the quarks and leptons [1]. The quark masses are uncertain because individual quarks are bound into hadrons. The t quark, however, decays before it hadronizes, so its mass can be measured precisely.

weak and electromagnetic forces proves to have interesting descriptive and predictive powers.

1.1.2 Gauge Theory of Electroweak Interactions

A successful unified electroweak theory must account for the experimental observations of left-handed weak charged-current interactions and for the relative strengths of the weak and electromagnetic forces.

The standard model of electroweak interactions is based on the $\mathrm{SU(2)_L} \otimes \mathrm{U(1)_Y}$ gauge group [2]. The conserved quantum numbers for the two symmetries composing the group are the weak isospin $\mathbf{T}$ and the weak hypercharge Y. Leptons and neutrinos are written as $\mathrm{SU(2)_L}$ doublets and $\mathrm{U(1)_R}$ singlets. The two components of the gauge group imply two corresponding gauge fields – a massless isotriplet $\mathbf{W}_\mu$ and a massless isosinglet B_μ – which operate on fermion fields ψ_L and ψ_R.

The effective Lagrangian for electroweak interactions within this model is

$$\mathcal{L} = -\frac{1}{4}\mathbf{W}^{\mu\nu} \cdot \mathbf{W}_{\mu\nu} - \frac{1}{4}B^{\mu\nu}B_{\mu\nu} + \mathcal{L}_{\text{fermions}},$$

with each separate fermion field, right- or left-handed, adding a term $\bar{\psi} i\gamma^\mu D_\mu \psi$. The covariant derivative D_μ in the lepton terms is defined to be $D_\mu = \partial_\mu + ig\mathbf{W}_\mu \cdot \mathbf{T} + ig'\frac{1}{2}B_\mu Y$, where g and g' give the coupling strengths of the interaction terms [3].

When the coupling terms of the Lagrangian are fully laid out, the orthogonal linear combinations

$$\mathrm{W}_\mu^\pm \equiv \frac{1}{\sqrt{2}}\left(W_\mu^{(1)} \mp W_\mu^{(2)}\right)$$

are identified with the charged W bosons. The remaining fields $W_\mu^{(3)}$ and B_μ form two additional orthogonal linear combinations, one which couples to the neutral currents, and one which couples to electric charge. The combinations are defined through the weak mixing angle $\theta_\mathrm{W} = \arctan(g'/g)$ as

$$\mathrm{Z}_\mu \equiv W_\mu^{(3)} \cos\theta_\mathrm{W} - B_\mu \sin\theta_\mathrm{W}$$
$$\mathrm{A}_\mu \equiv W_\mu^{(3)} \sin\theta_\mathrm{W} + B_\mu \cos\theta_\mathrm{W}$$

and are interpreted as the physical Z boson and the photon, respectively.

Given the underlying SU(2) gauge symmetry, a massive fermion or gauge boson would violate local gauge invariance. Nevertheless, such massive particles are experimentally observed. In the standard model, spontaneous symmetry breaking hides the electroweak symmetry and spawns massive fermions and gauge bosons.

1.1.3 The Higgs Mechanism

Spontaneous symmetry breaking in the standard model [4] requires at least one SU(2) doublet of scalar fields Φ. Two terms are added to the Lagrangian – a $\mathcal{L}_\mathrm{scalar}$ term describing the scalar fields' self-interactions and their interactions with gauge bosons, and a $\mathcal{L}_\mathrm{Yukawa}$ term describing the interaction between the scalar and other fields [5].

The scalar self-interaction term has the form $\mathcal{L}_{\text{scalar}} = (\mathcal{D}^\mu\Phi)^\dagger(\mathcal{D}^\mu\Phi) - V(\Phi^\dagger\Phi)$, where $V(\Phi^\dagger\Phi) = \mu^2(\Phi^\dagger\Phi) + |\lambda|(\Phi^\dagger\Phi)^2$ is identified as a potential. Two cases for the potential V are illustrated in Fig. 1.1. If $\mu^2 \geq 0$, then a unique minimum is located at the point $(\text{Re}(\Phi), \text{Im}(\Phi)) = (0,0)$. If instead $\mu^2 < 0$, then a rotationally symmetric group of minima is spontaneously broken when a vacuum expectation value $\langle\Phi\rangle_0$ is defined

$$\langle\Phi\rangle_0 \equiv \begin{pmatrix} 0 \\ v/\sqrt{2} \end{pmatrix} = \begin{pmatrix} 0 \\ \sqrt{\mu^2/2\lambda} \end{pmatrix}.$$

A restoring force acts along the radial direction, but the rotational symmetry of the potential implies zero-energy excitations in the form of Goldstone bosons [6]. In the context of a classical perturbation theory and using a suitable gauge, the scalar term in the Lagrangian for small oscillations about this shifted minimum becomes

$$\mathcal{L}_{\text{scalar}} = \frac{1}{2}(\partial\text{H})^2 + \frac{g^2}{4}\text{W}^+\text{W}^-(v+\text{H})^2 + \frac{g^2+g'^2}{8}\text{ZZ}(v+\text{H})^2 - V\left[\frac{1}{2}(v+\text{H})^2\right],$$

where the gauge fields are the same as for the model with unbroken symmetry. Clearly, two of the terms define non-zero masses for the weak bosons, namely

$$m_{\text{W}^\pm} = \frac{gv}{2} \quad \text{and} \quad m_{\text{Z}} = \frac{\sqrt{g^2+g'^2}v}{2} = m_{\text{W}^\pm}\left(1+\tan^2\theta_{\text{W}}\right),$$

but the photon remains massless. This set of electroweak gauge bosons accurately reproduces the experimentally observed spectrum; however, the Higgs mechanism leaves behind one extra massive scalar boson, the Higgs boson.

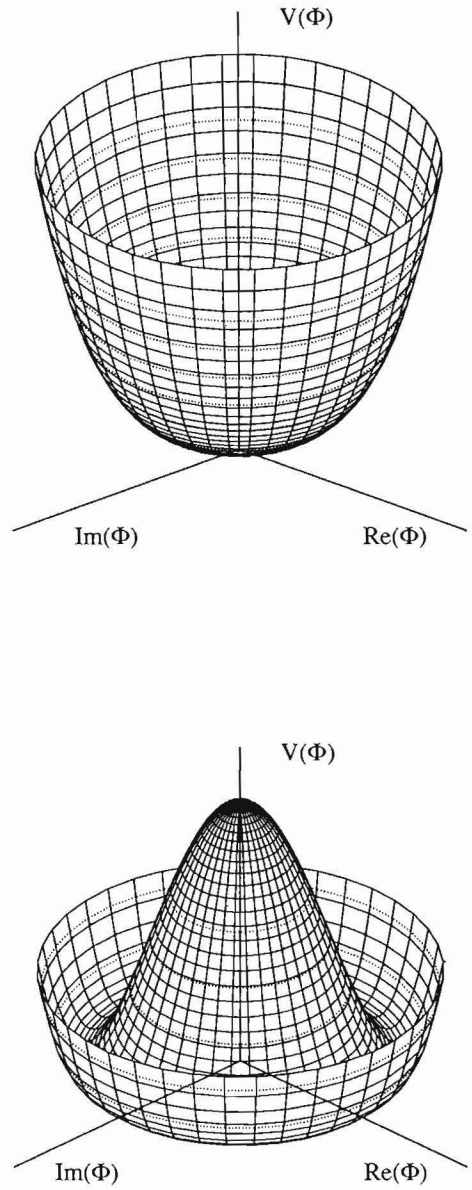

Figure 1.1: Schematic representation of the classical scalar Higgs potential $V(\Phi)$, for non-negative values of μ^2 (at top), and for negative values of μ^2 (at bottom).

1.1.4 Generation of Particle Masses

With the introduction of the Higgs scalar fields, the Lagrangian gains Yukawa interaction terms whose effect is to generate the fundamental fermion masses. For the first generation of leptons, such a term takes the form

$$\mathcal{L}_{\text{Yukawa}} = -G_{\text{e}} \left[\overline{\text{e}_{\text{R}}} \left(\Phi^{\dagger} \ell_{\text{L}} \right) + \left(\overline{\ell_{\text{R}}} \Phi \right) \text{e}_{\text{R}} \right] ,$$

where G_{e} is defined such that $m_{\text{e}} = G_{\text{e}} v / \sqrt{2}$. Not only does the interaction with the Higgs field generate the electron mass, but the coupling to the Higgs boson itself is proportional to the mass. Each generation of leptons contributes its own Yukawa term with a different arbitrary coupling constant G_{ℓ}. As a result, the lepton masses are free parameters with no prediction in the standard model.

The fermion fields identified with the quarks are grouped into three generations of left-handed doublets and right-handed singlets. The quark masses are then generated in much the same way as the lepton masses, but inter-generational couplings between quarks are allowed, as observed experimentally. In practice this quark mixing is attributed exclusively to the "down-type" quarks in each isospin doublet so that the doublets have the form

$$\begin{pmatrix} u \\ d' \end{pmatrix}_{\text{L}} , \begin{pmatrix} c \\ s' \end{pmatrix}_{\text{L}} , \begin{pmatrix} t \\ b' \end{pmatrix}_{\text{L}}$$

$$\text{where} \quad \begin{pmatrix} d' \\ s' \\ b' \end{pmatrix}_{\text{L}} = V \begin{pmatrix} d \\ s \\ b \end{pmatrix}_{\text{L}} .$$

The Cabbibo-Kobayashi-Maskawa 3×3 complex mixing matrix V consists of four physically independent parameters which are not predicted by the standard model

but can be measured experimentally [7, 8].

It is important to note that the Yukawa interaction terms in the Lagrangian describe mass generation for the fundamental fermions only. The masses of bound quark states, in particular, are dominated by the effects of the strong interaction. In this sense, most of the mass in everyday life is not described by the electroweak standard model, but rather by quantum chromodynamics, the gauge theory of the strong interaction.

1.2 The Higgs Boson in the Standard Model

The interactions of the Higgs boson with other fundamental particles can be described as a function of a single free parameter in the standard model, usually taken to be the Higgs boson mass. Such calculations not only help interpret experimental results, but also provide guidelines for developing Higgs boson searches.

1.2.1 Constraints on the Higgs Boson Mass

Although the Higgs boson mass is a free parameter in the standard model, its range is not completely unknown. Certain theoretical self-consistency arguments provide upper bounds on the Higgs boson mass, and global fits to electroweak precision measurements can constrain the allowed mass range, always assuming the validity of the standard model. Unsuccessful experimental searches also exclude Higgs boson mass hypotheses based on the calculated production cross section.

Various consistency requirements imply some phenomenological constraints on the Higgs boson mass. One analysis considers the s-wave amplitudes in scattering of Higgs bosons and longitudinally polarized gauge bosons [9]. If the partial wave amplitudes calculated from tree-level diagrams are required to satisfy unitarity, then

the Higgs boson mass must be less than $1\,\mathrm{TeV}/c^2$.

Additional hints to the Higgs boson mass come from electroweak processes that are sensitive to the masses of particles which contribute to radiative corrections through loop diagrams. These masses can be constrained by comparing the experimental measurements with the expectations for a given mass. A notable success of this method was the correct prediction of the top quark mass before the top quark itself had been experimentally observed [10]. Whereas the loop corrections depend quadratically on the top quark mass, they depend only logarithmically on the Higgs boson mass [11]; nevertheless, the increased precision of electroweak measurements makes it possible to constrain the Higgs boson mass. The LEP Electroweak Working Group has used these measurements as inputs to a global fit for the Higgs boson mass, and the results, shown in Fig. 1.2, favor a Higgs boson mass of $98^{+58}_{-38}\,\mathrm{GeV}/c^2$ while excluding masses above $212\,\mathrm{GeV}/c^2$ at 95% confidence level [12].

Previous Higgs boson searches at LEP provide the most stringent experimental limits on the Higgs boson mass. Results from the four LEP experiments have been combined by the LEP Higgs Working Group using data from e^+e^- collisions with center-of-mass energies of up to 202 GeV. Higgs boson masses less than $107.9\,\mathrm{GeV}/c^2$ are excluded at 95% confidence level, based on negative results from searches in many final states [14].

In addition, searches for the Higgs boson in $p\bar{p}$ collisions at the Tevatron collider place weak limits on the production cross section at larger masses. The CDF collaboration sets upper limits on $\sigma(p\bar{p} \to \mathrm{WH,ZH}) \times \mathrm{BR}(\mathrm{H} \to b\bar{b})$ of 7.4 pb for a Higgs boson mass of $130\,\mathrm{GeV}/c^2$, compared to the standard model prediction of 0.12 pb [15, 16].

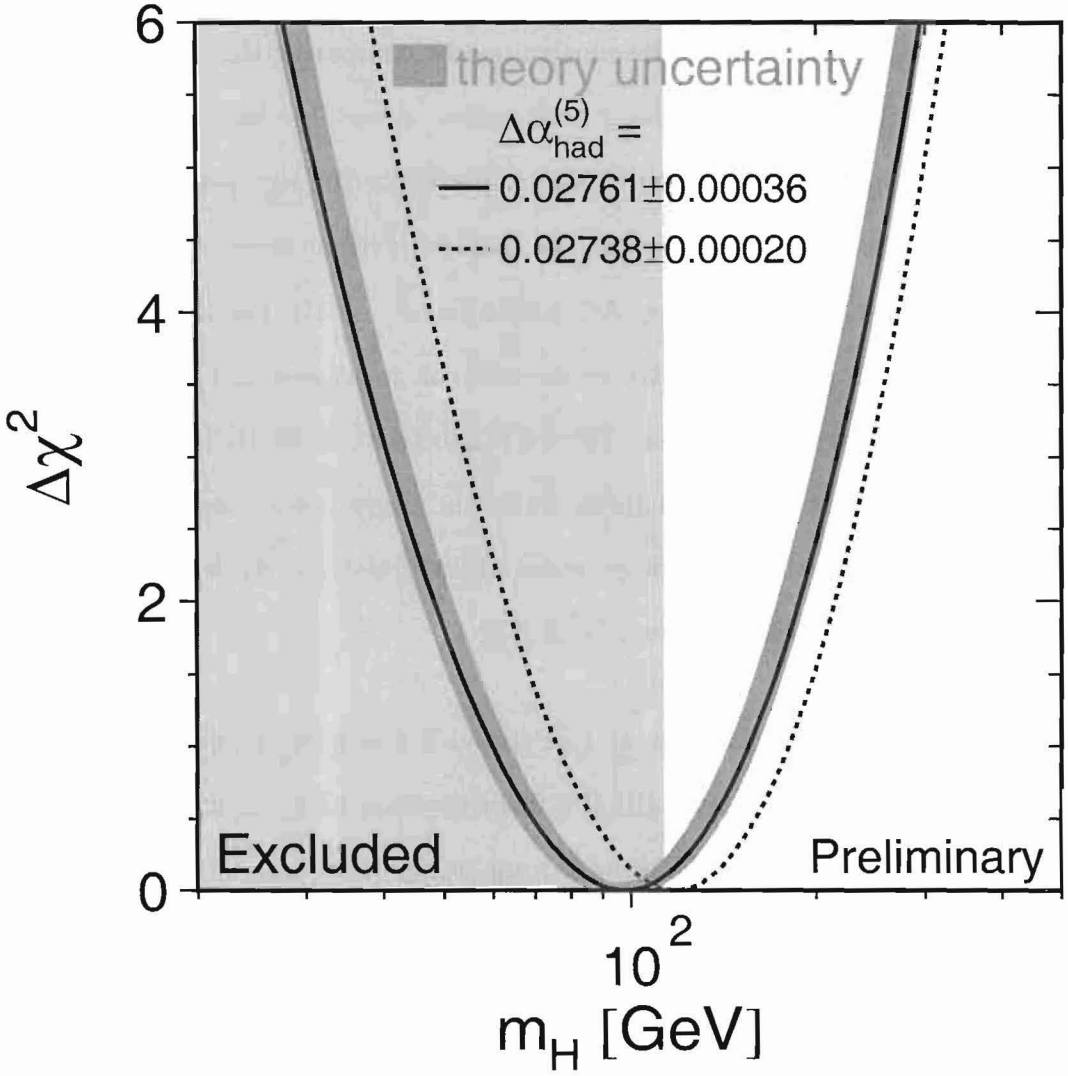

Figure 1.2: The χ^2 difference, relative to the minimum χ^2, from the global fit of experimental data to the standard model. The favored Higgs boson mass values are those within one unit of $\Delta\chi^2$ from the minimum $\Delta\chi^2$ at $m_{\mathrm{H}} = 98\,\mathrm{GeV}/c^2$. The input $\Delta\alpha_{\mathrm{had}}^{(5)}$ is taken from Ref. [13].

1.2.2 Higgs Boson Production at LEP

The light electron mass implies a small cross section for direct Higgs production in e^+e^- annihilations at LEP. Instead, the most promising production mechanisms for Higgs boson production at LEP2 energies ($130 < \sqrt{s} < 210$) are *Higgs-strahlung* and weak boson fusion. The large ZZH coupling allows the Higgs boson to be radiated from a virtual Z boson. This *Higgs-strahlung* ("Higgs radiation") diagram (Fig. 1.3) results in associated HZ production with the final Z boson close to its mass shell [17]. For a

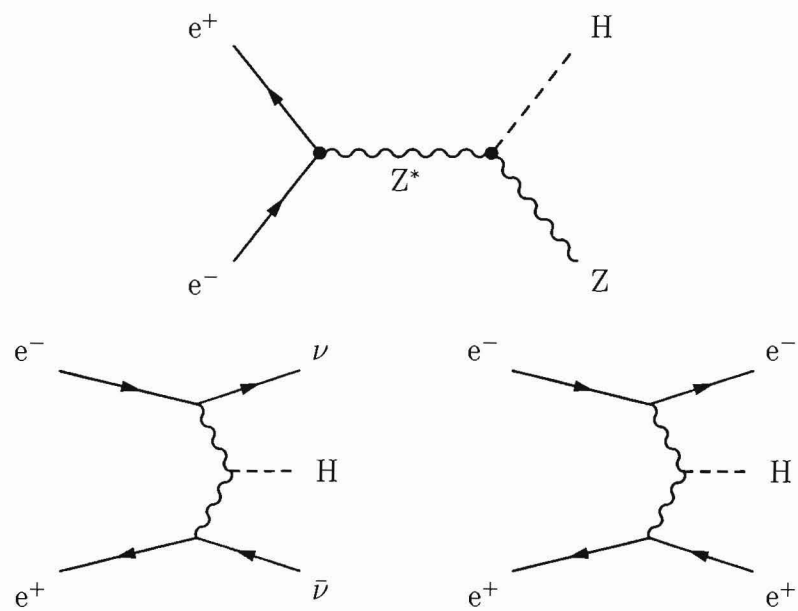

Figure 1.3: Feynman diagrams for Higgs boson production in e^+e^- collisions. The Higgs-strahlung diagram is shown on top, and the WW- and ZZ-fusion diagrams are shown on bottom left and bottom right, respectively.

given $\sqrt{s}$, the HZ production cross section drops sharply for $m_H > \sqrt{s} - m_Z$, beyond which mass the final state Z boson would be off-shell. At and above this threshold, the WW- and ZZ-fusion diagrams contribute a significant fraction of the total Higgs boson production cross section [18]. The total production cross section for $\sqrt{s} = 206\,\text{GeV}$ (the luminosity-weighted LEP average in 2000) is shown in Fig. 1.4. At this center-

of-mass energy, the kinematic threshold in the HZ diagram is $m_{\mathrm{h}} = 115\,\mathrm{GeV}/c^2$.

1.2.3 Higgs Boson Decays

The partial decay widths of the Higgs boson from tree-level diagrams are easily calculated as a function of the Higgs boson mass [9]. The partial decay width to fermions is

$$\Gamma(\mathrm{H} \to f\bar{f}) = \frac{G_F m_f^2 m_{\mathrm{H}}}{4\pi\sqrt{2}} N_c \left(1 - \frac{4m_f^2}{m_{\mathrm{H}}^2}\right)^{3/2},$$

where N_c is 1 for leptons and 3 for quarks. The partial width is evidently proportional to the square of the fermion mass when $m_{\mathrm{H}} \gg m_f$. Additional terms with quark mass and electroweak corrections are collected in Ref. [20] and are used to calculate the Higgs boson branching fractions shown in Fig. 1.5. The total decay width of a $115\,\mathrm{GeV}/c^2$ Higgs boson is $3\,\mathrm{MeV}/c^2$, well below the experimental resolution.

1.3 Higgs Boson Searches at LEP

Based on the dominant production and decay modes, the Higgs boson searches at LEP focus on four distinctive final state topologies or channels, which follow in decreasing order of analyzing power:

- four-jet channel: $(\mathrm{H} \to \mathrm{b\bar{b}})$, $(\mathrm{Z} \to \mathrm{q\bar{q}})$;
- missing-energy channel: $(\mathrm{H} \to \mathrm{b\bar{b}})$, $(\mathrm{Z} \to \nu\bar{\nu})$;
- electron and muon channels: $(\mathrm{H} \to \mathrm{b\bar{b}}, \tau^+\tau^-)$, $(\mathrm{Z} \to \mathrm{e^+e^-}, \mu^+\mu^-)$;
- tau lepton channels: $(\mathrm{H} \to \mathrm{b\bar{b}})$, $(\mathrm{Z} \to \tau^+\tau^-)$; $(\mathrm{H} \to \tau^+\tau^-)$, $(\mathrm{Z} \to \mathrm{q\bar{q}})$.

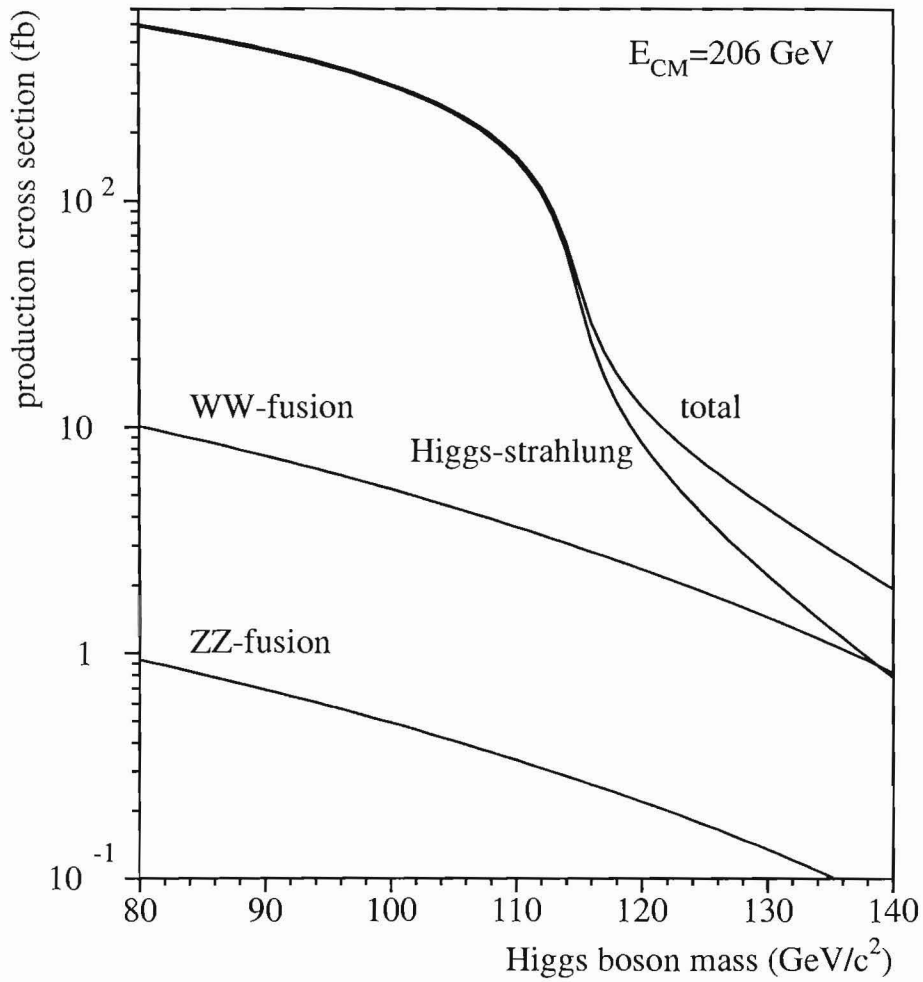

Figure 1.4: Higgs production cross sections for the three diagrams individually and combined. The results are calculated for a center-of-mass energy of 206 GeV using subroutines in the HZHA03 generator library [19]. The total cross section includes the effects of interference between the diagrams.

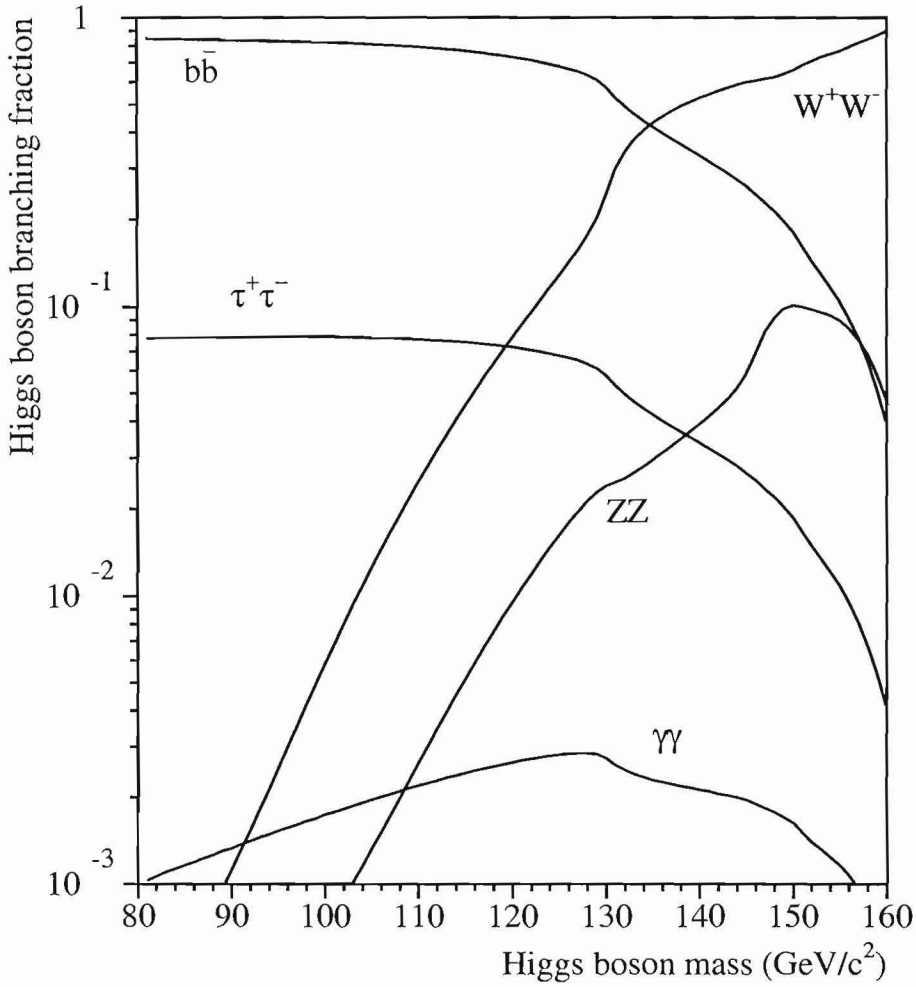

Figure 1.5: Branching fractions for Higgs boson decay modes used in LEP2 searches. The plotted values were calculated using routines in the the HZHA03 generator library.

These topologies account for more than 90% of possible final states from HZ production for a Higgs boson mass of $115\,\mathrm{GeV}/c^2$. The missing-energy channel and the electron channel are also sensitive to Higgs production via the WW- and ZZ-fusion diagrams, respectively.

In general, each analysis begins with a preselection which removes broad classes of background events based on simple kinematic requirements. A stricter final selection follows, based either on tighter and more complex cuts or on an artificial neural network trained to distinguish signal events from background events. This final selection is applied in parallel to experimental data and a simulation; the expected results from the simulation can then be directly compared to the results from experiment.

Chapter 2

The ALEPH Detector at LEP

The experimental apparatus used to collect data for this search can be described in two parts – the LEP collider, which provides high energy particle beams, and the ALEPH detector, which digitizes the resulting annihilations.

2.1 The LEP Collider

The Large Electron Positron collider (LEP) at CERN accelerates and collides high energy counter-rotating electron and positron beams. Having operated with beam energies up to 105 GeV/c^2 in 2000, it is the highest energy e^+e^- collider in the world. Its high center-of-mass energy and clean annihilations make LEP an invaluable machine for new particle searches.

Electrons and positrons are accelerated to high energy in a chain of machines, shown in Fig. 2.1. The LEP Injection Linac (LIL), a two-stage fast-cycling linac, accelerates electrons and positrons to 600 MeV at 100 Hz. The first stage accelerates electrons to 200 MeV. If positrons are to be produced, a tungsten target placed in the beam generates positrons, which are then accelerated to 600 MeV. If elec-

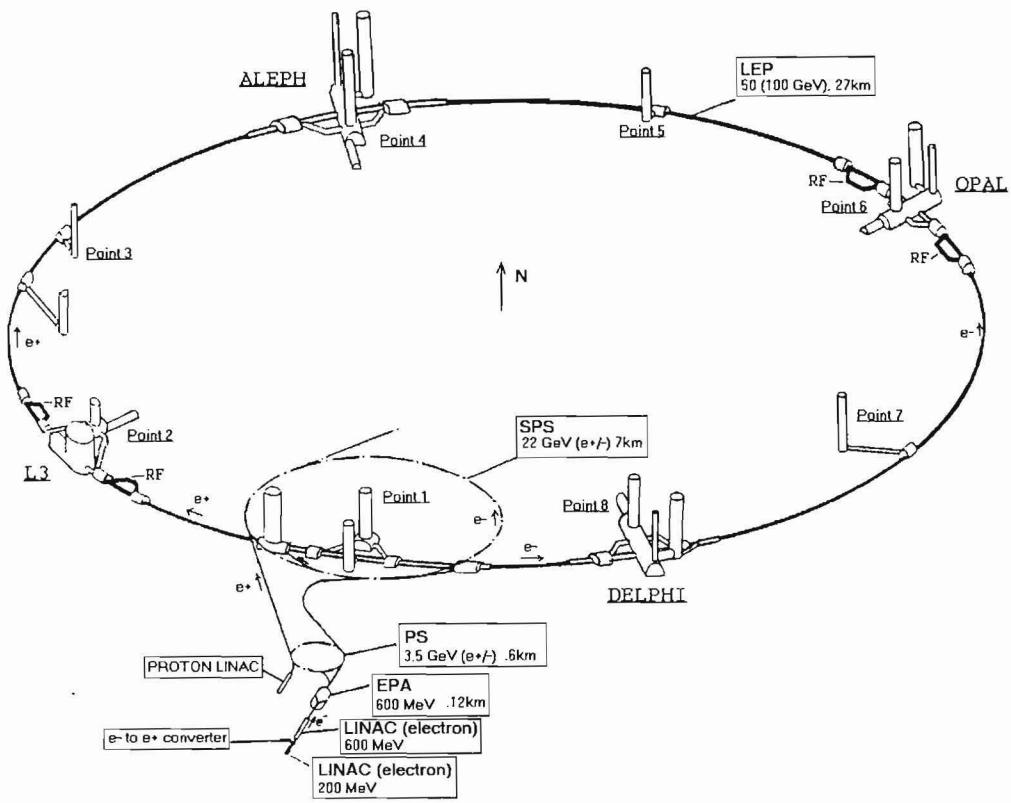

Figure 2.1: The CERN accelerator chain and the four LEP detectors. Electrons and positrons are accumulated and accelerated in several stages before being injected and ramped to final beam energies of up to 105 GeV in LEP.

trons are to be produced, the target is removed, and the electrons are accelerated by 400 MeV to reach 600 MeV. The particles produced by LIL are buffered in the Electron-Positron Accumulator (EPA), a racetrack-shaped storage ring. The EPA also allows positrons, which are slowly produced in LIL, to be accumulated until the positron current matches the electron current. Electrons and positrons are extracted in a 0.8 Hz cycle to the Proton Synchrotron (PS), a 200 meter diameter synchrotron which accelerates the particles to an energy of 3.5 GeV. The last accelerator in the injection chain is the Super Proton Synchrotron (SPS) which accelerates electrons and positrons to 20 GeV before they are injected into LEP.

LEP itself is a synchrotron 27 km in circumference. Dipole magnets in eight arcs bend the electron and positron beams; quadrupole magnets in the arcs and straight sections focus the beams to interaction points; sextupole magnets correct for machine chromaticity. To bring the beams to a fine focus before collision at the interaction points midway through the straight sections, special superconducting quadrupole magnets are installed on both sides of each detector. By squeezing the transverse dimensions of the colliding beams, the luminosity – and therefore the event rate – at the interaction points is increased.

The rate for a reaction is the product of luminosity and cross section. The cross section of a reaction is based on the particles and forces involved in the reaction as well as the kinematic properties of the reaction. The luminosity at LEP is defined as $L = N^2 k f / 4\pi\sigma_x\sigma_y$ where N is the number of particles, f is the revolution frequency, and σ_x and σ_y are the r.m.s. radii of the ellipsoidal beam envelope at the collision point.

Throughout the LEP runs in 2000, electrons and positrons were grouped into four bunches for each beam. These bunches were injected into 4+4 radiofrequency (RF) buckets from a total of 31,320 created by the LEP RF system. The LEP beams,

typically with 3 mA current, were built up through repeated injection from the SPS into the same 8 RF buckets.

The LEP beam energy is derived from measurements of the dipole bending fields by nuclear magnetic resonance (NMR) probes in sixteen of the 3200 LEP dipoles [21]. The beam energy is then directly proportional to the integrated magnetic field around the LEP ring. This method has been calibrated and cross-checked with another method making use of resonant beam depolarization (RD). If the average spin vector of a beam of polarized electrons or positrons is perturbed coherently with the natural spin precession, the beam becomes depolarized. By finding the spin precession frequency, the RD method measures the beam energy with a precision better than 1 MeV, but fails for beam energies above 55 GeV due to difficulties in producing sufficiently polarized beams. Nevertheless, the RD method is used to calibrate the NMR probe measurement for beam energies between 41 and 56 GeV [22]. The LEP beam energy has been determined with a precision of 25 MeV for data taken in 2000 [23].

A new technique was used to increase the LEP energy in discrete steps throughout a typical 2-hour fill, while still maintaining a one-klystron margin. (If one klystron tripped, the remaining RF power would be just sufficient to keep the beams in their orbit.) Instead of ramping the beams directly to a final energy, a series of miniramps were employed to accelerate the beams. As the current in the machine decreased during a fill, the load on the superconducting RF cavities decreased. Increasing the energy of the lower current beams still allowed the machine to operate with the one-klystron safety margin. At the end of fill, instead of being dumped immediately, the beams were ramped to the maximum energy (without margin) and remained there until a klystron tripped and the beams were lost. To avoid the confusion of varying energies within a single run, a new ALEPH run began with each change in the LEP energy. In 2000, ALEPH collected data equivalent to 217 pb^{-1} integrated

luminosity, the bulk of which were collected at center-of-mass energies between 204.5 and 207.5 GeV, as shown in Fig. 2.2.

Electron beams at LEP energies circulate near the energy limit beyond which the synchrotron radiation losses are impractically large. (Electrons in LEP already lose about 2 GeV per revolution due to this effect.) Future lepton accelerators will probably use either a linear geometry or more massive leptons (*e.g.*, muons) to achieve higher center-of-mass energies [24, 25, 26].

2.2 The ALEPH Experiment

The ALEPH detector (**A**pparatus for **LE**P **PH**ysics) is one of four large general-purpose electronic detectors installed on LEP. Situated 143 m below ground, it is well shielded from cosmic radiation of all but the highest energies.

The ALEPH detector is in fact a series of coaxial subdetectors with the z axis along the beam axis. The inner subdetectors provide precise particle tracking. A superconducting solenoid generates an axial magnetic field which makes possible accurate measurements of charged particle momenta. The outer subdetectors measure particle energies and identify penetrating muons. The detector ensemble has been designed to provide solid angle coverage of nearly 4π sr and to be hermetic to energy produced in e^+e^- collisions.

The sections that follow detail the unique properties and function of each subdetector in ALEPH, emphasizing its utility for Higgs boson searches.

2.2.1 The Vertex Detector

A detector to identify and measure short-lived decay products of the Higgs boson and other particles should be placed close to the production point. Intervening material

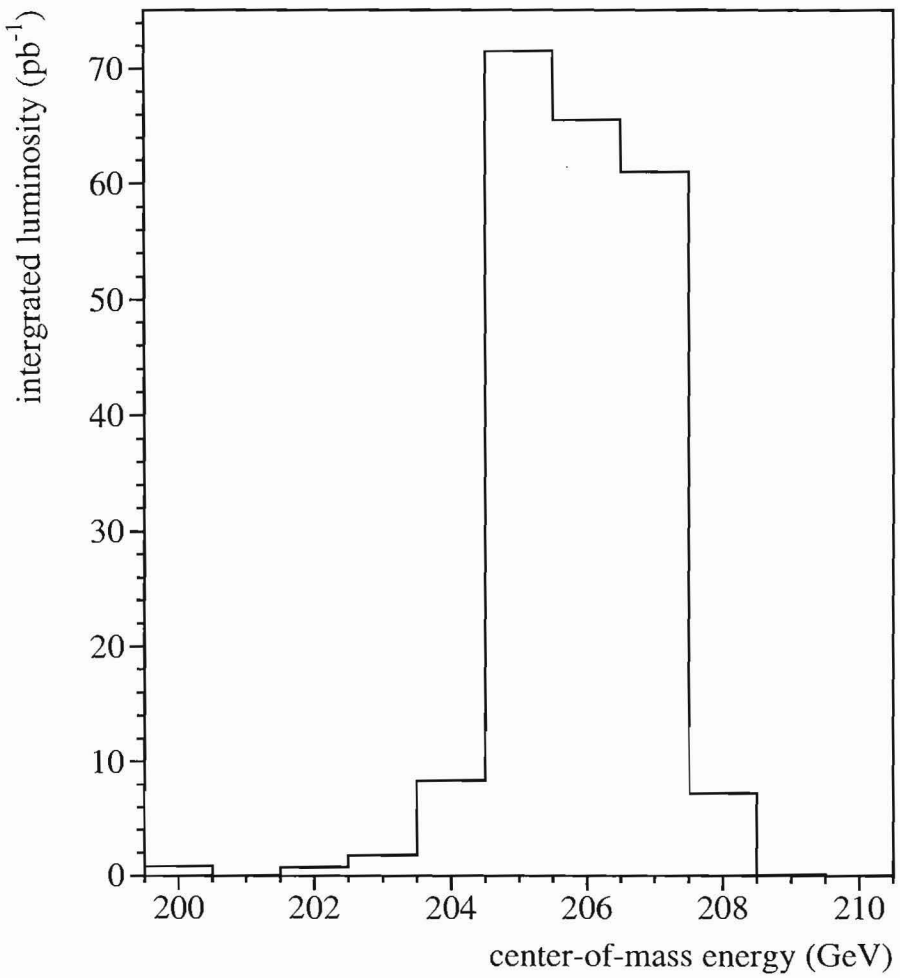

Figure 2.2: Integrated luminosity collected with the ALEPH detector in 2000. The luminosity-weighted center-of-mass energy is 205.9 GeV.

should be minimized to reduce multiple scattering of the particles to be detected. In ALEPH, a silicon vertex detector (VDET), located just outside the beryllium beam pipe, provides three-dimensional point constraints on each charged particle track.

Charged particles traversing a reverse-biased p-n junction induce electron-hole pair formation. The electrons and holes are swept by the effective bias potential to collector plates, where charge is measured as evidence of the particle's passage. The ALEPH VDET features a double-sided microstrip readout, in which the electrons and holes are collected by orthogonal strips on both faces of a wafer [27]. With such a readout, the passage of a charged particle can be measured with precision in both $r - \phi$ and z coordinates.

Two cylindrical planes of silicon wafers are arranged in pinwheels with average radii 6.3 and 11.0 cm (Fig. 2.3). To ensure tracking coverage at low angles, the planes

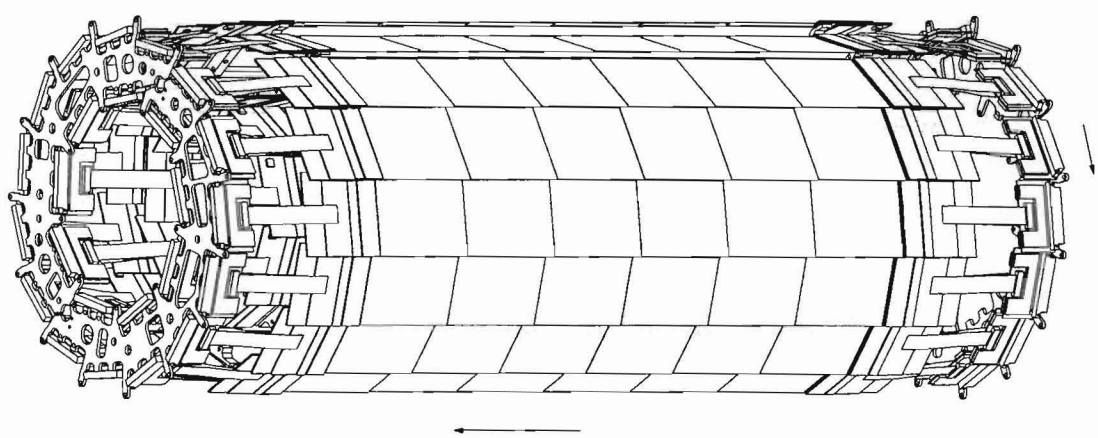

Figure 2.3: The ALEPH silicon vertex detector. The outstanding point resolution on the silicon planes at small radii makes it possible to reconstruct vertices from the decay products of short-lived particles.

extend 20 cm in z on both sides of the interaction point. The 300 μm thick n-type silicon wafers are biased to form a depletion region extending the entire thickness

of the wafer. Strips that measure the $r - \phi$ coordinate are $p+$-doped implants with a pitch of $50\,\mu$m. The implants on this "junction side" are isolated naturally when the depletion region is formed. Strips that measure the z coordinate are $n+$-doped implants with a pitch of $100\,\mu$m. The implants on this "ohmic side" are separated by $p+$ blocking strips which interrupt the electron accumulation layer at the silicon-oxide interface.

Signals are carried from the z strips to the readout electronics via a flexible circuit glued to the wafers. The readout electronics, including charge amplifiers and coupling capacitors, are mounted at the ends of the cylinders to reduce the amount of material in the active detection region. A support structure of carbon fiber and Kevlar ensures the rigidity and stability of the VDET.

Tracks of particles passing through overlapping wafers are over-constrained, and the extra constraints are used to determine the point resolution of the VDET for single tracks (Fig. 2.4). The VDET's precise point resolution at small radii is indispensable for the identification of short-lived decay particles from the Higgs boson.

2.2.2 The Inner Tracking Chamber

The ALEPH inner tracking chamber (ITC) serves two purposes. It provides three-dimensional track points with radii between 12.8 cm and 28.8 cm, and it provides the only tracking information used in the ALEPH Level 1 trigger decision.

The ITC is a conventional cylindrical drift chamber with eight layers of small drift cells. In the hexagonal cell structure, each sense wire is surrounded by four field-shaping wires. Cells in adjacent layers are offset to remove the left-right ambiguity inherent in most drift chambers.

Position measurements in $r - \phi$ depend on the precise knowledge of the electron

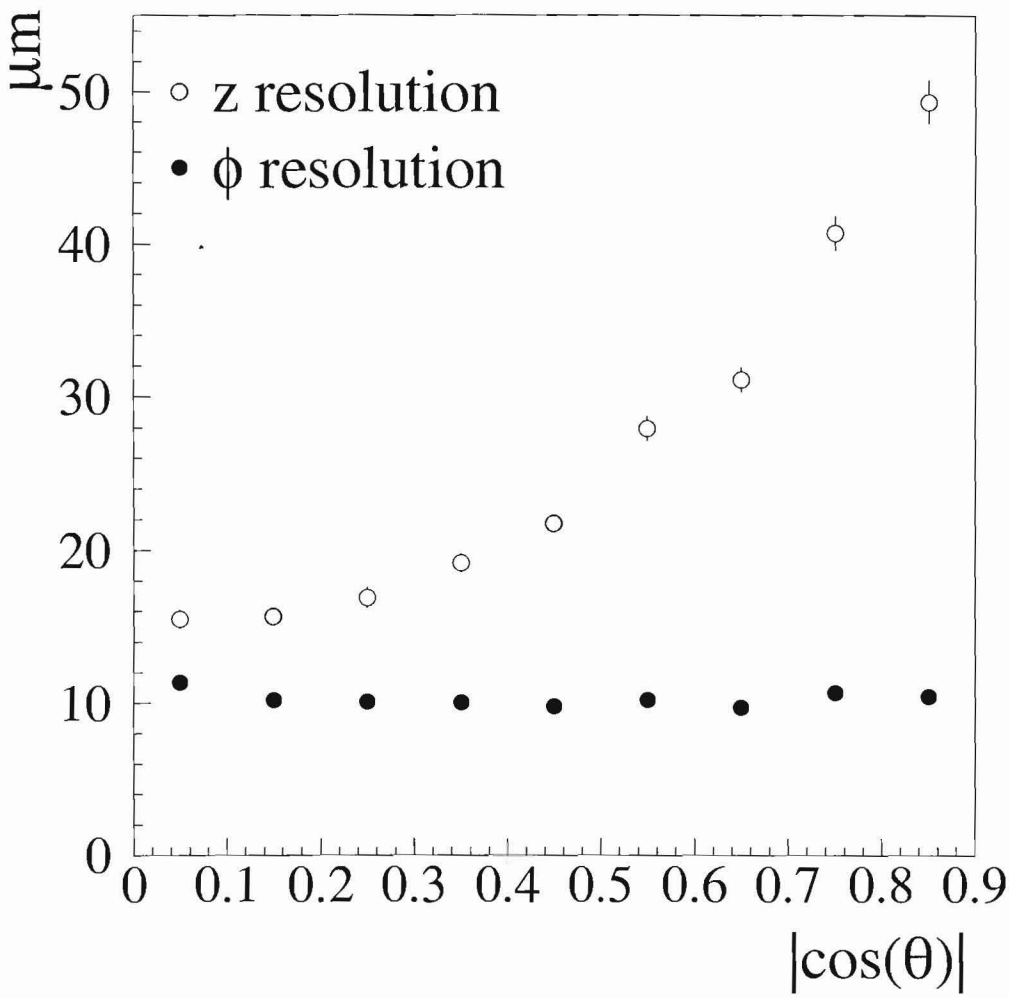

Figure 2.4: ALEPH VDET point resolution as a function of $|\cos\theta|$. At low polar angles, the resolution in z is limited by δ-ray production as particles traverse a longer path through the silicon bulk [28].

drift velocity, which is measured *in situ* in the ALEPH magnetic field. Position measurements in z depend on accurate timing of the pulse arrival at the two ends of the sense wire. By utilizing the time difference, the z coordinate can be calculated, albeit with a relatively poor precision. The position resolution in $r - \phi$ is $150\,\mu$m, and the resolution in z, averaged over the 2 m long wires, is 5 cm [29].

Fast readout due to the small 1 cm diameter cells enables the ITC to deliver its trigger decision in $2\,\mu$s. The track points from the ITC also allow tracks from the main tracking chamber to be extrapolated to match VDET hits at small radii.

2.2.3 The Time Projection Chamber

The main tracking chamber of ALEPH is a large annular gas volume with planar multiwire proportional chamber endplates (Fig. 2.5). In this time projection chamber (TPC), the passage of a charged particle liberates ionization electrons which drift up to 2.2 m along an axial electric field to the endplates. As a consequence of the relatively slow drift velocity, the z coordinate of the passing particle can be measured more precisely than with the ITC.

Each TPC endplate is divided into 18 sectors. Six inner sectors (*Kind*) are rotated with respect to 12 outer sectors (six *Mann*, six *Weib*) to eliminate uninstrumented cracks in ϕ. In each sector, three planes of wire grids are stretched across a plane of segmented copper pads arranged in 21 concentric arcs. The gating grid field blocks avalanche cations from entering the active volume, and the cathode grid defines the ground of the electric drift field. Measurements of a particle's energy loss by ionization ($\mathrm{d}E/\mathrm{d}x$) are derived from the pulse heights measured on the sense wire grid. Up to 21 position measurements per track are derived from the pad coordinates of induced signals.

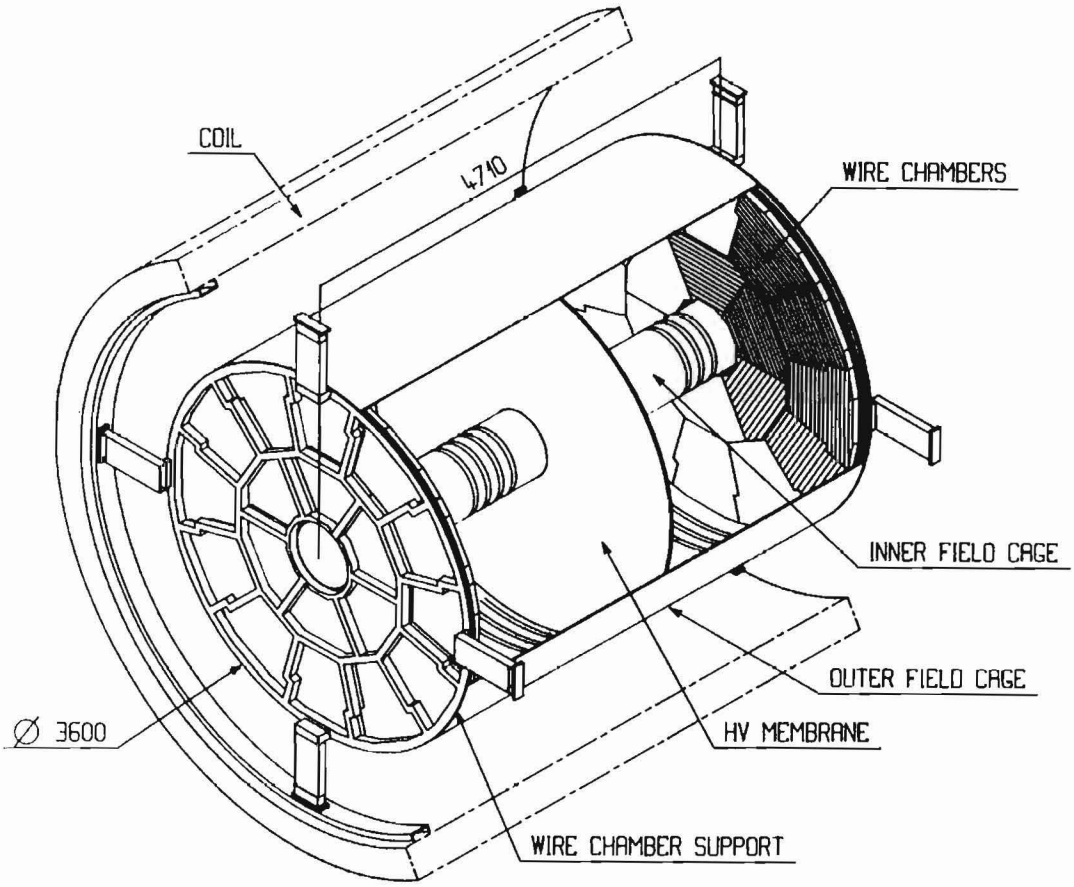

Figure 2.5: The structure of the time projection chamber, ALEPH's main tracking subdetector.

Electrode rings on the inner and outer walls form a TPC field cage which shapes the applied drift field. A conductive central membrane held at a high voltage of $-26\,\mathrm{kV}$ defines one end of the field, and the cathode grid of the endplate wire chambers defines the other end. In an ideal TPC with parallel electric and magnetic fields, the electron drift velocity field would be $\vec{v_\mathrm{d}} = \mu\vec{E}$, but small inhomogeneities cause higher-order corrections which are accounted for during reconstruction. During data-taking, the drift velocity is measured *in situ* by firing ionizing lasers and measuring the arrival time of the resulting ionization electrons. A typical drift velocity during 2000 was $5.2\,\mathrm{cm}/\mu\mathrm{s}$, but this was subject to slight variations of the gas pressure inside the TPC.

The electron multiplication avalanche at the sense wires allows a small amount of original ionization charge to be detected. Unfortunately, the same avalanche creates an equal number of cations which tend to drift backwards along the electric field into the active volume of the TPC. This problem is solved by a gating grid which synchronously generates an electric dipole field to trap the cations. About $2\,\mu\mathrm{s}$ before the beam crossing, the gating grid is set to $-66\,\mathrm{V}$, rendering it transparent to drifting electrons. After readout is complete, the gate is closed by applying $\pm 100\,\mathrm{V}$ to alternate wires, thus creating the dipole field. A special circuit opens and closes the gate with matched pulses which avoid induced signals on the sense wires.

The charge collected on wires and pads is measured with flash ADC's which digitize the analog charge in 512 time buckets of 88 ns each. Periodic calibration of the ADC's guarantees a linear and uniform response to the input charge. Each ADC has four voltage reference points along its divider chain. During calibration, the field wires of the sector are pulsed at different amplitudes to induce signals on the sense wires, and the resulting ADC outputs are measured. The reference point voltages are adjusted to minimize a χ^2 representing the deviation from an optimal linear response.

This online calibration method avoids the need for an offline correction database.

The long lever arm and the fine spatial resolution of the TPC precisely measure the transverse momentum of charged particles curving in the magnetic field. The three tracking detectors combined achieve a momentum resolution of $\Delta p/p^2 = 0.6 \times 10^{-3}(\mathrm{GeV}/c)^{-1}$ [30], and the $\mathrm{d}E/\mathrm{d}x$ measurement from the TPC is used to identify low-momentum leptons.

2.2.4 The Electromagnetic Calorimeter

The electromagnetic calorimeter (ECAL) is a sampling calorimeter with 45 interleaved lead sheets and wire chambers. In a sampling calorimeter, the energy of an incoming particle is proportional to the number of charged tracks produced via electromagnetic showers in the absorber [31].

Long aluminum extrusions define individual cells, each of which contains a single sense wire at high voltage. Particles crossing the cell create ionization avalanches on the wires, which are read out capacitively on finely segmented cathode pads.

Stacks of cathode pads are connected in a projective tower geometry pointing toward the interaction point. Each tower is divided longitudinally into three "stories" of 4, 9, and 9 radiation lengths. The high degree of granularity – the total solid angle of a tower of single pads is approximately 1° – allows two close particles to be resolved.

The wire chambers are operated in proportional mode with a $XeCO_2$ gas, and the gas gain is actively monitored using a ^{55}Fe source. Electrons produced in the wire avalanche are scattered by the heavy xenon nuclei into the cell walls, thereby avoiding continuous ionization in the active planes.

The ECAL provides a measure of energy for neutral particles which interact electromagnetically. Because the electromagnetic shower is a statistical process, the en-

ergy resolution depends on the energy as

$$\frac{\sigma(E)}{E} = \frac{0.18}{\sqrt{E(\mathrm{GeV})}} + 0.01$$

for electrons. The ECAL also allows efficient and reliable identification of electrons and photons in Higgs searches. The calorimeter granularity is important for determining the energy deposition profile of the shower in both longitudinal and transverse directions.

2.2.5 The ALEPH Solenoid

The central tracking detectors and the ECAL are immersed in a 1.5 T magnetic field coaxial with the beam line. This field is generated by a superconducting solenoid of NbTi wire embedded in an aluminum matrix. The return flux is shaped by an yoke of stacked iron plates which also serve as absorber material for the hadron calorimeter. The ALEPH solenoid is one of the largest in the world, with 136 MJ of stored energy at 4967 A current.

Because the radius of curvature of a charged track is inversely proportional to the magnetic field strength, momenta transverse to the axial field are precisely measured in ALEPH. To ensure the accuracy of the transverse momentum measurement, the magnetic field has been mapped using Hall plates, and the small deviations ($< 0.2\%$) of the main field component are corrected for during reconstruction [29].

2.2.6 The Hadron Calorimeter and Muon Chambers

The iron structure of the return yoke is used as the absorbing material for the hadronic sampling calorimeter (HCAL). It also serves as a filter for muons, which are detected

in muon chambers outside the HCAL.

The HCAL modules are stacks of iron plates and streamer tubes. A graphite-coated plastic comb extrusion defines cells, each of which contains a single sense wire. The energy in a cell is derived from induced signals on pads, which are further connected to form projective towers as in the ECAL. The number of streamers and the average streamer charge are used to calculate the collected energy. The average streamer charge is calibrated with an external streamer tube and a ^{106}Ru source. Additional induced signals are read from aluminum strips within the cells, and the combination of these signals form a 2-dimensional digital pattern of HCAL hits.

The HCAL absorber stops nearly all hadrons, but not muons. Outside the HCAL, nearly eight interaction lengths from the interaction point, two planes of muon chambers measure the angle of fully penetrating muons. These limited streamer tubes induce charge on orthogonal strips, and the charge signals are collected to infer a pair of orthogonal coordinates in $r - \phi$ and z.

The hadronic energy resolution measured from data is

$$\frac{\sigma(E)}{E} = \frac{0.85}{\sqrt{E(\mathrm{GeV})}}$$

for pions at normal incidence [29]. The digital hit pattern in the HCAL and the position information in the muon chambers are used to identify muons.

2.2.7 The Luminosity Calorimeters

Luminosity is measured in ALEPH by counting Bhabha electrons scattered into a well-defined fiducial area and dividing by the Bhabha scattering cross section integrated over the corresponding solid angle. Electron scattering with low momentum transfer is precisely calculated using quantum electrodynamics [32]. The luminosity calorimeter

(LCAL), a lead/wire sampling calorimeter of similar construction to the ECAL, is therefore designed to cover low polar angles between 58 mrad and 160 mrad. The large Bhabha cross section at low angles reduces the statistical uncertainty in the luminosity measurement.

To provide an independent check of the LCAL luminosity, a sampling calorimeter made of tungsten and silicon (SICAL) counts scattered electrons at angles between 30 mrad and 58 mrad. This low-angle measurement is limited in precision by spurious counts from beam-related particles. The SICAL is also integrated with the other calorimeters to contribute to the ALEPH solid angle coverage. This enhanced coverage at low angles is important for Higgs searches having backgrounds with low angle electrons or photons.

2.2.8 The Trigger System

The trigger system is designed to reduce the event rate to a level suitable for tape writing. Unlike trigger systems at hadron colliders, the physics event rate is low enough that no specific physics event types need be selected. The ALEPH trigger simply reduces the overall event rate without suppressing any physics events.

First, the Level 1 trigger combines information from the calorimeters and ITC. Wire energies in the calorimeters are summed inside projective angular segments of 30° azimuth. Each segment triggers separately when the total segment energy passes a set threshold. Look-up tables in the fast ITC trigger use hit information to select only tracks which point roughly back to the interaction point. A space processor identifies a series of hits inside a road in $\cos\theta$, adjusting for the pulse propagation length along the wire as a function of r. If a Level 1 YES decision is given, the TPC gate is held open, and the TPC is fully read out.

Next, the Level 2 trigger replaces the tracking information from the ITC with information from the TPC. Data from dedicated TPC trigger pads subtending 15° in ϕ are passed to look-up tables implemented in the same way as for the ITC. The improved tracking information typically reduces the trigger rate to 4 Hz compared to the 10 Hz rate from Level 1.

Finally, the Level 3 trigger checks the Level 2 decision, using all detector information after an event has been fully read out. Parts of the offline reconstruction, including simple track reconstruction and calorimeter clustering, are implemented at this level to allow sharper selection criteria. During most of the data-taking period in 2000, though, the Level 3 rate was essentially identical to the Level 2 rate.

Chapter 3

Analysis Tools

This chapter describes some of the low-level analysis tools used in the event selections. Such tools are not specific to any single analysis, but instead form the foundations of the analyses which follow. In this chapter, the details of the Monte Carlo simulation of signal and background processes are presented, the energy flow algorithm in ALEPH is summarized, and a method of tagging jets from b quarks is described.

3.1 Event Reconstruction

The `JULIA` event reconstruction program processes the detector output, performing track fitting and merging calorimetric clusters [33]. At least four hits in the TPC are used to begin identifying helical tracks. A road is opened about the extrapolated track in the ITC, and coordinates are added according to a global fit based on a Kalman filter [34]. Compatible hits in the VDET are added to the track. In the ECAL and HCAL, spatially connected calorimeter cells which contain energy above a cutoff threshold are clustered together. During data-taking `JULIA` runs on a dedicated online computer cluster.

For the final data reprocessing, the detector alignment and response constants in JULIA are tuned using events already reconstructed with preliminary constants. In addition, the LEP energy working group releases precise beam energy measurements calculated for 15-minute time intervals during data-taking. The searches presented in the following chapters have been applied to the final reprocessed versions of the data, including those collected in 2000.

3.2 Monte Carlo Simulation

The ALEPH Higgs search relies heavily on accurate simulations of signal and background processes. These simulations are used to calculate event selection efficiencies and to parameterize distributions of discriminant variables used in confidence level calculations.

Events from background and signal processes are simulated with several Monte Carlo event generator programs. Events from each $q\bar{q}$ background flavor are generated using the KORALZ 4.02 generator [35]. Events from the W^+W^- background process, restricted to the CC03 diagrams [36], are generated with the KORALW 1.21 program [37]. Events from $We\nu$ and ZZ diagrams are produced with PYTHIA 5.7 [38], as are the simulated Ze^+e^- events. (Only Ze^+e^- events in which the Z boson has a mass greater than $12\,\mathrm{GeV}/c^2$ are simulated because of the rapidly increasing cross section for lower Z masses. No events from HZ signal production have such a low Z mass.) The $Z\nu\bar{\nu}$ events are simulated with the ZNNBO1 generator [39].

Events from the Higgs signal process are simulated with the HZHA03 generator [19] which includes all possible final states arising from decays of the Higgs and Z bosons as well as the interference between the *Higgs-strahlung* production diagram and the weak boson fusion diagrams. Special samples are generated for final states with low

Background Process	Number of Events	Cross Section (pb)	Equiv. Int. Lumi. (pb^{-1})
dd	100K	16.00	6251
$u\bar{u}$	100K	16.47	6071
$s\bar{s}$	100K	16.00	6249
$c\bar{c}$	100K	16.49	6066
$b\bar{b}$	100K	15.65	6390
Ze^+e^-	100K	7.18	13900
W^+W^-	250K	17.54	14250
ZZ	50K	2.81	17800
$We\nu$	20K	0.884	22600
$Z\nu\bar{\nu}$	20K	0.0183	1090000

Table 3.1: Event samples with $\sqrt{s} = 206\,\mathrm{GeV}$ from Monte Carlo simulation, along with the process cross section and equivalent integrated luminosity.

Higgs or Z boson branching fractions, specifically $Z \to \nu\bar{\nu}$, $Z \to e^+e^-$, $Z \to \mu^+\mu^-$, $Z \to \tau^+\tau^-$, and $H \to \tau^+\tau^-$.

The JETSET 7.4 package [38] is used to model the hadronization of the simulated partons. In this model, a color string joins two colored partons; when the string is stretched past a fixed energy threshold, it breaks, and a new $q\bar{q}$ pair is formed. All simulated datasets are passed through GALEPH, a GEANT-based simulation of the ALEPH detector [40], and are processed with the usual JULIA reconstruction program.

A typical simulation sample corresponds to many times the actual collected integrated luminosity. The representative samples generated with a center-of-mass energy of 206 GeV are summarized in Table 3.1. Samples simulating background processes with four-fermion final states have been generated in 1 GeV steps between 200 and 210 GeV. The kinematic properties of the $q\bar{q}$ background process do not change rapidly with the change in center-of-mass energy, and the relatively large cross section for that process compared to the other background processes means more events must be produced to approach the same equivalent integrated luminosity. For these

reasons, the samples with $q\bar{q}$ final states have been generated only in 2 GeV steps between 200 and 210 GeV.

Samples simulating Higgs production have been generated every 2 GeV in center-of-mass energy between 200 and 210 GeV. For each energy, a full range of Higgs masses between 75 and 120 GeV/c^2 are simulated, with extra samples for masses exactly at the kinematic threshold $m_{\mathrm{H}} = \sqrt{s} - m_{\mathrm{Z}}$.

3.3 Electron and Muon Identification

Electrons and muons are differentiated from other charged particles by their unique detector response. Electron and muon identification in ALEPH have been extensively investigated and tuned for use in heavy flavor physics [41]. The selections in subsequent chapters use modified versions of those identification algorithms.

3.3.1 Electron Identification

Electrons are identified principally by their distinctive ionization energy loss in the TPC and their unique shower shape in the ECAL. The three specific variables which tag electrons are the energy loss due to ionization R_I, the transverse compactness of the associated electromagnetic energy deposit R_T, and the longitudinal shape of the electromagnetic energy deposit R_L.

These variables are in fact three normally distributed estimators, constructed by comparing the measured and expected values for the electron hypothesis. For example, the ionization estimator R_I is defined as

$$R_I = \frac{\frac{\mathrm{d}E}{\mathrm{d}x} - \left\langle \frac{\mathrm{d}E}{\mathrm{d}x} \right\rangle_{\mathrm{e}}}{\sigma_{\mathrm{d}E/\mathrm{d}x}}.$$

The R_T estimator is formed from the total energy deposited in the four ECAL stories nearest the extrapolated track in each stack; the R_L estimator is formed from the inverse of the mean depth of energy deposited. These two electromagnetic shower shape estimators, which are especially useful in identifying high energy electrons, are plotted in Fig. 3.1. Only tracks with $p \geq 2\,\mathrm{GeV}/c$ and $\cos\theta \leq 0.96$ are accepted as

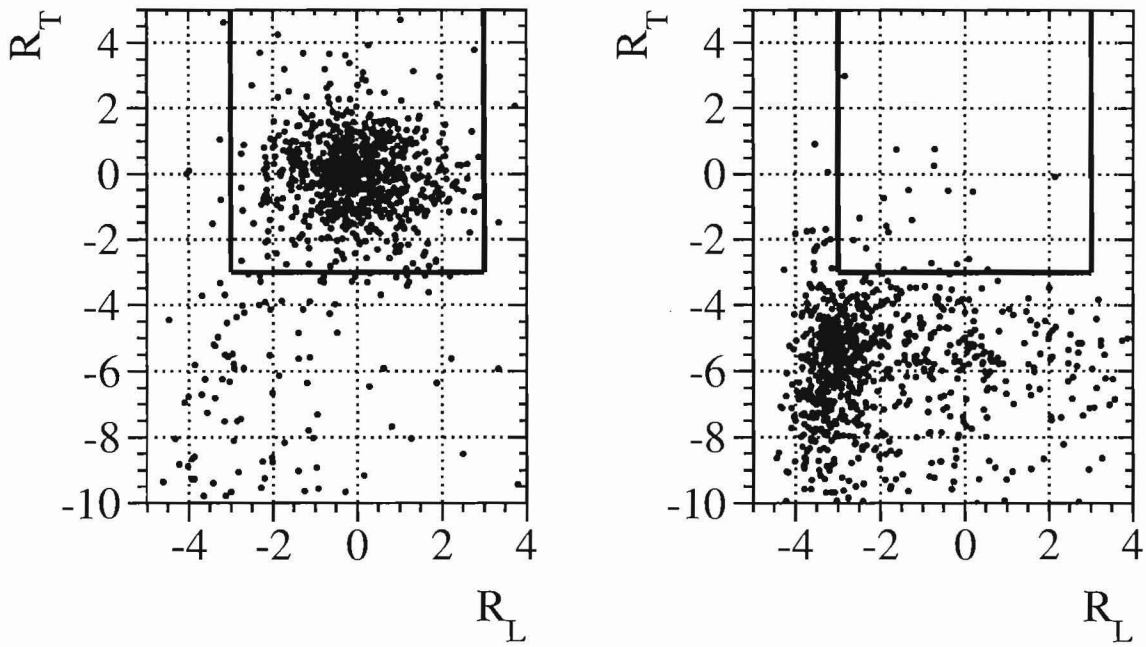

Figure 3.1: Electromagnetic shower shape estimators of longitudinal and transverse energy deposition [42]. A sample enriched in electrons is plotted at left, and a sample enriched in pions is shown at right. The heavy square corresponds to the electron identification cuts described in the text.

electron candidates. The electron identification used in the following selections also requires $R_I > -2.5$, $R_T > -3.0$, and $-3.0 < R_L < 3.0$.

Electron-positron pairs from photon conversion or Dalitz decays are flagged if the pair's invariant mass is less than $20\,\mathrm{MeV}/c^2$ and if the two track helices pass within $1\,\mathrm{cm}$ in the $x - y$ projection and $1\,\mathrm{cm}$ in z at their point of closest approach.

3.3.2 Muon Identification

Muons are identified by their interactions in the HCAL and the muon chambers, the outermost subdetectors. Muons leave a penetrating digital hit pattern in the HCAL and usually produce hits in the muon chamber planes.

A road of width three times the expected multiple scattering is opened around the track direction extrapolated from the TPC. A typical muon-like HCAL hit pattern has at least five hits in the last ten HCAL planes and at least one hit in the last three planes. The extrapolated track must cross ten HCAL planes total, and the ratio of the number of planes with hits to the number of planes traversed must be at least 0.4. Finally, the quantity X_{mult}, defined as the ratio, in the last ten HCAL planes only, of the number of hits to the number of traversed planes, must be less than 1.5. This ultimate cut excludes showers with excess digital hits in the last ten planes.

A charged particle track with $p > 3\,\text{GeV}/c$ and $|\cos\theta| \leq 0.96$ is identified as a muon if it is associated to a muon-like HCAL hit pattern or if it produces hits in both muon chamber planes within 0.5 cm and 150 mrad of the extrapolated track while maintaining $X_{\text{mult}} < 1.5$.

3.4 Energy Flow Algorithm

The reconstruction of the Higgs boson mass depends strongly on the energy resolution of the ALEPH detector. An energy flow algorithm, fully described in Ref. [30], is used to improve the total energy resolution for events with hadronic jets. This process matches cleaned calorimetric clusters with charged particle tracks to form energy flow objects.

The first part of the energy flow algorithm cleans up detector hits from cosmic

rays and electronics noise. A track from a charged particle is considered a good track if it has at least four TPC hits and if it comes from a cylinder of radius 2 cm and length 20 cm centered about the interaction point and coaxial with the beams. Charged particle tracks are also accepted if they are part of a reconstructed V^0 which originated near the interaction point. Noisy calorimeter channels are identified by their presence in many previous events and are ignored in the event reconstruction algorithms.

For all charged particle tracks with momenta between 200 MeV/c and 45 GeV/c, the momentum measured in the tracking subdetectors is more precise than the energy measured in the calorimeters. The second part of the energy flow algorithm associates energy clusters, where possible, with charged particle tracks. Identified electron tracks and their associated ECAL deposits are combined; if more than 3σ extra ECAL energy is associated with the electron, it is assumed to be a photon from bremsstrahlung. Identified muon tracks are combined with up to 1 GeV in the nearest associated ECAL cluster and with up to 400 MeV per plane from the HCAL. Photons and neutral pions are identified and associated with ECAL clusters. When all of these identifications and combinations have been performed, only energy deposits due to neutral and charged hadrons remain unaccounted for. If the remaining energy is larger than the expected calorimeter response to the charged hadrons, then the difference is attributed to neutral hadronic energy. The energy flow algorithm output is a set of energy flow objects, each identified as one of the five types.

If the calorimetric energy for each event in ALEPH were simply summed, the total energy resolution would be $\sigma(E) = 1.2\sqrt{E(\mathrm{GeV})}$ [30]. Studies of 700,000 hadronic events with $\sqrt{s} = 91.2$ GeV found an energy resolution of 6.2 GeV when the energy flow algorithm had been applied. Further studies of events with lower effective center-

of-mass energies, gave an energy-dependent resolution parametrized as

$$\sigma(E)/E = [(0.59 \pm 0.03)/\sqrt{E(\mathrm{GeV})} + (0.6 \pm 0.3)] \times (1 + \cos^2\theta).$$

In simulated two-jet events, the jet angular resolution is 17.7 mrad in θ and 19.4 mrad in $\phi \sin\theta$.

3.5 Tagging Jets from b Quarks

Because the branching fraction $\mathrm{H} \to \mathrm{b\bar{b}}$ is 77% for a Higgs boson with a mass of $115\,\mathrm{GeV}/c^2$, an effective algorithm for identifying jets from b quarks is crucial in reducing the background contribution in Higgs searches.

In the selections which follow, an artificial neural network is used to tag jets from b quarks [43]. The following jet inputs to the network reflect the characteristic high mass and long lifetime of b hadrons:

1. negative logarithm of impact parameter-based probability for tracks in the jet to have come from the primary event vertex [44],

2. χ^2 difference between fitting all tracks in the jet to the primary event vertex and fitting some tracks in the jet to a secondary vertex [45],

3. highest transverse momentum of a lepton with respect to the jet,

4. energy flow object multiplicity / ln E,

5. sum of transverse momenta squared over all energy flow objects in the jet, and

6. boosted sphericity of the jet [46].

The neural network is trained on a sample of jets in simulated $q\bar{q}$ events from radiative returns. In this training sample, jets are rejected if the electromagnetic energy is more than 80% of the total jet energy. For each jet, the values of the six variables, scaled to be in the range $(0, 1)$, are input as a pattern, and the true nature of the jet is appended. When the neural network is trained with the `JETNET 3.0` package [47], the output for b-like jets peaks at 1, and the output for light quark jets peaks at 0. The output of the b tagging neural network is plotted in Figure 3.2 for jets in simulated events and for jets in Z peak data taken in 2000.

A given cut on the network output implies a corresponding efficiency and purity in the b tagging. The rejection factor is different for each type of jet; in particular, jets from c quarks show, to some extent, the same characteristics of high mass and long lifetime as jets from b quarks. The efficiency for tagging b jets vs. the rejection factor for light quark jets is shown in Figure 3.3.

Because Higgs boson signal events are notable for their tagged b jets, it is important that light (non-b) quark jets are not unexpectedly judged b-like by the neural network. The reliability of the b tagging network for light quark jets is checked with a dedicated analysis of $W^+W^- \to q\bar{q}\ell\nu$ events. Since the W bosons decay mostly to udsc quarks, the b tag spectrum should not have a b-like peak at high values. Identified semileptonic events with dijet invariant masses within $40\,\mathrm{GeV}/c^2$ of m_W are selected, and the b tagging network is applied to the two hadronic jets in each event. Figure 3.4 shows the b tag output in simulation and the 2000 data. There is no evidence of light quark jets being falsely tagged as b quark jets.

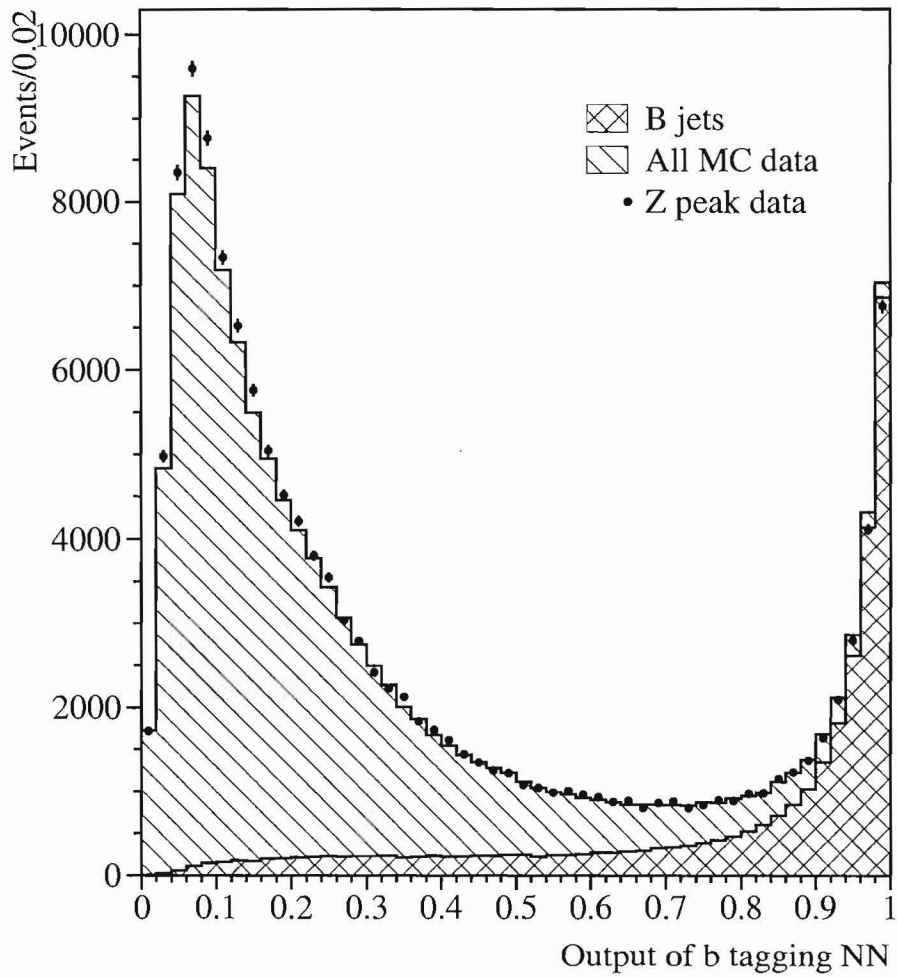

Figure 3.2: The b tagging neural network output for jets in simulated events and in data at $\sqrt{s} = 91.2\,\mathrm{GeV}$. The contribution of jets from b quarks is shown by the cross-hatched region peaking near 1.

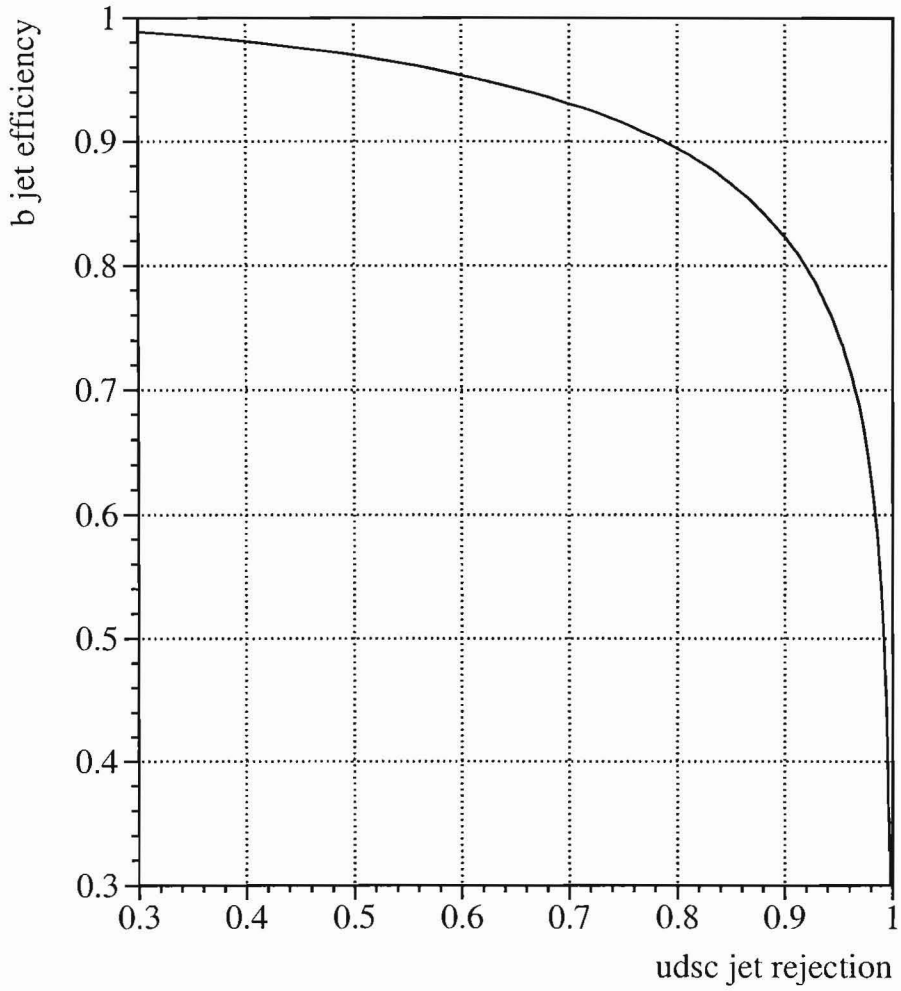

Figure 3.3: The b tagging efficiency vs. the light quark rejection rate for jets in simulated events with $\sqrt{s} = 91.2\,\mathrm{GeV}$.

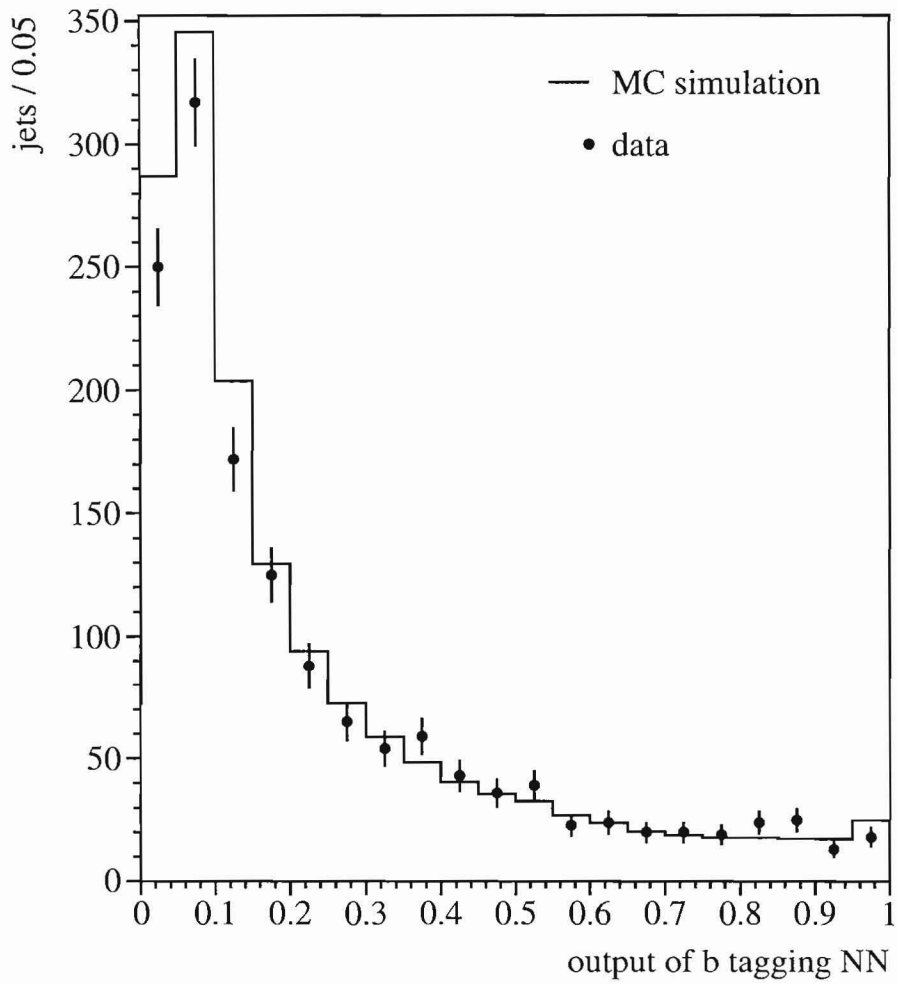

Figure 3.4: The b tagging neural network output for jets in simulated semileptonic W^+W^- events and in data. As expected, few light quark jets from W boson decay have high b tag values.

Chapter 4

Event Selection for Final States with Four Jets

The selection of events with four jets is the analysis most sensitive to HZ production because both bosons decay predominantly to quark pairs (note $\mathcal{B}(\mathrm{H} \to \mathrm{q\bar{q}}) = 87\%$ and $\mathcal{B}(\mathrm{Z} \to \mathrm{q\bar{q}}) = 70\%$). In practice, b tagging is used to reduce contributions from other four-jet processes and to select b jets from Higgs boson decay. There are two classification branches in the final selection: the 2b branch and the 4b branch.

4.1 Preselection

The selection begins with a set of simple preselection cuts which effectively remove large classes of background events from the sample while conserving signal efficiency.

The total energy from charged particle tracks is required to be greater than 10% of the total measured event energy. The event must contain at least eight good tracks, each good track having at least four TPC hits and passing within 10 cm in z and 2 cm in r of the origin.

Each event is clustered into four jets using the Durham algorithm [48]. The resulting y_{34} variable, representing the value of the y for which the natural transition from three to four jets occurs, is required to be greater than 0.001.

Radiative returns to the Z peak are rejected by requiring $|p_z| \leq 1.5\,(m_{\text{vis}} - 90.)$. This cut removes events with a large amount of missing longitudinal momentum, such as events with a photon escaping undetected down the beampipe. An event is also rejected if one of the jets is composed of more than 80% of its energy in electromagnetic objects. This cut rejects radiative return events with a detected high energy photon as well as W^+W^- events with isolated high energy electrons.

The final step of the preselection is to refit the jet energies and angles to conserve overall energy and momentum in the event. This four-constraint fit compensates for missing energy from semileptonic decays in the jets and for mismeasurements of the jet energies [49].

The preselection removes obvious background events; persistent events are filtered by the final selections for the 4b branch and the 2b branch.

4.2 Selection of Final States with Four b Quarks

Although the branching fraction for HZ to four b quarks is relatively low (note that $\mathcal{B}(\text{H} \to \text{b}\bar{\text{b}}) \cdot \mathcal{B}(\text{Z} \to \text{b}\bar{\text{b}}) = 12\%$ for $m_{\text{H}} = 115\,\text{GeV}/c^2$), the event selection is straightforward, and the background contributions are small. The most important tool is the b tagging algorithm described in Chapter 3.

The signal topology consists of four balanced jets, so an additional selection cut removes events with an unbalanced four jet topology. For each three-jet permutation

in the event, the energy-weighted angular dispersion $\Delta\Theta_{ijk}$ is calculated [50]:

$$\Delta\Theta_{ijk} \equiv \left(\frac{\sum_l E_l \Theta^2_{l,\vec{u}}}{\sum_l E_l} \right)^{1/2},$$

where $\Theta_{l,\vec{u}}$ is the angle between the direction of the jets' vector sum $\vec{u}$ and an object l in the jets i, j, k. Requiring the minimum $\Delta\Theta_{ijk}$ be greater than 50 degrees removes events with a "broomstick" topology. The cut is particularly effective in removing $q\bar{q}g$ events when two jets from gluon splitting are next to a third jet.

Events arising from HZ $\rightarrow$ $b\bar{b}b\bar{b}$ production have four jets isolated from one another, each well b-tagged. The final selection uses both of these characteristics.

First, an angular separation term is defined using $\Theta^{\min}_{ij}$, the minimum jet-jet angle in degrees. Requiring the cosine of this angle be less than 0.940 effectively implies the four jets be well isolated. This cut rejects $q\bar{q}g$ events which pass the y_{34} cut by virtue of one broad jet being split into two subjets by the clustering algorithm.

Second, a b tagging term is formed from a dedicated b tagging neural network output η_j for each of the four jets. (For the 4b selection branch alone, a four-variable b tagging neural network is employed [51]. Its performance and structure are similar to those of the six-variable network described in Chapter 3.) This term $\mathcal{B}_4 = 4 - \sum_{j=1}^{4} \eta_j$ is 0 if all jets are well b-tagged and 4 if none is.

These two terms are combined into a linear discriminant variable $F = 300 \times \mathcal{B}_4 - \Theta^{\min}_{ij}$, whose coefficient is determined by an analysis which maximizes the discriminating power between simulated signal and background event samples [52]. Events for which $F < 272$ are accepted and classified as 4b candidates.

The linear combination of the two terms representing the signal characteristics allows a higher signal efficiency than a separate treatment of the two terms. In combination, a signal event with well-isolated jets but poor b tagging in one jet may

still be selected, as may an event with four well b-tagged jets even though two happen to be poorly separated.

4.3 Selection of Final States from Two b Quarks

The 2b selection is implemented with an artificial neural network trained to discriminate between signal and background events. The neural network has 19 input nodes corresponding to the 19 event variables listed in Table 4.1, each scaled to the range $(0, 1)$. The fully-connected feed-forward neural network is trained using the standard back-propagation algorithm in the Stuttgart Neural Network Simulator package (SNNS) [53]. During training, the neural network is presented with six patterns (corresponding to six jet pairing combinations) for each event in the background sample, but only one pattern (corresponding to the one correct pairing) for each event in the signal sample. The weights of the network nodes are adjusted so that the output node value is near 0 for background patterns and near 1 for signal patterns. Because many of the kinematic input variables are sensitive to the simulated Higgs boson mass relative to the kinematic Higgs boson mass threshold $\sqrt{s} - m_Z$, the training sample includes events with simulated masses from 85 to $105\,\mathrm{GeV}/c^2$ at a center-of-mass energy 196 GeV.

Events pass the neural network selection if the value of the final output variable is greater than 0.763. The output value is also used in the confidence level calculation as a further measure of an event's likelihood to have come from Higgs boson production. An event which passes the neural network event selection but fails the 4b selection of the previous section is classified as a 2b candidate; an event which passes the 4b selection is always classified as a 4b candidate.

Variable	Variable Definition
jas	sum of 4 smallest interjet angles (of 6)
cosmin	sum of the 2 smallest cosines of jet-jet angles ($\min(\cos\theta_{ij} + \cos\theta_{kl})$) over all $ijkl$ jet permutations
M_Z	reconstructed Z mass after refitting
E_{max}	largest jet energy
E_3	third-largest jet energy
E_4	smallest jet energy
y_{34}	y_{cut} value for 3- to 4-jet transition
BED	measure of event broadening defined as the minimum over thrust-defined hemispheres of $\left(\frac{\sum_{i=1}^{N_{tracks}} \lvert p_{Ti}\rvert}{\sum_{i=1}^{N_{tracks}} \lvert p_i\rvert}\right)$ with transverse momenta calculated from the thrust axis
$(1-\eta_3)(1-\eta_4)$	product of Higgs jets' NN b-tag outputs
$\min(\eta_3, \eta_4)$	minimum of Higgs jets' NN b-tag outputs
$\sum \eta_i$	sum of 4 NN b-tag outputs
bs_1	lowest boosted sphericity [46] of any jet
bs_2	second-lowest boosted sphericity of any jet
$Mult_1$	lowest jet multiplicity of tracks with rapidity greater than 1.6
$Mult_2$	second-lowest jet multiplicity of tracks with rapidity greater than 1.6
M_1	smallest rescaled jet mass
M_2	second-smallest rescaled jet mass
α_{12}	decay angle of "Z" jets in parent rest frame
α_{34}	decay angle of "H" jets in parent frame

Table 4.1: Input variables to the four-jet 2b event selection neural network. The first six variables measure event kinematic quantities, and the next two quantify the event's shape. Three variables parametrize the b content of the jets, and six more variables suppress gluon and light quark jets according to the jet shape and multiplicity. The final two variables provide information on jet assignment to parent bosons.

4.4 Jet Pairing and Mass Reconstruction

A problem unique to the four-jet channel is the ambiguity of jet pairing. Even if an event is truly due to Higgs boson production, only one of the six possible pairings is correct. A neural network output value is calculated for each pairing, whether the event is classified 2b or 4b. The pairing with the highest output is selected as the pairing for that event, and the reconstructed Higgs mass is based on that pairing. In the 2b branch, the b tag values and the reconstructed Z boson mass have the largest influence on the output for different pairings; in the 4b branch, the reconstructed Z mass and the decay angles in the parent boson rest frame have the greatest effect.

The reconstructed Higgs mass for the selection is defined to be $M_{\mathrm{H}} = M_{12} + M_{34} - 91.2$, where the implicit assumption of HZ production has been used. Any mismeasurements of the two fitted dijet masses are anticorrelated due to the constraint on the total event energy and momentum. Consequently, the use of the dijet mass sum (as opposed to a simple dijet mass) results in a sharper reconstructed mass resolution (Fig. 4.1) and consequently a more powerful discrimination between signal production and the background continuum.

A cuts analysis which uses the same kinematic fitting procedure and reconstructed mass definition [54] can be used to check the reliability of the Higgs boson mass reconstruction. All of the cuts which isolate high-mass four-jet signal events are applied, but events having jets with b tag values greater than 0.9 are rejected. With the anti-b cut, the selection is dominated by $\mathrm{W^+W^-}$ background contribution, as shown in Fig. 4.2. Correct jet pairings in $\mathrm{W^+W^-}$ events are faithfully reconstructed at $2m_{\mathrm{W}} - m_{\mathrm{Z}} \approx 70\,\mathrm{GeV}/c^2$; the broad peak at higher masses corresponds to incorrect pairings. (The algorithm which is most efficient for Higgs boson jet pairing is not optimal for $\mathrm{W^+W^-}$ jet pairing.) Most importantly, no significant disagreement is

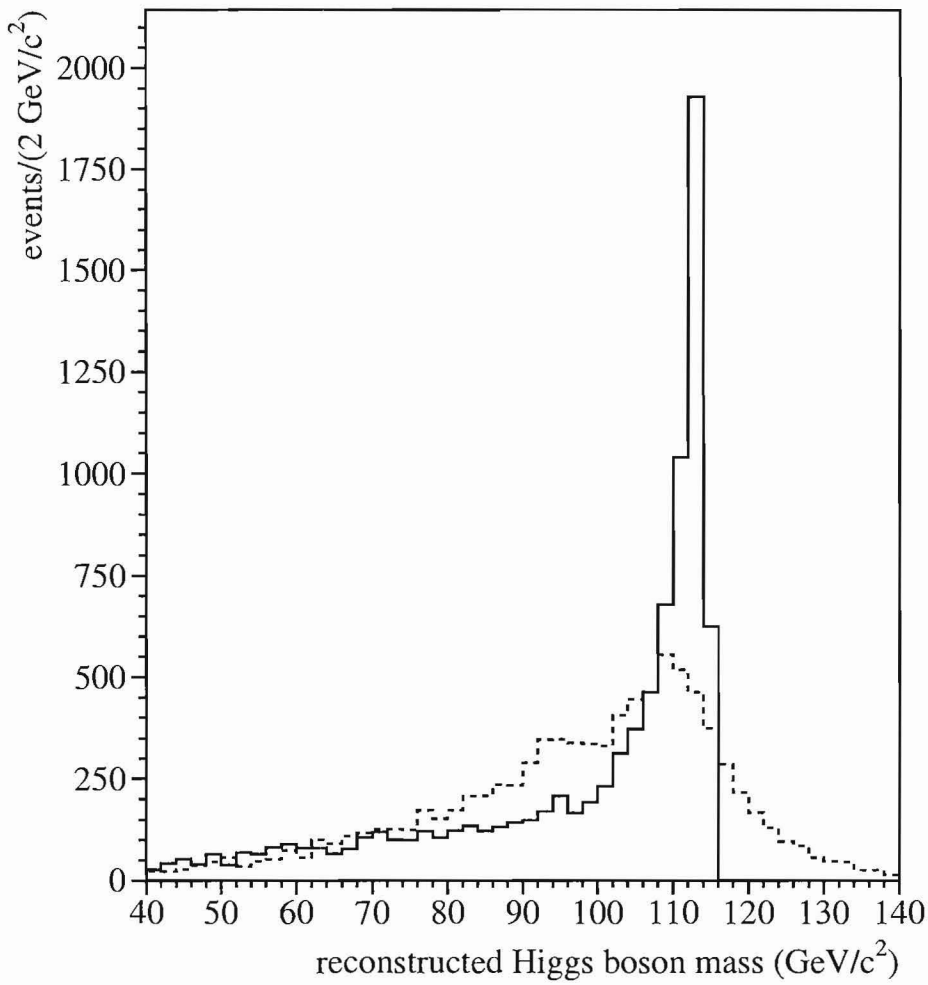

Figure 4.1: Reconstructed Higgs boson mass distributions for simulated four-jet HZ signal events which survive the NN output cut. A four-constraint kinematic fit is applied to events with $\sqrt{s} = 206$ and $m_{\mathrm{H}} = 114\,\mathrm{GeV}/c^2$, and both mass definitions are calculated for each event. The invariant mass of the two jets paired to form the Higgs boson is plotted with a dashed line, and the reconstructed Higgs boson mass $M_{\mathrm{H}} = M_{12} + M_{34} - 91.2$ is plotted with a solid line.

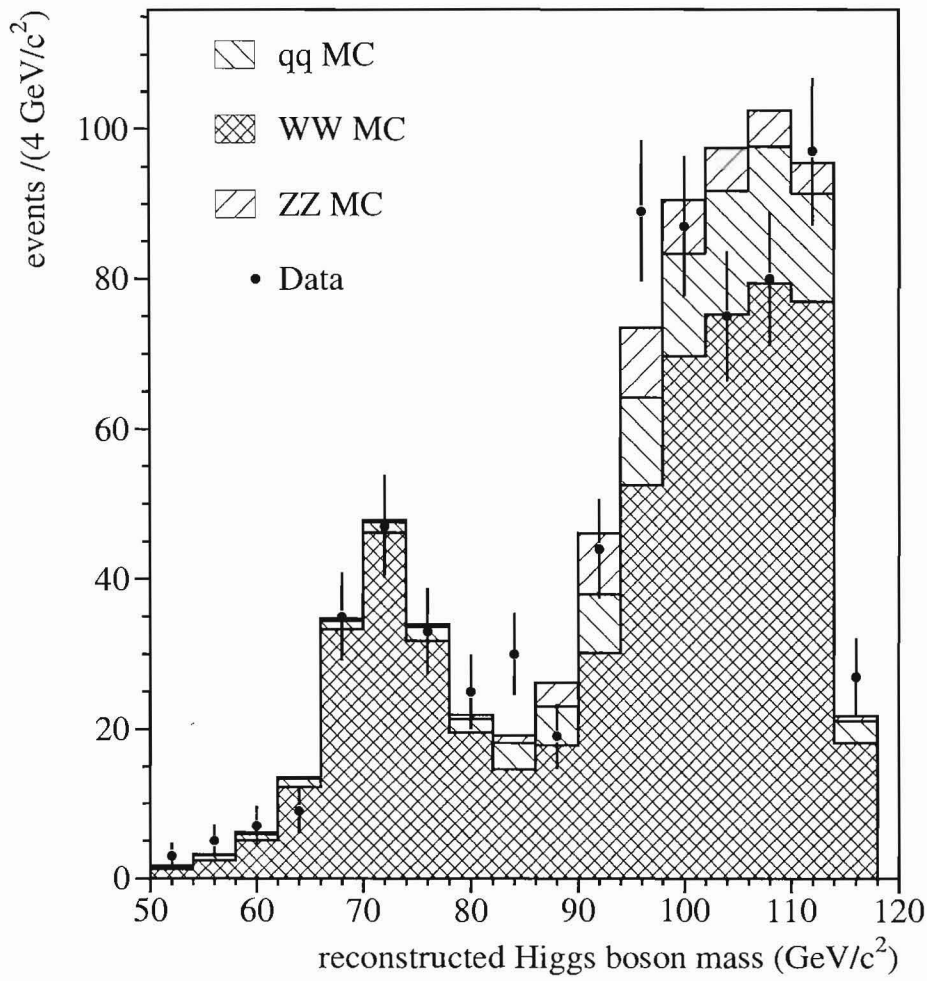

Figure 4.2: Reconstructed Higgs boson mass in selected four-jet events after applying an anti-b cut.

observed between simulation and data.

4.5 Results from Selection

Only two diagrams contribute significantly to the expected number of background events in the 4b selection: $e^+e^- \to ZZ \to b\bar{b}b\bar{b}$ and $e^+e^- \to b\bar{b}g \to b\bar{b}b\bar{b}$. In the latter case, the b jets split from the gluon are often poorly separated – such events are penalized in the selection by the minimum jet-jet angle term. In the former case, both dijet masses (assuming the correct pairing is chosen) cluster near m_Z. This diagram therefore contributes little to the high reconstructed mass region after the final selection is made. For the 2b selection, which lacks a hard b tag cut, the W^+W^- diagram contributes along with the $q\bar{q}$ and ZZ diagrams to the expected background.

Distributions of the discriminating variable F are shown in Figure 4.3 for data and simulation, and distributions of the neural network output variable are plotted in Figure 4.4. At the preselection level, simulated events from the W^+W^- diagram dominate because of their four jet topology and high cross section compared to the ZZ background. When all cuts in the 4b selection are applied, 5.8 events are expected, and 10 are selected; for the 2b selection, 41.9 are expected, and 43 are observed (Table 4.2). Because the final selection relies heavily on b quark tagging, the expected number of events from ZZ production is a large fraction of the total expected background.

The simple event counting implied in Table 4.2 does not give a complete indication of the relative expected contributions of signal and background events to the dataset. In particular, the use of discriminant variables such as the reconstructed Higgs boson mass effectively deweights selected candidates with values outside the range expected for $Hq\bar{q}$ signal events. The reconstructed mass is illustrated in Fig. 4.5, focusing

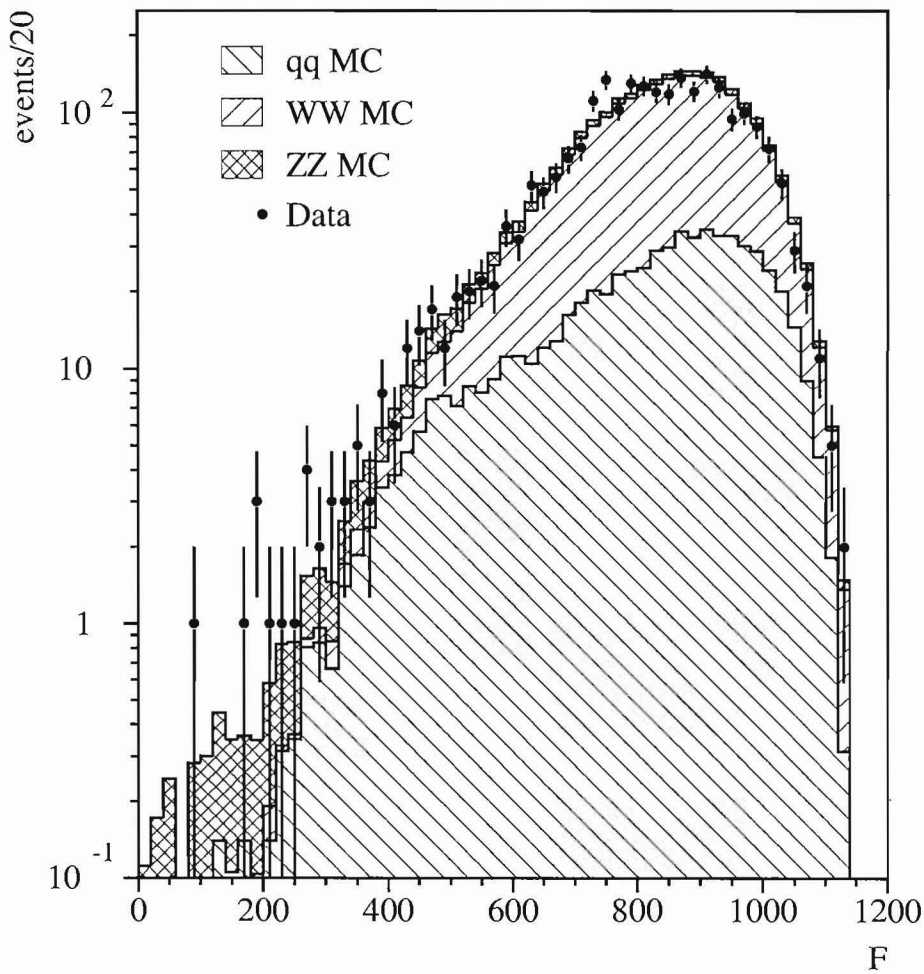

Figure 4.3: Distributions of the F variable in data and simulation. Events with F values less than 272 pass the 4b selection.

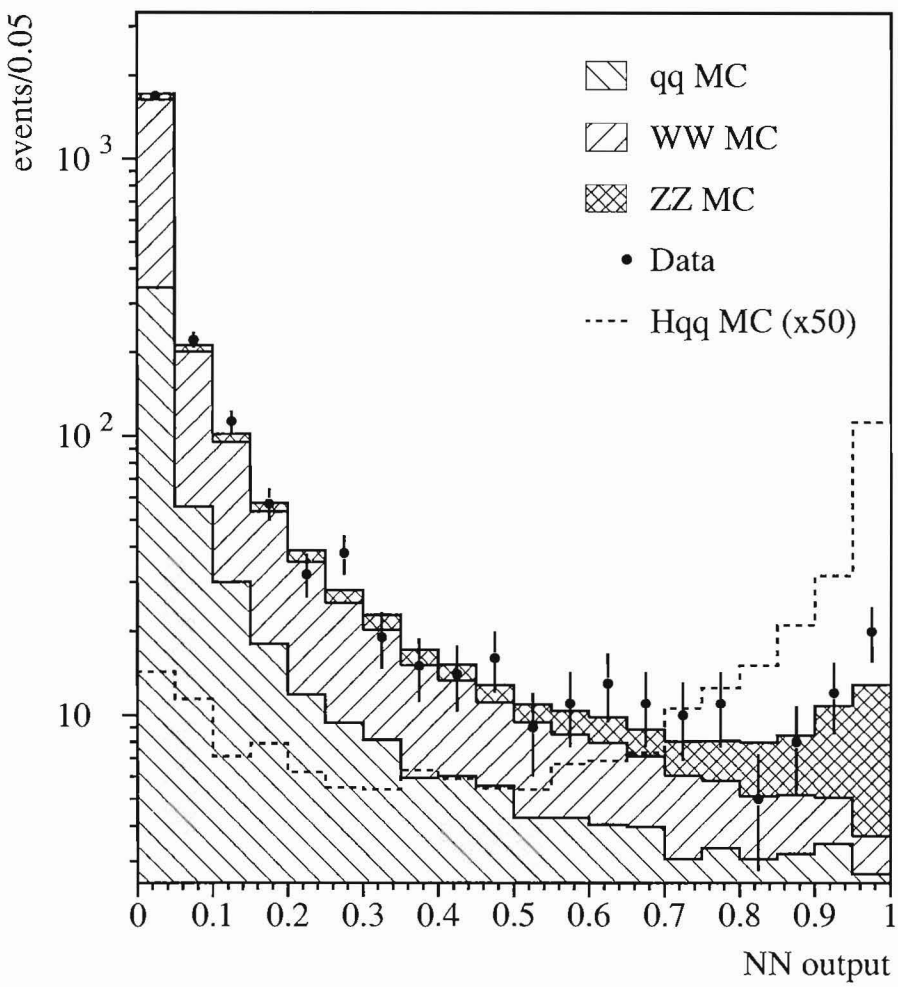

Figure 4.4: Distributions of the four-jet 2b selection neural network output variable in data and simulation. The histogram of the signal distribution has been scaled up by a factor of 50. Events with output greater than 0.763 pass the 2b selection.

	Number of events	
	2b	4b
Total $Hq\bar{q}$ signal	2.35	0.60
ZZ	19.18	3.96
$q\bar{q}$	14.24	1.71
W^+W^-	8.46	0.12
Total background	41.89	5.80
Observed candidates	43	10

Table 4.2: Expected and observed number of four-jet events in 2000. The simulated $Hq\bar{q}$ signal assumes $m_H = 115\,\mathrm{GeV}/c^2$.

on the range between the previous Higgs boson mass limit and the highest masses kinematically allowed at LEP. For example, if the combined 2b/4b selection required the reconstructed Higgs boson mass to be between 113 and $117\,\mathrm{GeV}/c^2$ (roughly the mass resolution about the observed excess), then 2.1 background events and 0.8 $Hq\bar{q}$ signal (with $m_h = 115\,\mathrm{GeV}/c^2$) events would be expected, compared to 5 candidates observed. When event weights are computed using the likelihood ratio, as described in Chapter 7, candidates with signal-like properties are assigned a higher event weight than candidates with background-like properties.

4.6 Discussion of Candidates from the Four-Jet Selection

Among the candidates selected by the four-jet selection, three carry high event weights for a Higgs boson mass hypothesis of $115\,\mathrm{GeV}/c^2$, as calculated from their discriminant variable values. These three events have reconstructed Higgs boson masses greater than $108\,\mathrm{GeV}/c^2$ and very high neural network output values, all greater than 0.99. Two of the candidates are classified as 4b; the third is classified as 2b. For

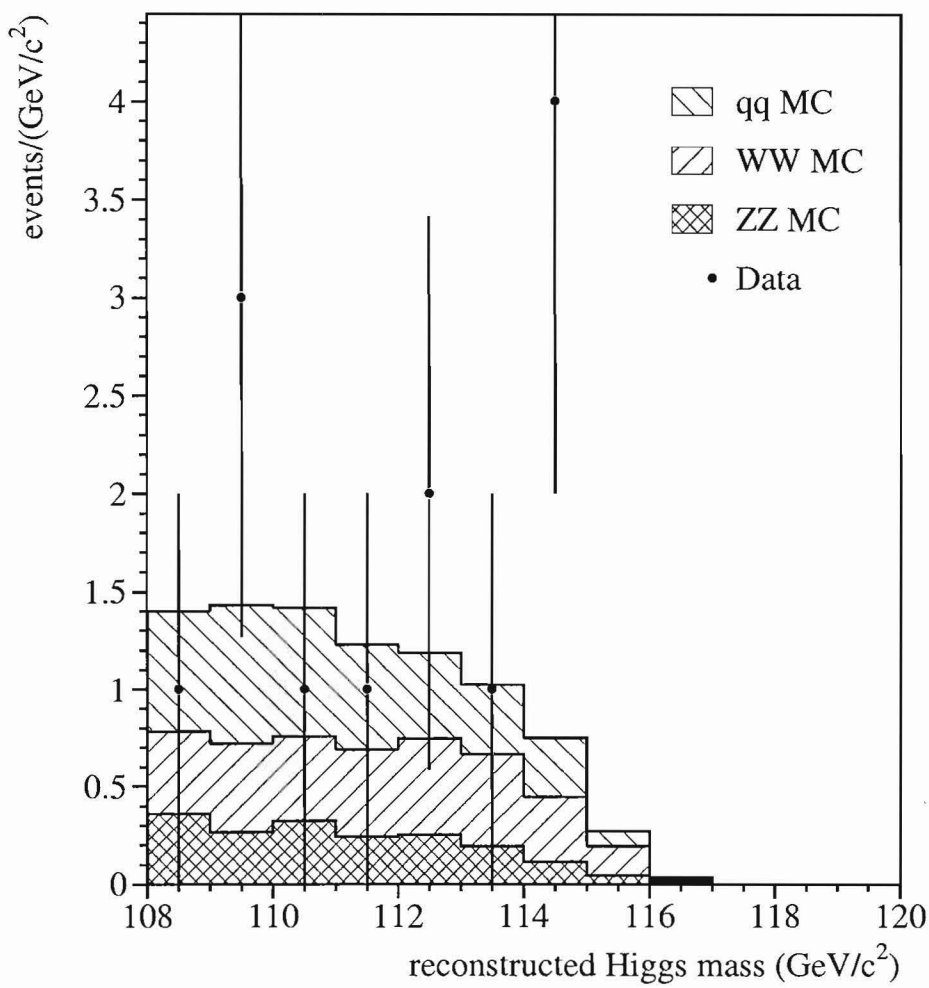

Figure 4.5: Reconstructed Higgs boson mass from selected four-jet events. Masses below $108\,\mathrm{GeV}/c^2$ have already been excluded by previous LEP searches and are not plotted.

this selection, the reconstructed higgs boson mass and the neural network output are the discriminant variables used to calculate event weights; consequently, these three events contribute significantly to the final observed excess.

The first candidate (run 54698, event 4881) is classified as a 2b event. Collected

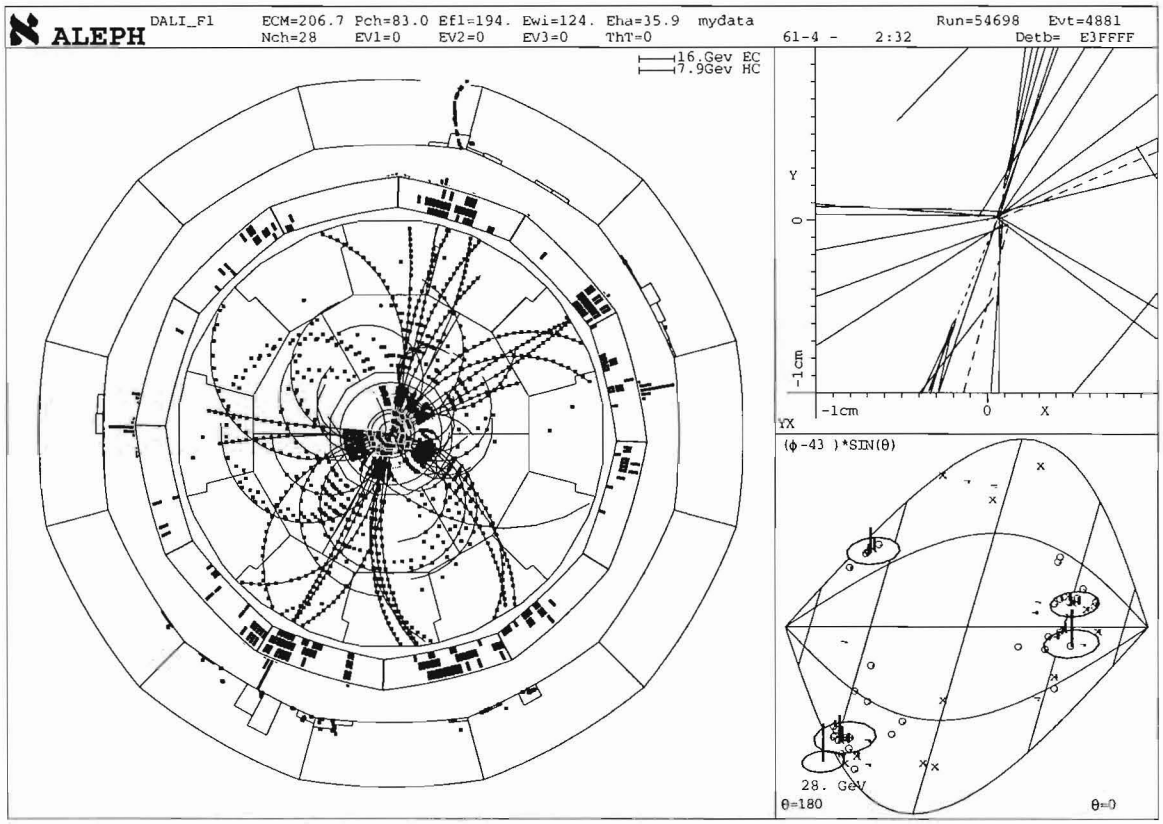

Figure 4.6: Run 54698, event 4881 in the DALI event display [55]. The zoomed frame at top right shows evidence for secondary vertices in two jets, while the frames at left and bottom right show the angular separation of the four jets in the $x - y$ and $\phi - \sin\theta$ planes, respectively.

at a center-of-mass energy of 206.6 GeV, it has two jets with clear secondary vertices and high b tag values (0.999 and 0.998). The event display (Fig. 4.6) shows four jets well separated in space, and it also shows the secondary vertices in the zoomed region [56]. The reconstructed Higgs mass for this event is $M_{\mathrm{H}} = 101.1 + 104.3 - 91.2 =$

114.2 GeV/c^2, and the neural network output is 0.997. Such high measured dijet masses make this event unlikely to come from W^+W^- or ZZ production.

The second candidate (run 56065, event 3253), collected at a center-of-mass energy of 206.7 GeV, is classified as a 4b event. The high b-tagging network outputs for all

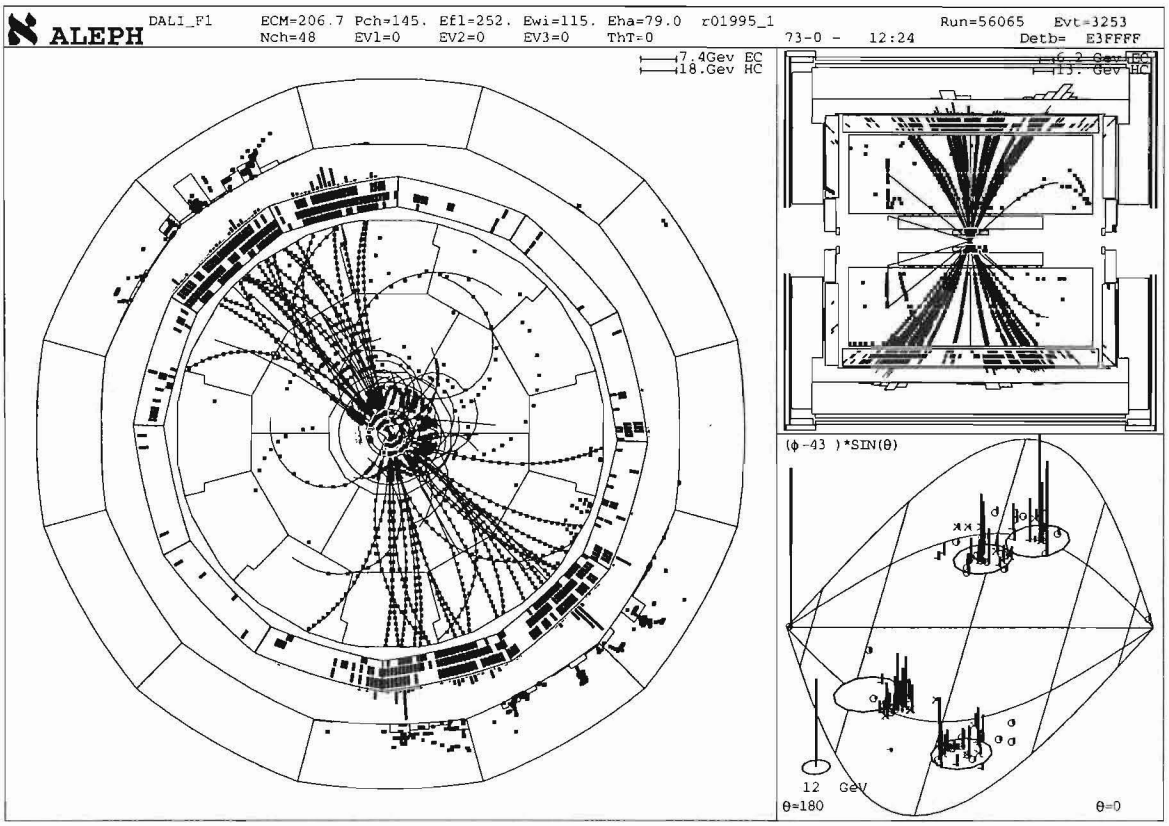

Figure 4.7: Run 56065, event 3253 in the DALI event display.

four jets (0.996, 0.663, 0.992, and 0.999) preclude the W^+W^- hypothesis for this event. The total energy for this event is 252 GeV, part of which is due to a 22 GeV deposit in the small-angle calorimeter (Fig. 4.7). Such a high visible energy supports the hypothesis that the energy cluster is a beam-related deposit in coincidence with the underlying four-jet event. An objective algorithm, which was developed and tested on events in the ALEPH data stream taken with random triggers, also confirms that

hypothesis [57]. When the event is reconstructed without the foreign SICAL energy flow object, the reconstructed Higgs boson mass is 114.5 GeV/c^2.

The third candidate (run 56698, event 7455) is also classified as a 4b event (Fig. 4.8). Three jets have high b tagging network output values (0.999, 0.831, 0.999),

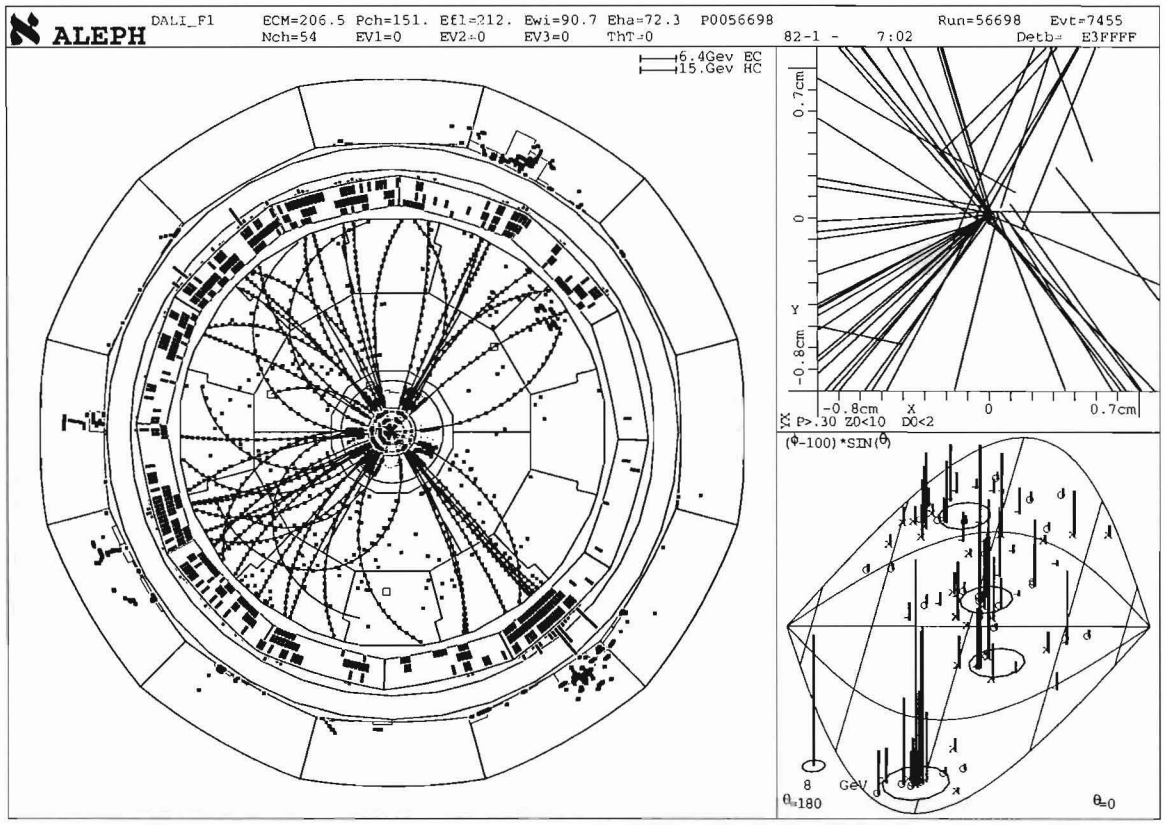

Figure 4.8: Run 56698, event 7455 in the DALI event display.

but the fourth has a b tag value of 0.197. According to simulation, the probability for a HZ $\rightarrow$ b$\bar{\text{b}}$b$\bar{\text{b}}$ event to have such a poorly b-tagged jet is 19% [58]. Although the event selection neural network output (0.999) is high, the F value of 268 just passes the cut for the 4b selection. The reconstructed Higgs boson mass for this event, collected at $\sqrt{s}$ = 206.7 GeV, is 109.9 GeV/c^2. If the candidate is interpreted as a ZZ event, a kinematic fit [59] yields very large boson masses of 98.9 and 101.6 GeV/c^2.

A fourth four-jet candidate (run 56366, event 955) with a high reconstructed Higgs boson mass ($114.4\,\mathrm{GeV}/c^2$) is less significant than the other three because its neural network output value is only 0.933. This 2b candidate, collected at $\sqrt{s} = 206.4\,\mathrm{GeV}$, has a reconstructed Z boson mass of just $78.8\,\mathrm{GeV}/c^2$, significantly low for a true HZ event.

Chapter 5

Event Selection for Final States with Tau Lepton Pairs

The production of associated H and Z bosons may also result in final state topologies with tau lepton pairs. In one final state, a Higgs boson decays to a $b\bar{b}$ pair, while the Z boson decays to $\tau^+\tau^-$; in a second final state, the Higgs boson decays to $\tau^+\tau^-$, and the Z boson decays to $q\bar{q}$. A separate selection addresses each of these two final states. The main challenge in the event selection is to identify tau leptons reliably even in the midst of hadronic jets. A tau lepton which decays to three or more hadrons can be mimicked by part of a broad jet; a tau lepton which decays to a low momentum electron or muon can be confused with a lepton from semileptonic decay in a jet.

5.1 Preselection

The preselection begins with hadronic events having at least 8 good tracks, the total energy of which is at least 20% of the center-of-mass energy. The event's missing energy is required to be greater than the event's transverse momentum; this cut

removes poorly measured or noisy events with excess energy in the calorimetry.

Many of the other preselection cuts remove $q\bar{q}$ events with radiative returns to the Z peak. These events are characterized by an initial-state radiation photon, the most typical energy of which is $E_\gamma^{\text{peak}} = \frac{\sqrt{s}}{2} - \frac{m_Z^2}{2\sqrt{s}}$. Such photons may escape detection at low angles, or they may be reconstructed in the detector. Events are rejected if the magnitude of the event longitudinal momentum is greater than $0.6\,E_\gamma^{\text{peak}}$ or if the sum of the event missing energy and longitudinal momentum magnitude is greater than $1.8\,E_\gamma^{\text{peak}}$, as shown in Fig. 5.1. If an identified photon in an event is isolated by at least 15° and has energy greater than $0.6E_\gamma^{\text{peak}}$, the event is removed. (The isolation of an object is defined as the half-angle of the smallest annular cone about the track direction which admits no more than 5% of the total measured event energy, excluding energy within 2° of the object itself.)

The same cuts which reject radiative return $q\bar{q}\gamma$ events also reject Ze^+e^- events in which one low-angle electron escapes detection. Other requirements remove events with energetic isolated electrons or muons, typical of W^+W^-, ZZ, and Ze^+e^- diagrams. In particular, if an event contains an isolated electron or muon with energy greater than 25% of the center-of-mass energy, the event is rejected. This cut effectively removes Ze^+e^- events as well as W^+W^- and ZZ events with leptonic decays. Electrons and muons from tau lepton decay typically have a softer energy spectrum and are not affected by this cut.

5.2 Tau Lepton Identification

The tau leptons are identified inclusively within the event as "minijets," jets with small invariant masses. To begin, energy flow objects are clustered into jets with a maximum jet invariant mass of $2.7\,\text{GeV}/c^2$. Even though the tau lepton mass is

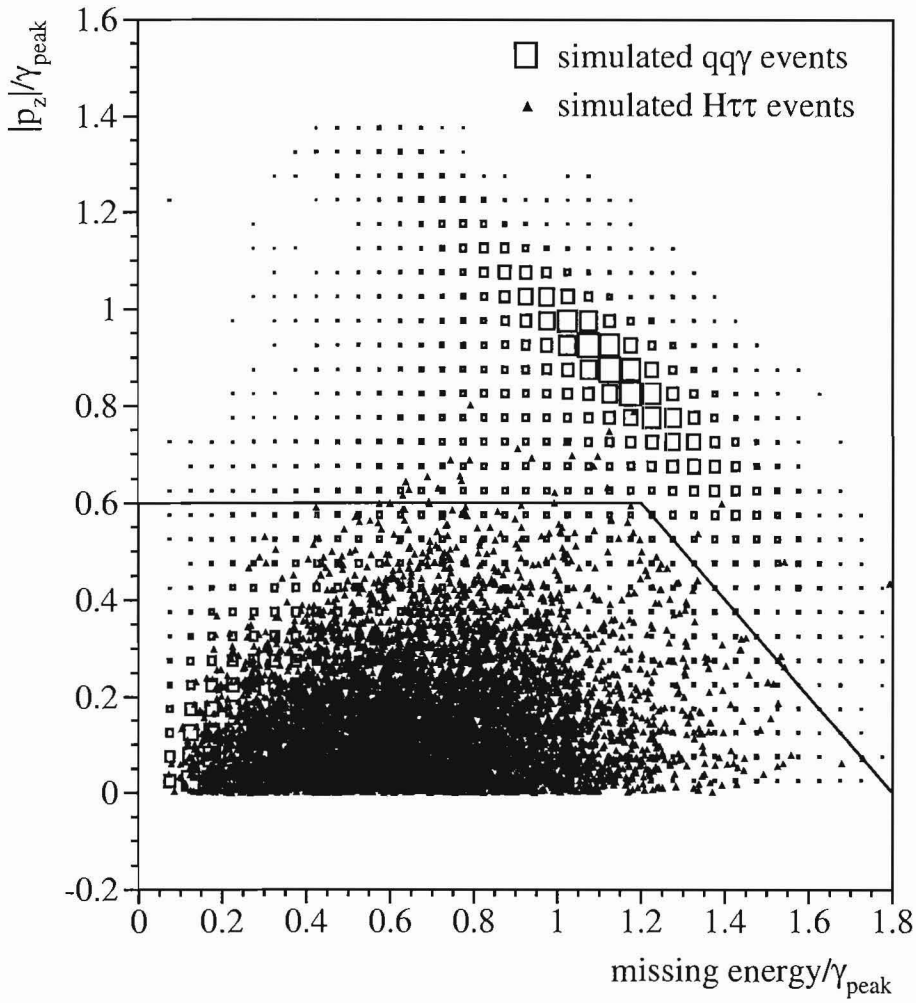

Figure 5.1: Graphical cut to remove $q\bar{q}$ events with ISR. Both $q\bar{q}$ background events and $H\tau^+\tau^-$ signal events are generated at $\sqrt{s} = 206\,\mathrm{GeV}$. (With respect to these kinematic variables, $\tau^+\tau^-q\bar{q}$ signal events are identical to $H\tau^+\tau^-$ events.)

$1.8\,\mathrm{GeV}/c^2$, a slightly higher cutoff value allows a minijet to include contamination from a random fragmentation track while retaining all objects from the tau lepton itself. A typical signal event contains ten minijets.

Only minijets isolated by more than 15°, using the previous isolation definition, are considered as tau lepton candidates. Minijets are accepted only if the number of tracks from charged particles with momentum greater than $1\,\mathrm{GeV}/c$ is at least one and not greater than three. A tau lepton candidate minijet is required to have unit charge. (Exceptionally, a tau lepton candidate may contain two particle tracks if a track is lost due to the momentum cutoff or if a track from a hadronic jet contaminates the true tau lepton jet. In that case, the charge of the particle with higher momentum is used.)

Further classification of the minijets allows additional cuts to reduce specific sources of fake tau leptons. The tau leptons from heavy boson decay typically have a high momentum. If the tau lepton further decays into more than one charged particle, the ν_τ momentum is typically small, and the charged particles conserve the parent's high momentum. For this reason, the momentum of classified two- and three-track tau lepton candidates is required to be greater than $12.5\,\mathrm{GeV}/c$. On the other hand, if a tau lepton decays to one charged particle and one or two neutrinos, the single charged particle carries significantly less momentum than in the three-track case, and no momentum cut is applied. In the intermediate case of tau lepton decay to both charged and neutral hadrons – minijets for which $p_{\pi^\pm} < 0.8E_\tau$ – the total tau lepton candidate momentum must be greater than $7.5\,\mathrm{GeV}/c$.

One common source of fake tau lepton candidates is isolated high energy leptons, especially from photon conversions in $\mathrm{q\bar{q}}\gamma$ events. Electrons in the one-track tau lepton candidates must either have a hit in the VDET or not be identified as a conversion. Neither track in a two-track tau lepton candidate may be an electron.

The relative representation of the tau lepton minijet classes after preselection is shown in Fig. 5.2. The rest of the analysis proceeds by looping over all pairs of oppositely-charged tau lepton minijet candidates. In order to reduce the combinatoric background from low multiplicity jets in $q\bar{q}g$ events, the selection rejects pairs of three-track tau minijets. The objects comprising the tau lepton candidates are locked, and the rest of the event is clustered into two jets using the Durham algorithm.

The jet momenta of each event are rescaled, assuming a jet invariant mass of m_τ for the two tau lepton minijets and a fixed velocity vector for the other two jets. The rescaling algorithm minimizes the value of a fit estimator χ^2 defined as the sum of four terms. The first two terms, $(E - \sqrt{s})/\sigma_E^2$ and $\sum_{i=1}^{3} p_i^2/\sigma_{p_i}^2$, favor event energy and momentum conservation, respectively. The third term, a sum

$$\sum_{i=1}^{2\text{ jets}} \frac{(E_i - E_i^0)^2}{\left[\left(0.6\sqrt{E} + 0.6\right)(1 + \cos^2\theta)\right]^2}$$

over the two non-tau jets, disfavors large rescaling of jet energies beyond the ALEPH energy flow jet resolution [30]. The fourth term in the fit estimator compares dijet mass differences corresponding to each of two event hypotheses in turn. For the $HZ \to b\bar{b}\tau^+\tau^-$ hypothesis, the term $(M_{\tau^+\tau^-} - m_Z)^2/\sigma^2$ compares the difference between the rescaled $\tau^+\tau^-$ invariant mass and m_Z with a $3\,\mathrm{GeV}/c^2$ resolution [59]. For the $HZ \to \tau^+\tau^- q\bar{q}$ hypothesis, a term $(M_{q\bar{q}} - m_Z)^2/\sigma^2$ compares the difference between the $q\bar{q}$ invariant mass and m_Z with the same $3\,\mathrm{GeV}/c^2$ resolution.

Some practical bounds limit the energy rescaling. In no case are the non-tau jets allowed to rescale to less than 75% of the measured momenta; neither may the tau lepton minijets rescale to less than 90% of their measured momenta. Events failing the kinematic fit are rejected.

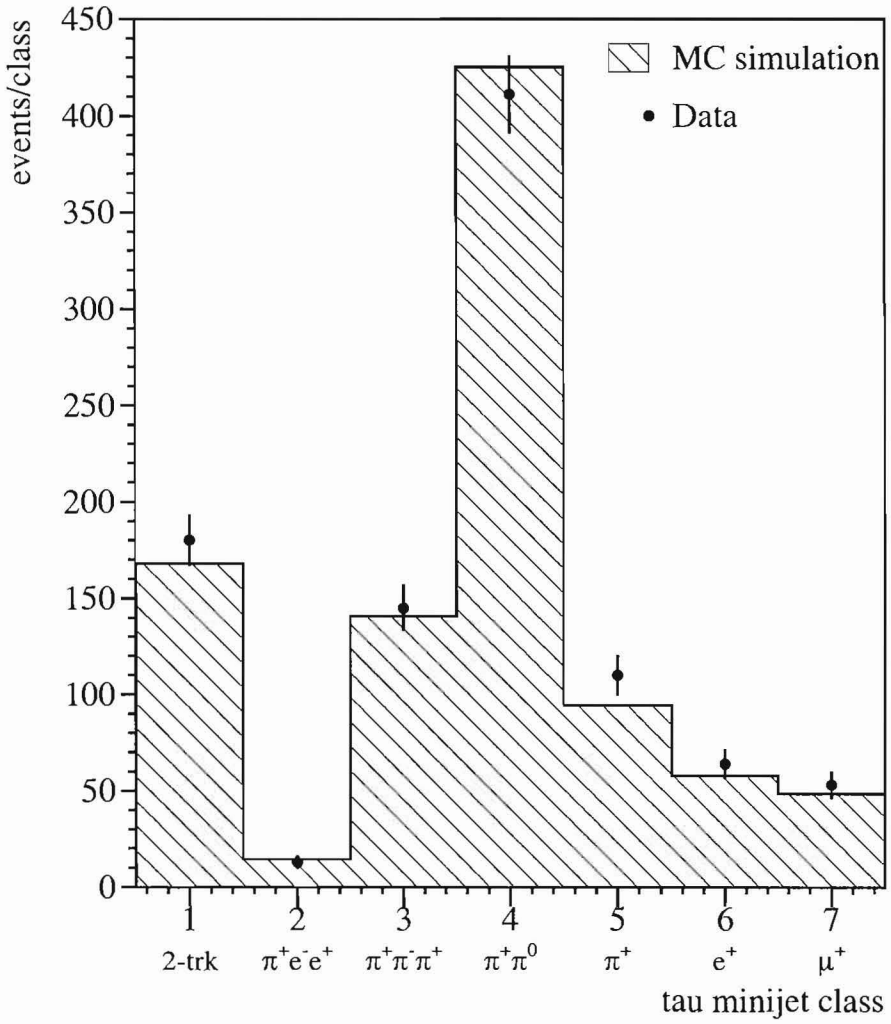

Figure 5.2: Tau lepton minijet candidate classes in data and simulation. The classes are labelled assuming a τ^+ minijet.

Because the number of restricted variables exceeds the number of jet energies being rescaled, the fit estimator is itself useful for quantifying the compatibility of the overconstrained fit. If more than one pairing combination of tau lepton minijets exists, then only the combination with the lowest fit estimator is considered in the event selections that follow.

5.3 Selection of HZ $\rightarrow \tau^+\tau^-q\bar{q}$ and HZ $\rightarrow b\bar{b}\tau^+\tau^-$ Final States

After the common preselection and tau lepton minijet identification, events from each of the two final states are selected with two dedicated artificial neural networks.

The few event variables which promise the most discrimination between signal and background events are used as inputs to the neural networks. For both networks, the following four kinematic quantities are used:

1. the tau isolation, defined in the same way as the photon isolation in the preselection;

2. χ^2, the kinematic fit estimator;

3. p_T, the event total transverse momentum; and

4. p_T^{jet}, the sum of the fitted transverse momenta of the tau jets with respect to the nearest hadronic (non-tau) jet axis.

For the $b\bar{b}\tau^+\tau^-$ selection network, a fifth variable, the sum of the b tagging neural network outputs for the two hadronic jets, suppresses background contamination from the $q\bar{q}$ and W^+W^- diagrams.

The three-layer neural network architecture is simple and robust, with 10 hidden nodes and 1 output node. The networks are trained, using the SNNS package, so that the output for signal events clusters near 1, and the output for background events clusters near 0. The output from the single node is shown in Fig. 5.3. Events with neural network output node values below 0.875 are rejected.

5.4 Overlap between Selections

A single event may generate high output values in both independent neural networks; however, if the results from the two selections are to be combined in a simple way, they must be uncorrelated. To keep the $b\bar{b}\tau^+\tau^-$ and $\tau^+\tau^-q\bar{q}$ final states exclusive, events which pass the cut on both neural network outputs are classified unambiguously using the kinematic fit estimator.

To simplify the treatment of the overlap between selections, the same network output cut value is used for both HZ final state selections. A scan over a single cut value applied to both outputs, when compared to a true two-dimensional scan, shows a negligible loss of performance.

Both neural network values are calculated for an event; if the sum is less than 1.8, then the selection with the higher output value is assumed. If both neural network output values are high, then the difference between the outputs is evidently small, and the kinematic fit estimator χ^2 is used to choose the assignment. If $\chi^2_{b\bar{b}\tau\tau}$ is less than $\chi^2_{\tau\tau q\bar{q}}$, the event is classified as a $b\bar{b}\tau^+\tau^-$ candidate; otherwise, it is classified as $\tau^+\tau^-q\bar{q}$.

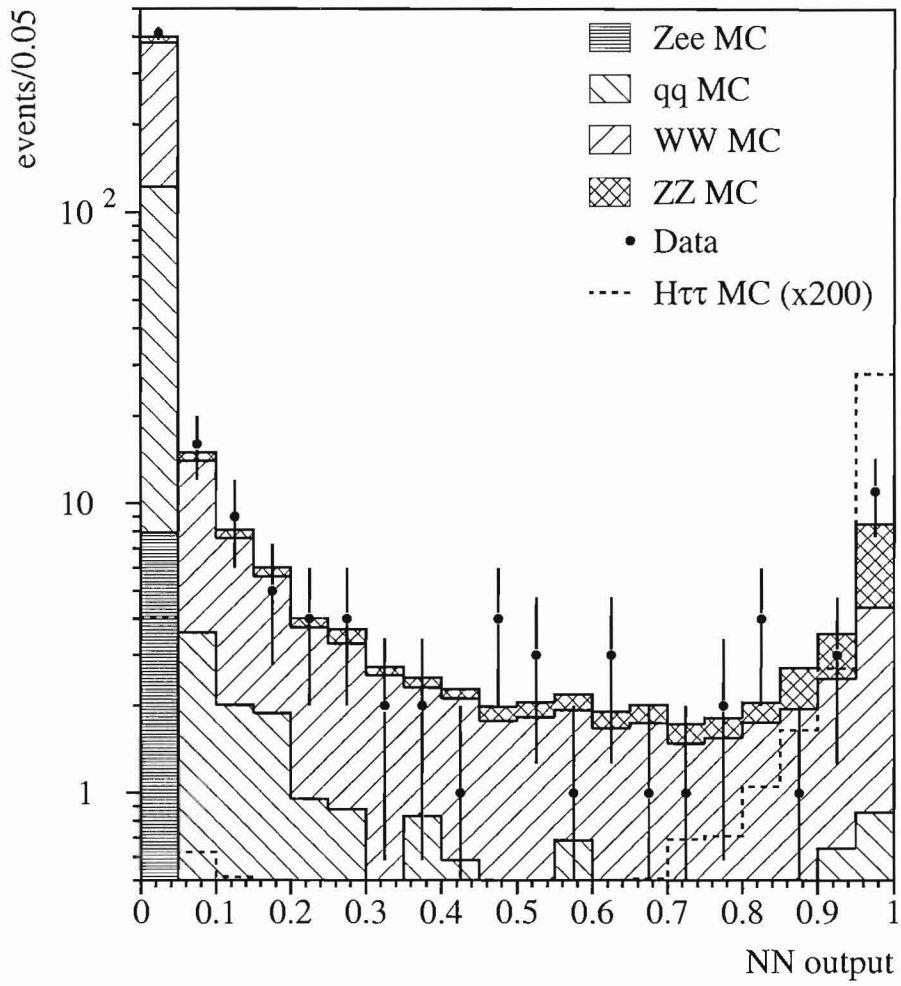

Figure 5.3: Distributions of the $\tau^+\tau^-$ selection network output in data and in simulation. The histogram of the $H\tau^+\tau^-$ signal distribution has been scaled up by a factor of 200. Events with network outputs greater than 0.875 are accepted as candidates.

5.5 Results from Selections

The expected contributions from signal and background processes are summarized in Table 5.1. A total of 15 candidate events are observed when the combined selection is

	Events
$\tau^+\tau^-q\bar{q}$	0.16
$H\tau^+\tau^-$	0.11
Total signal	0.27
W^+W^-	6.21
ZZ	5.74
$q\bar{q}$	1.06
Ze^+e^-	0.71
Total background	13.72
Observed candidates	15

Table 5.1: Expected and observed number of events with tau lepton pairs in 2000. The simulated signal assumes $m_H = 115\,\mathrm{GeV}/c^2$.

applied to the collected data. In light of the observed $Hq\bar{q}$ excess, it is interesting to note that two selected candidates have reconstructed Higgs boson masses greater than $115\,\mathrm{GeV}/c^2$ after the kinematic fitting procedure. The reconstructed mass (Fig. 5.4) is the only discriminating variable used for this analysis; consequently, one of these two events, with a reconstructed mass of $115.2\,\mathrm{GeV}/c^2$, has a relatively high event weight in the final result under the $115\,\mathrm{GeV}/c^2$ Higgs boson mass hypothesis.

5.6 Discussion of Candidates from the Tau Lepton Pair Selection

The event, collected at 208 GeV, has a reconstructed Higgs boson mass of $115.2\,\mathrm{GeV}/c^2$ and is selected by the $b\bar{b}\tau^+\tau^-$ selection with a network output of 0.987. The two

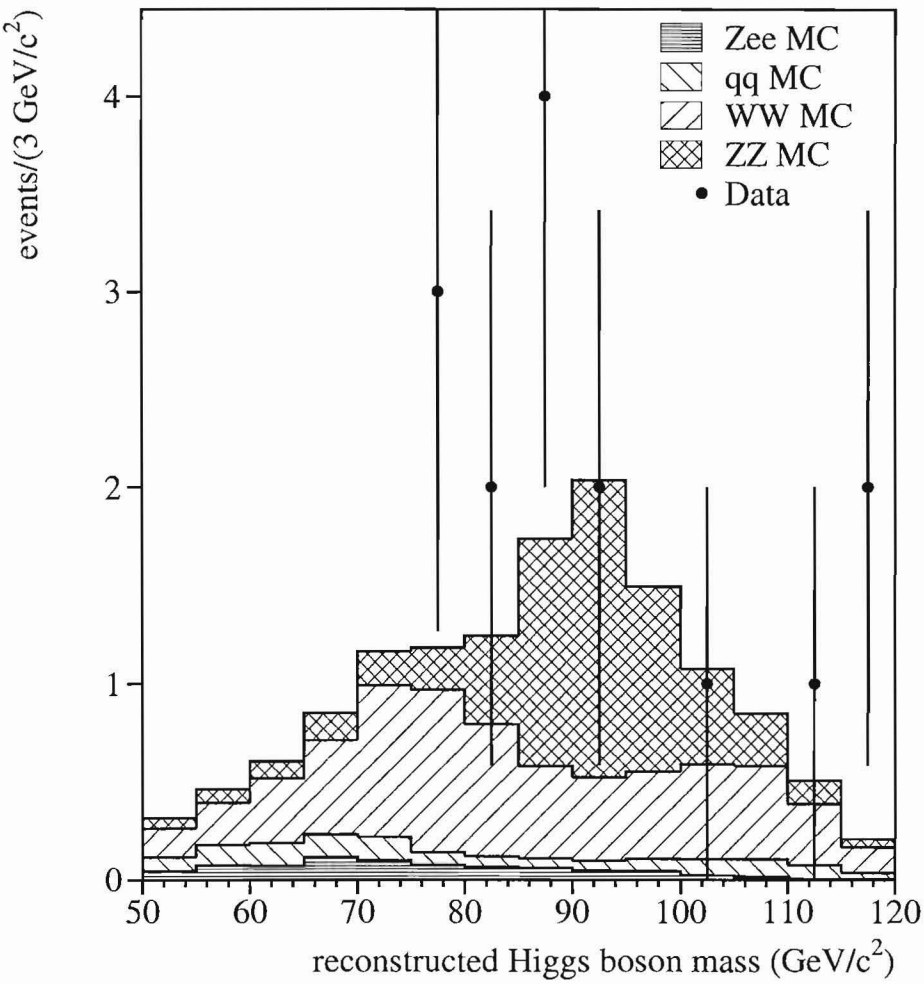

Figure 5.4: Reconstructed Higgs boson mass in selected $\tau^+\tau^-$ events from simulation and data in 2000.

hadronic jets are b-tagged with NN outputs of 0.88 and 0.68, and the identified three-track τ^- is well isolated, both by the isolation angle definition (52°) and by visual inspection (Fig. 5.5). The momentum of the identified τ^+ is only 7.82 GeV/c, but

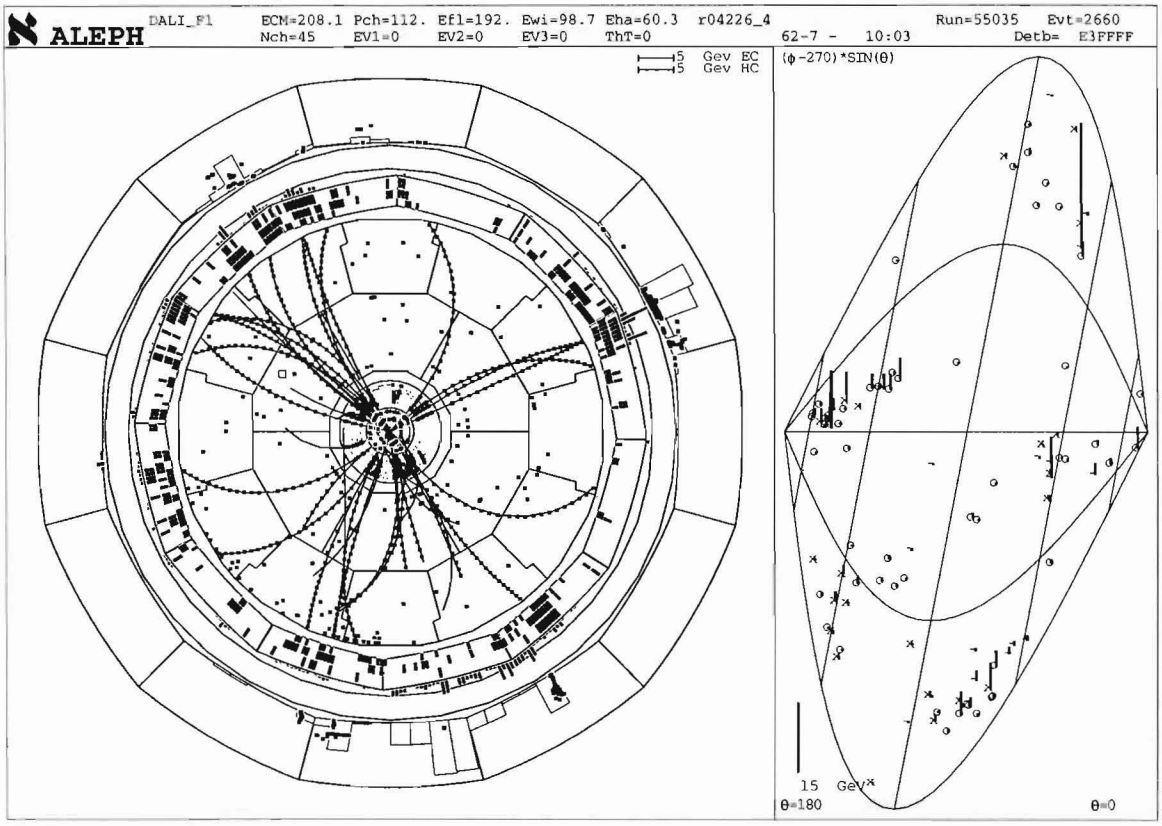

Figure 5.5: Run 55035, event 2660 in the DALI event display. The identified three-track tau lepton is isolated at 2 o'clock in the $x-y$ projection on the left. One of the three tracks is represented by the tall tower in the $\theta - \phi \sin\theta$ plane on the right.

this might be expected for a purported pion from one-prong tau lepton decay. The τ^+ isolation angle is large (59°) because the neighboring particle tracks are all low-energy. The most likely interpretation for this event is $W^+W^- \to \tau^+\nu_\tau\bar{c}s$ production, despite the high b tag value for the hadronic jets.

A second high-mass event (Fig. 5.6), collected at 206.4 GeV, has a reconstructed Higgs boson mass of 117.0 GeV/c^2 and is also selected by the $b\bar{b}\tau^+\tau^-$ selection with

a network output of 0.958. The identified τ^- lepton is classified as a muonic decay with a momentum of 35.1 GeV/c, but the identified τ^+ lepton is classified as a two-track decay with momentum 23.3 GeV/c. A 27 GeV energy deposit in the LCAL

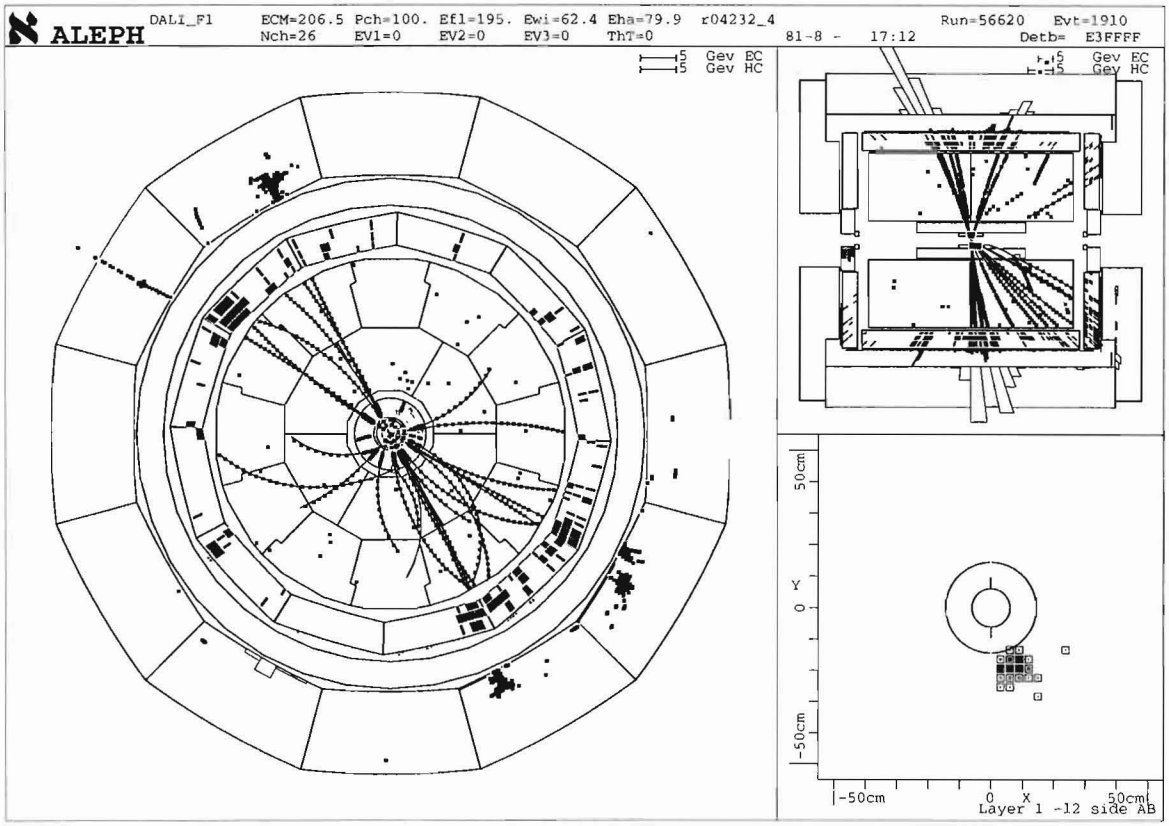

Figure 5.6: Run 56620, event 1910 in the DALI event display. A 27 GeV energy deposit is visible near the beam line in the $r - z$ projection at upper left; the same deposit is shown in the zoomed $x - y$ view of the LCAL at lower right.

contributes to the high reconstructed Higgs boson mass. Even though the deposit is isolated and appears to be consistent with beam-related background, it is clustered into the hadronic jet system, thereby increasing the reconstructed mass.

This event, with a high reconstructed Higgs boson mass, is more likely to have come from background processes than from 115 GeV/c^2 Higgs boson production; as a result, it contributes a low event weight to the combined results.

Chapter 6

Event Selections for Final States with Neutrino, Electron, or Muon Pairs

6.1 Event Selection for Final States with Neutrino Pairs

The final state with a neutrino pair from Z boson decay is characterized by a large missing mass approximately equal to m_Z and two acoplanar jets from the Higgs boson decaying to a $b\bar{b}$ pair. The large branching fraction $\mathcal{B}(Z \to \nu\bar{\nu}) = 20\%$ and the few sources of background contamination make this the second most sensitive search channel.

6.1.1 Preselection

The first requirements – that the number of charged tracks be greater than 4 and that the energy of those charged tracks be greater than $0.1\sqrt{s}$ – ensure the selected events contain hadronic jets. Neither event hemisphere, as defined by the event's thrust axis, may have zero total energy.

One source of background contamination is the contribution from the $\gamma\gamma \to q\bar{q}$ diagram. Events from $\gamma\gamma \to q\bar{q}$ typically have little energy deposited more than 30° from the beam line; therefore, events are kept only if the fraction of energy deposited above 30° is greater than 25% or if the event transverse momentum p_T is greater than $0.05\sqrt{s}$.

The missing mass $\not{M}$ is required to be greater than $50\,\mathrm{GeV}/c^2$. For signal production, the missing mass distribution is peaked at m_Z. (The distribution is peaked at lower $\not{M}$ for Higgs boson masses greater than $\sqrt{s} - m_H$.)

After these preselection cuts, a remaining background process is $e^+e^- \to q\bar{q}\gamma$ with one or two initial state radiation (ISR) photons emitted along the beam line and not detected [60]. To remove events with single energetic ISR photons or with double ISR photons emitted in the same direction, the magnitude of the missing longitudinal momentum $|\not{p}_z|$ must be less than $50\,\mathrm{GeV}/c$.

Events from the background process $e^+e^- \to W^+W^-$ may still pass the missing mass cut, especially in the final state $q\bar{q}\tau\nu$ with two neutrinos from the tau lepton decay. A special set of cuts reject W^+W^- events with a tau lepton, notable by its isolation from the rest of the event. Each event is clustered into minijets using the JADE algorithm [61] with a invariant mass cutoff value of $2E_{vis}/\sqrt{s}$, where E_{vis} is the total visible energy in the event. The minijet most isolated with respect to the other minijets is considered a likely tau lepton candidate and must have less than 10 GeV

of energy. In addition, no charged particle track in the event may be separated by more than 25° from its closest charged particle track neighbor.

This analysis is sensitive to energy deposited near the beam line which often indicates a low-angle radiated photon. Unfortunately, the amount of energy deposited at low angles is also sensitive to effects from beam interactions. For this reason, events are rejected if the energy deposited less than 12° from the beam line is greater than $0.035\sqrt{s}$.

6.1.2 Neural Network Selection

Only event kinematic variables are used in the $H\nu\bar{\nu}$ neural network selection. The final selection discriminates between the $H\nu\bar{\nu}$ signal topology and the dominant $q\bar{q}\gamma$ and W^+W^- background topologies [62].

Input variables which specifically address the separation between $H\nu\bar{\nu}$ and $q\bar{q}\gamma$ are:

1. f_{30}, the fraction of the total event energy deposited more than 30° from the beam line;
2. $\not{p}_T$, the event missing momentum transverse to the beam line;
3. ϕ_{12}, the acoplanarity or difference in azimuth of the two hemispheres' momenta;
4. Θ, the centrality, defined as $\sin\theta_1 \sin\theta_2$, where θ is the polar angle of a hemisphere's momentum; and
5. $E_{\not{p}}^{30}$, the fraction of the total event energy deposited within 30 degrees in azimuth of the missing momentum vector.

Other input variables which specifically address the separation between $H\nu\bar{\nu}$ and W^+W^- are:

1. $\not{p}$, the event missing momentum;

2. A, the acollinearity or angle between the two hemispheres' momenta; and

3. $\not{M}$, the event missing mass.

The b tagging outputs for the two jets are not used in the neural network selection; they are used as discriminant variables during the final calculation of results.

Because the final selection seeks to separate the signal from two dominant classes of background, the network architecture is constructed with three output nodes, one each for $q\bar{q}$, W^+W^-, and $H\nu\bar{\nu}$ signal event types. In this way, the contributions from different background classes can be selected and studied separately. The signal node output from the selection neural network is shown in Fig. 6.1. Events with signal output node values greater than 0.89967 are accepted as $H\nu\bar{\nu}$ candidates.

A reconstructed Higgs boson mass for each selected event is calculated by assuming the recoil mass to be m_Z and rescaling both jet momenta by the same factor [63]. Then the reconstructed Higgs mass is given by

$$M_H = \frac{E_{cm}E_{vis} - \sqrt{E_{cm}^2 E_{vis}^2 - (E_{vis}^2 - p_{vis}^2)(E_{cm}^2 - m_Z^2)}}{\sqrt{E_{vis}^2 - p_{vis}^2}},$$

where E_{cm} is the event center-of-mass energy and E_{vis} is the total visible energy.

6.1.3 Results from Selection

Expected contributions from signal and background processes are shown in Table 6.1. A deliberate effort has been made to exclude the b-tagging information from the $H\nu\bar{\nu}$ event selection. As a result, not all events selected by this selection can truly be considered Higgs candidate events. The $We\nu$ and ZZ backgrounds are kinematically similar to the $H\nu\bar{\nu}$ signal; as a result, their contributions dominate the expected total

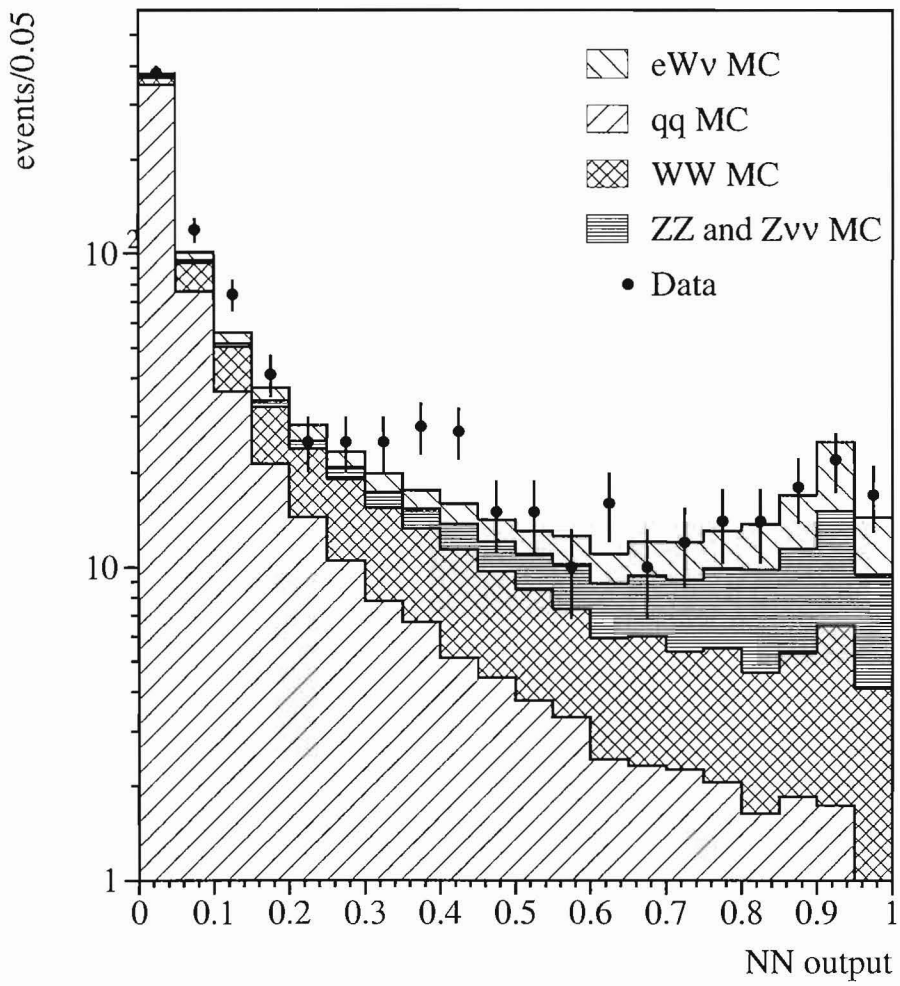

Figure 6.1: Distributions of the $H\nu\bar{\nu}$ selection neural network signal node output in data and simulation. Events with output greater than 0.89967 are selected as candidates.

	Events
Total $H\nu\bar{\nu}$ signal	0.98
$We\nu$	14.14
ZZ	12.56
W^+W^-	7.97
$q\bar{q}$	2.03
$Z\nu\bar{\nu}$	1.01
Ze^+e^-	0.03
Total background	37.74
Observed candidates	39

Table 6.1: Expected and observed number of events with neutrino pairs in 2000. The simulated $H\nu\bar{\nu}$ signal assumes $m_H = 115\,\mathrm{GeV}/c^2$.

background. When applied to the collected data, the analysis selects 39 candidate events. No event, however, has a btag sum greater than 1.0 and a reconstructed Higgs boson mass greater than $108\,\mathrm{GeV}/c^2$. Because the b tag sum (specifically, the b tag sum rarity computed from a simulated signal sample) is used as a discriminating variable along with the reconstructed Higgs boson mass, no single event from this selection contributes significantly to an excess at high mass.

6.2 Event Selection for Final States with Electron or Muon Pairs

The final state with an electron or muon pair from the Z boson decay is a clean topology with excellent Higgs mass resolution. Unfortunately, the rather low branching fractions ($\mathcal{B}(Z \to e^+e^-) = \mathcal{B}(Z \to \mu^+\mu^-) = 3.4\%$) imply a low signal rate for this channel, even though the rate is slightly enhanced by He^+e^- final state contributions from the ZZ-fusion diagram. The basic search strategy is to identify two electrons or muons with invariant mass near m_Z and to calculate the mass of the system recoil-

ing against them. The recoil system may be two hadronic jets or two tau leptons, depending on the Higgs boson decay.

6.2.1 Lepton Identification

Electrons and muons are identified using the standard algorithms presented in Chapter 3. They are considered isolated if the isolation angle, as defined in the search for $\tau^+\tau^-$ final states, is at least 10°. If an electron or muon with $|\cos\theta| \leq 0.95$ is isolated or identified, it is accepted as a lepton candidate track. In general, at least one lepton in a pair must be identified; the other, always of the same flavor, may be either identified or merely isolated.

If a partner cannot be found for an identified lepton candidate track with momentum greater than $20\,\mathrm{GeV}/c$, evidence is sought for a same-flavored lepton with $|\cos\theta| > 0.95$. Dedicated algorithms are used to identify electrons and muons with $|\cos\theta| > 0.95$, near the beamline and outside the tracking acceptance of the TPC. These low-angle electrons and muons are never isolated, by definition. Electrons at low angles are identified by using the ECAL[1] and the ITC. Hits in the ITC with high $|\cos\theta|$ values are associated with an ECAL cluster whose energy is at least 20 GeV. If two or more ITC hits with $|z| > 50\,\mathrm{cm}$ are within 3° in the $r - \phi$ plane of the ECAL cluster, then the cluster is identified as a low-angle electron. The energy of the low-angle electron is taken from the total energy in the ECAL cluster. Muons at low angles are identified by using the muon chambers and the HCAL. Every low-angle HCAL cluster with energy between 2 and 10 GeV is considered as a possible muon candidate. To be identified, a cluster must have at least six hits in the last ten planes of the HCAL and must have one hit either in the last two HCAL planes or in the two

[1]For this purpose, the LCAL is treated as a low-angle extension of the ECAL.

muon chambers. The energy of the low-angle muon is determined from an overconstrained event fit. Energy and momentum conservation provide four constraints; the free parameters are the momenta of the two hadronic jets and the momentum of the muon. (The identified and well-measured muon is removed explicitly for this fit.)

6.2.2 Mass Reconstruction

The reconstructed mass of the putative Higgs boson is identified as the invariant mass of the system recoiling against the electron or muon pair. The Higgs boson mass resolution is improved by correcting the invariant mass of the lepton pair for bremsstrahlung and final state radiation photons.

The first correction for bremsstrahlung radiation applies only to events with two identified electrons. Photons emitted as bremsstrahlung are absorbed and measured in the ECAL. If the photon energy is a large fraction of the original electron energy, then the total ECAL energy provides an accurate measurement of the electron energy. If, on the other hand, the photon energy is small compared to the original electron energy, then the measurement of the track momentum in the TPC is the most accurate gauge of the electron energy. The photon energy is seldom in one of these two limiting cases, so the results from the two methods are combined. The relative weights of the methods' contributions are calculated using the error function to ensure a smooth progression from track momentum measurement to ECAL energy measurement [64]. If an electron is not isolated, it is difficult to distinguish electron-related energy flow objects from jet-related energy flow objects; therefore, no bremsstrahlung correction is applied to that electron candidate.

The second correction to the electron or muon pair invariant mass recovers a possible final state radiation (FSR) photon from the decay of the Z boson. A photon

is considered an FSR photon candidate if its energy is at least 2 GeV and its isolation angle with respect to the hadronic system is at least 10°. If the addition of the photon to the electron or muon pair moves the invariant mass of the system toward $91.2\,\mathrm{GeV}/c^2$, then the photon is included in the system for the final calculation of the reconstructed mass.

6.2.3 Event Selection

Events with no identified leptons or with an identified electron-muon pair are rejected. A candidate event must have at least 4 good charged particle tracks (or 3 good charged particle tracks in addition to a low-angle lepton) and a total charged particle energy at least 10% of the center-of-mass energy.

Events with an initial state radiation photon are rejected, as in the tau lepton search channels, by requiring the most energetic isolated photon have energy less than $0.75E_\gamma^{\mathrm{peak}}$. Electrons from the conversion of a high energy photon are identified by calculating an electron-positron pair's invariant mass and specific ionization in the TPC. An event is rejected if the $\ell^+\ell^-$ pair has invariant mass less than $0.05\,\mathrm{GeV}/c^2$ or if the ionization of two indistinct high-momentum tracks together is more than 10σ from the ionization expected for an electron.

If more than one pair of electrons or muons is found in the event, the pair whose corrected invariant mass is closest to m_{Z} is selected. The sum of the selected leptons' transverse momenta with respect to the nearest hadronic jets must be greater than $20\,\mathrm{GeV}/c$. This cut removes $\mathrm{e^+e^-} \to \mathrm{q\bar{q}}$ events in which hadronic jets contain semileptonic decays.

Often a $\mathrm{W^+W^-} \to \mathrm{q\bar{q}}\ell\nu$ event can be selected if the identified lepton is paired with an isolated track from a hadronic jet. Cuts to remove such events are based

on explicit reconstruction of the W bosons. The invariant mass of the identified lepton and the missing momentum vector is calculated as $m_{\mathrm{W}}^{\mathrm{lept}}$, while the invariant mass of the rest of the event is calculated as $m_{\mathrm{W}}^{\mathrm{hadr}}$. The event is rejected if both $m_{\mathrm{W}}^{\mathrm{hadr}} + m_{\mathrm{W}}^{\mathrm{lept}} > 150\,\mathrm{GeV}/c^2$ and $m_{\mathrm{W}}^{\mathrm{hadr}} - m_{\mathrm{W}}^{\mathrm{lept}} < 20\,\mathrm{GeV}/c^2$.

Both recoiling jets are required to have at least one charged particle track in order to remove potential $\ell^+\ell^-\gamma\gamma$ background events with a photon conversion. Events with $\mathrm{Z}\gamma^\star \to \mathrm{Z}\ell^+\ell^-$ are removed by requiring the sum of the invariant masses of the identified electron or muon pair and the recoil system be greater than $115\,\mathrm{GeV}/c^2$.

The tau lepton identification algorithm, as introduced in Chapter 5, is used to identify tau leptons from Higgs decay. Because the $\mathrm{q\bar{q}}$ background level is already reduced by the requirement of two identified leptons, the charged jet mass of the tau lepton candidate is required to be only $1.8\,\mathrm{GeV}/c^2$ instead of $2.7\,\mathrm{GeV}/c^2$. This change increases the identification efficiency for isolated tau leptons. Events with exactly four good charged tracks are good candidates for $(\mathrm{H} \to \tau^+\tau^-)\ell^+\ell^-$, and they are required to have missing energy, as expected from τ decay, of at least $0.1\sqrt{s}$. For identified $\tau^-\tau^-\ell^+\ell^-$ events, the $\mathrm{W}^+\mathrm{W}^-$ hypothesis event rejection cuts are dropped.

The final cut in the $\mathrm{H}\ell^+\ell^-$ event selection requires the reconstructed Z boson mass $M_{\ell^+\ell^-}$ be greater than $77.0\,\mathrm{GeV}/c^2$.

6.2.4 Results from Selection

Expected contributions from background and signal processes are shown in Table 6.2.

The b content of the hadronic jets is not used in the selection. As a result, the $\mathrm{H}\ell^+\ell^-$ selection maintains sensitivity to Higgs bosons decaying to tau lepton pairs in the $\tau^+\tau^-\ell^+\ell^-$ final state. The value of the b/τ tag and the reconstructed Higgs

	Events
Total $H\ell^+\ell^-$ signal	0.43
ZZ	21.72
Ze^+e^-	4.81
W^+W^-	2.42
$q\bar{q}$	1.81
Total bkgd.	30.77
Observed candidates	30

Table 6.2: Expected and observed number of $H\ell^+\ell^-$ events in 2000. The simulated $H\ell^+\ell^-$ signal assumes $m_H = 115\,\mathrm{GeV}/c^2$.

boson mass are used as discriminating variables in the confidence level calculation. When an event contains two identified tau lepton candidates, the b/τ tag value is set to 2; otherwise, the b/τ tag value is the sum of the b-tagging NN outputs for the two hadronic jets. A large number of the 30 selected candidates, especially those from $We\nu$ and W^+W^- diagrams, are deweighted by their low b/τ tag values. In fact, only one selected event has both a reconstructed mass greater than $108\,\mathrm{GeV}/c^2$ and a b-tag sum greater than 1.0. It is therefore the only $H\ell^+\ell^-$ event which has a significant event weight under a Higgs boson mass hypothesis of $115\,\mathrm{GeV}/c^2$, the mass hypothesis favored by the observed excess in the $Hq\bar{q}$ channel.

6.3 Discussion of Candidate from the Electron Pair Selection

The event, collected at $\sqrt{s} = 205.1\,\mathrm{GeV}$, has a lepton pair invariant mass of $79.3\,\mathrm{GeV}/c^2$ and a reconstructed Higgs boson mass of $117.3\,\mathrm{GeV}/c^2$. One hadronic jet has a b-tag output of 0.996; the other has an output of 0.421. The $43\,\mathrm{GeV}/c$ positron is well isolated, as seen in Fig. 6.2, but the $39\,\mathrm{GeV}/c$ electron is only 6° away from a

hadronic jet. The bremsstrahlung correction in this analysis is not applied if an iden-

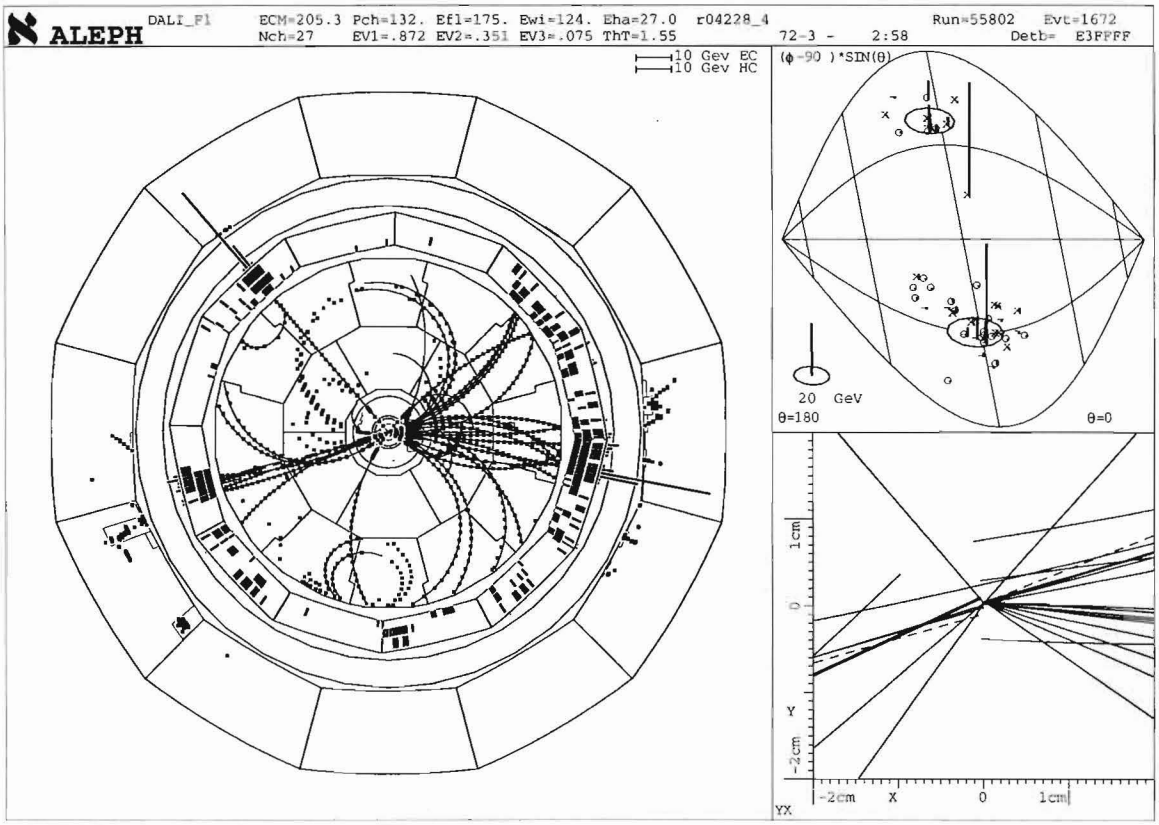

Figure 6.2: Run 55802, event 1672 in the DALI event display. The electron and positron are easily identified by the energy deposits visible in the $x - y$ projection at left and by the tall towers in the $\theta - \phi \sin\theta$ plane at top right. One hadronic jet is broad with high multiplicity, and the other jet contains a secondary vertex, visible in the zoomed $x - y$ projection at bottom right.

tified electron is isolated by less than 10° from a jet; consequently 18 GeV of neutral electromagnetic energy within 2° of the electron are not treated as bremsstrahlung energy. If these energy flow objects were added to the electron, the invariant mass of the lepton pair would be 93.5 GeV/c^2, and the reconstructed Higgs boson mass would decrease to 99.4 GeV/c^2. In that case, the most likely hypothesis for the event is ZZ production.

Chapter 7

Statistical Interpretation and Combination of Results

In simplest terms, the statistical interpretation of the search results tests two complementary hypotheses in the context of Higgs boson production. The first hypothesis, that the observed data are due to background production only, corresponds to the classic null hypothesis; the second, that the data are due to signal plus background production, corresponds to the classic alternative hypothesis.

This chapter describes the method used to combine the results from the individual search channels. These results are then interpreted quantitatively by calculating confidence levels for each of the two hypotheses.

7.1 Confidence Level Calculation using a Test Statistic

The confidence level calculation follows a three-step outline.

1. A test statistic is used to quantify the "signal-ness" of an event or a set of events such that a greater test statistic value implies a more signal-like set.

2. Expected test statistic distributions are calculated for a set of events simulated under the background-only hypothesis and for a set of events simulated under the signal+background hypothesis.

3. The probability to observe a dataset more background-like than the experimentally observed dataset is computed under each of the two hypotheses.

This calculation framework builds on the proposal introduced in Ref. [65].

7.2 The Likelihood Ratio as Test Statistic

The test statistic used in this analysis is the likelihood ratio. The likelihood ratio can be shown, via the Neyman-Pearson lemma, to be the optimal test statistic for testing a null hypothesis against a simple alternative hypothesis [66, 67].

Ultimately, the purpose of the test statistic is to measure the "signal-ness" of each event and to assign an event weight accordingly. An event's weight is calculated based on the values of its discriminant variables, typically the reconstructed Higgs boson mass and the sum of b tag outputs for two hadronic jets. Fundamentally, the likelihood ratio Q in a single search channel is

$$Q = \frac{\mathcal{L}_{s+b}}{\mathcal{L}_b} = e^{-s} \prod_{i=1}^{n_{\text{obs}}} \frac{s f_s(\overrightarrow{x_i}) + b f_b(\overrightarrow{x_i})}{b f_b(\overrightarrow{x_i})},$$

where s and b are the expected number of signal and background events in the search channel, n_{obs} is the number of observed events, and f_s and f_b are the probability density functions of the vector of event discriminant variable values $\overrightarrow{x_i}$. The prob-

ability density functions are generated from events in Monte Carlo simulation, and the expected number of signal and background events are calculated from run-by-run records of luminosity and center-of-mass energy and from expected cross sections. For computational purposes, the functions are smoothed with a kernel estimation algorithm [68] and interpolated with a histogram morphing algorithm [69].

Each individual event, simulated or observed, is subsequently assigned an event weight $w_i = \ln[1 + s f_{\mathrm{s}}(\overrightarrow{x_i})/b f_{\mathrm{b}}(\overrightarrow{x_i})]$, representing that event's contribution to the signal-ness of the dataset[1]. A high event weight implies that a candidate is more likely to have come from signal+background production than from background-only production. By definition, event weights vary with expected number of signal events and consequently with the Higgs boson mass hypothesis. Among the 137 ALEPH candidates selected in 2000, six have event weights greater than 0.4 for the 115 GeV/c^2 mass hypothesis (Fig. 7.1).

The three greatest event weights belong to the four-jet events discussed in Chapter 4, but the $\mathrm{He^+e^-}$ event and the $\mathrm{H}\tau^+\tau^-$ event also contribute relatively high event weights for a Higgs boson mass hypothesis of 115 GeV/c^2. The results from searches in 2000 are combined with search results from data taken in 1998 and 1999 at center-of-mass energies between 189 and 202 GeV/c^2. Even so, the low Higgs signal production cross section for $m_{\mathrm{H}} > \sqrt{s} - m_{\mathrm{Z}}$ implies low event weights at high Higgs boson mass hypotheses for events selected in lower-energy data.

[1]Clearly, an event weight must be calculated in the context of only one analysis. To maintain the exclusivity of the selections, a strict veto is maintained in the order $\mathrm{H}\tau^+\tau^-$, $\mathrm{H}\ell^+\ell^-$, $\mathrm{Hq\bar{q}}$, and $\mathrm{H}\nu\bar{\nu}$. That is, the rare candidate selected by both $\mathrm{H}\tau^+\tau^-$ and $\mathrm{H}\ell^+\ell^-$ would be considered a $\mathrm{H}\tau^+\tau^-$ candidate for the purpose of event weight calculation.

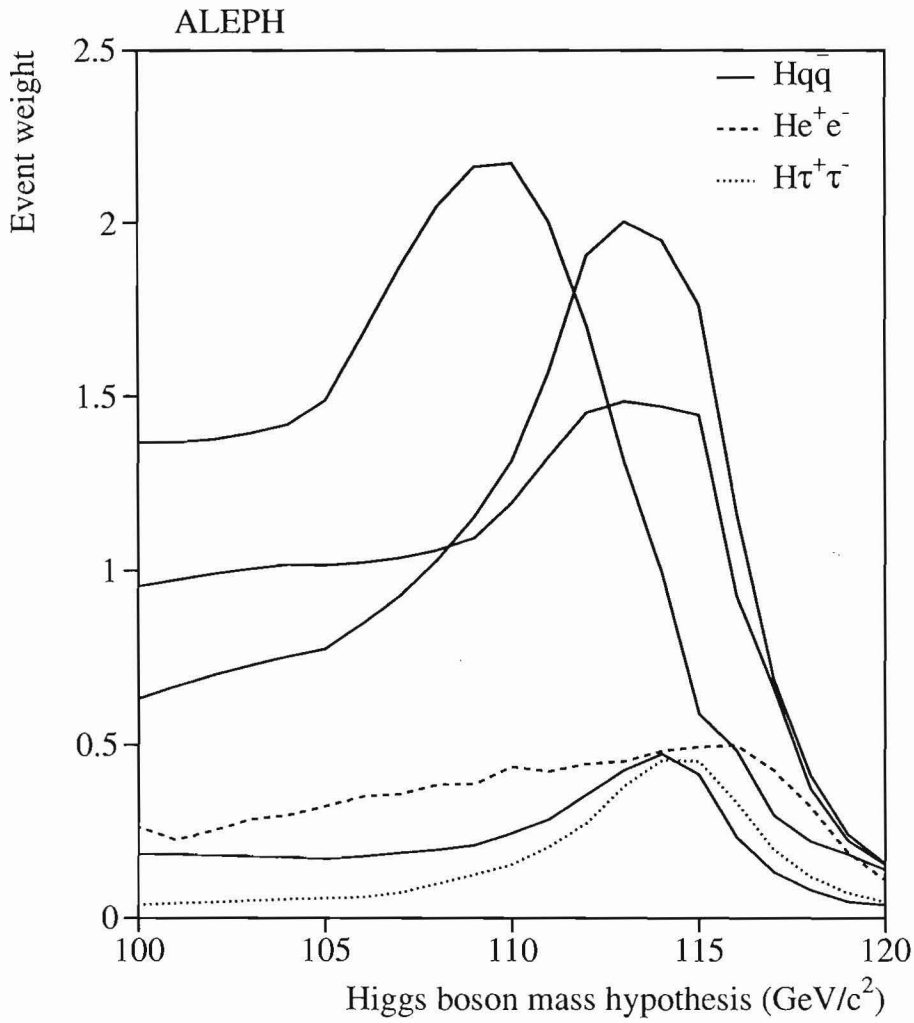

Figure 7.1: Event weights of individual Higgs candidate events as a function of the Higgs boson mass hypothesis. Of the 137 candidates in the 2000 ALEPH data, only those with weight greater than 0.4 at $m_{\mathrm{H}} = 115\,\mathrm{GeV}/c^2$ are plotted here. The weights of the four-jet candidates are shown with solid lines, those of the electron pair candidate with a dashed line, and those of the tau lepton pair candidate with a dotted line.

7.3 Test Statistic Distributions for Event Ensembles

In order to compare the observed value of the test statistic to the expected values under the two hypotheses, it is first necessary to calculate the test statistic for a group of events, be it one search channel or an entire dataset. The likelihood ratio for a ensemble of events is just the product of likelihood ratio factors for the individual events. Since the likelihood ratio for each search channel has a leading factor of e^{-s}, the total combined likelihood ratio takes the form

$$\ln Q = -s_{\text{tot}} + \sum_{k=1}^{n_{\text{tot}}} n_k w_k$$

where n_{tot} is the total number of events observed, s_{tot} the expected number of signal events, n_k the number of events observed in a specific channel, and w_k the event weight.

One way to form the normalized test statistic probability density function ρ_{s+b} for an ensemble of signal and background events is to generate a large number of toy Monte Carlo experiments and then calculate the test statistic directly for each generated ensemble. This technique is straightforward but computationally intensive, especially if a high level of precision is required.

An alternative approach is to calculate analytically the test statistic distribution using the expected number of signal and background events and the test statistic distribution expected for a single event [70]. The analytic method, which uses the Fourier transform, is based on the relation

$$\overline{\rho_{s+b}(G)} = e^{(s+b)\left[\overline{\rho_1(G)}-1\right]},$$

where G is the transform domain of the log-likelihood function domain. The result, which is motivated and derived in detail in Appendix A, depends on the fundamental equality between the Fourier transform of a convolution and the product of individual transforms. Because its analytic nature implies high precision and fast computation, this technique is used for the combination instead of the toy Monte Carlo approach.

Given the multiplicative properties of the likelihood ratio test statistic, the combination of results from several searches follows intuitively. The likelihood ratio for the combination of searches is simply the product of the searches' individual likelihood ratios. This construction parallels the calculation of the likelihood ratio for an ensemble of events within a single search channel.

Specifically, for a combination of N search channels,

$$\begin{aligned}\overline{\rho_{s+b}(G)} &= \prod_{j=1}^{N} \overline{\rho^{j}_{s+b}(G)} \\ &= e^{\sum_{j=1}^{N}(s_j+b_j)\left[\overline{\rho^{j}_{1}(G)}-1\right]},\end{aligned}$$

so that the intrinsic sensitivity of each individual analysis is automatically preserved through the contribution of its likelihood ratio.

In Fig. 7.2, the likelihood ratio probability density functions for signal+background and background-only production are plotted with the observed likelihood ratio for each of the four final state search channels. A likelihood ratio value favoring signal+background production, for a specific Higgs boson mass hypothesis of 115 GeV/c^2, is observed in three of the four final states. The combined result, shown in Fig. 7.3, is dominated by the excess from the most powerful search channel, the four-jet channel.

When likelihood ratios are calculated for other Higgs boson mass hypotheses

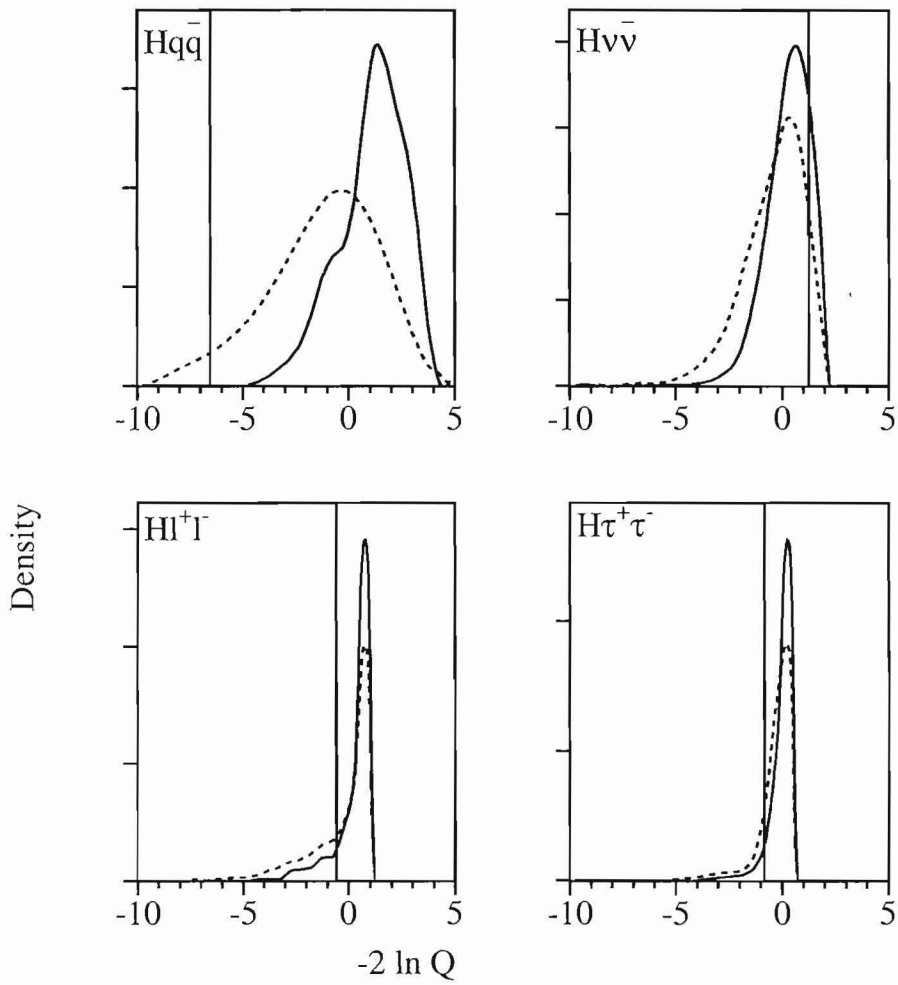

Figure 7.2: Log likelihood ratio distributions for individual ALEPH final state search channels under the 115 GeV/c^2 Higgs boson mass hypothesis. In each plot, the solid vertical line marks the observed value of the likelihood ratio. The background-only distribution is shown with a solid curve, and the signal+background distribution is shown with a dashed curve.

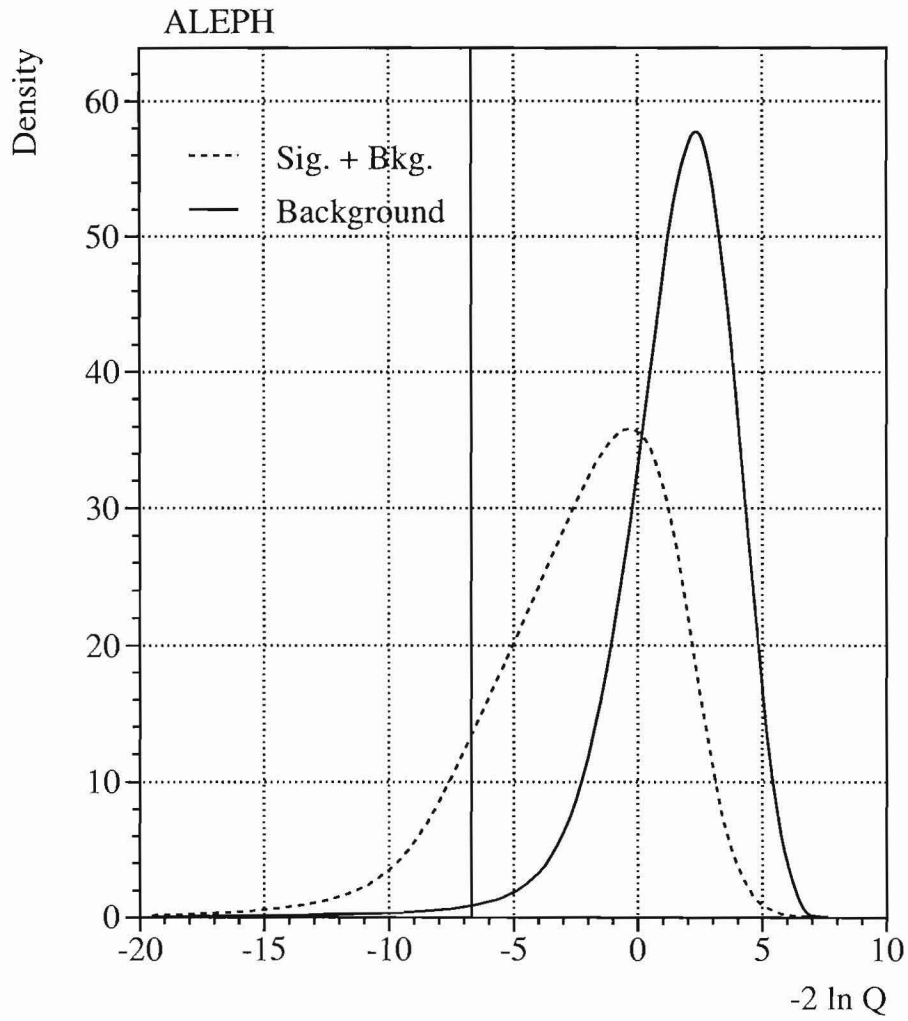

Figure 7.3: Log likelihood ratio distributions for all ALEPH searches combined under the 115 GeV/c^2 Higgs boson mass hypothesis. The observed likelihood ratio value (solid vertical line) lies in the signal-like tail of both the background-only and the signal+background distributions, plotted as solid and dashed lines, respectively.

(Fig. 7.4), the distributions expected from signal+background and background-only production are different, as are the observed likelihood ratio values. Nevertheless, a plot of the combined result for $-2\ln Q$ over a wide range of Higgs boson mass hypotheses in Fig. 7.5 clearly shows a minimum for the $m_{\mathrm{H}} = 115\,\mathrm{GeV}/c^2$ hypothesis, indicating that this signal mass hypothesis is most favored.

7.4 Confidence Integral Calculations

The expected and observed likelihood ratio results for a single mass hypothesis, as shown in Figs. 7.2 and 7.3, can be used to state quantitatively the degree of confidence in that hypothesis. In this case, the confidence integral is defined as the probability that a dataset be more background-like than the observed dataset.[2] Because the likelihood ratio test statistic Q increases monotonically with more signal-like events or ensembles, the confidence integral is defined as an integral over the ensemble test statistic probability density function

$$c \equiv \int_{-2\ln Q_{\mathrm{obs}}}^{+\infty} \rho(-2\ln Q)\mathrm{d}(-2\ln Q),$$

so that c_b is calculated by integrating over ρ_{b}, and c_{s+b} is calculated by integrating over $\rho_{\mathrm{s+b}}$.

The complement of the confidence integral for the background-only hypothesis, $1 - c_b$, gives a measure of the probability for a fluctuation in the background-only production to account for the observed dataset. It is convenient to associate a $1 - c_b$ value with an equivalent number of standard deviations. To compute the significance

[2]The confidence integral is the same quantity described elsewhere as the confidence [66] or the confidence coefficient [65]. In fact, confidence integral values of 0.99 and 0.01 imply the same amount of confidence in the hypothesis under test.

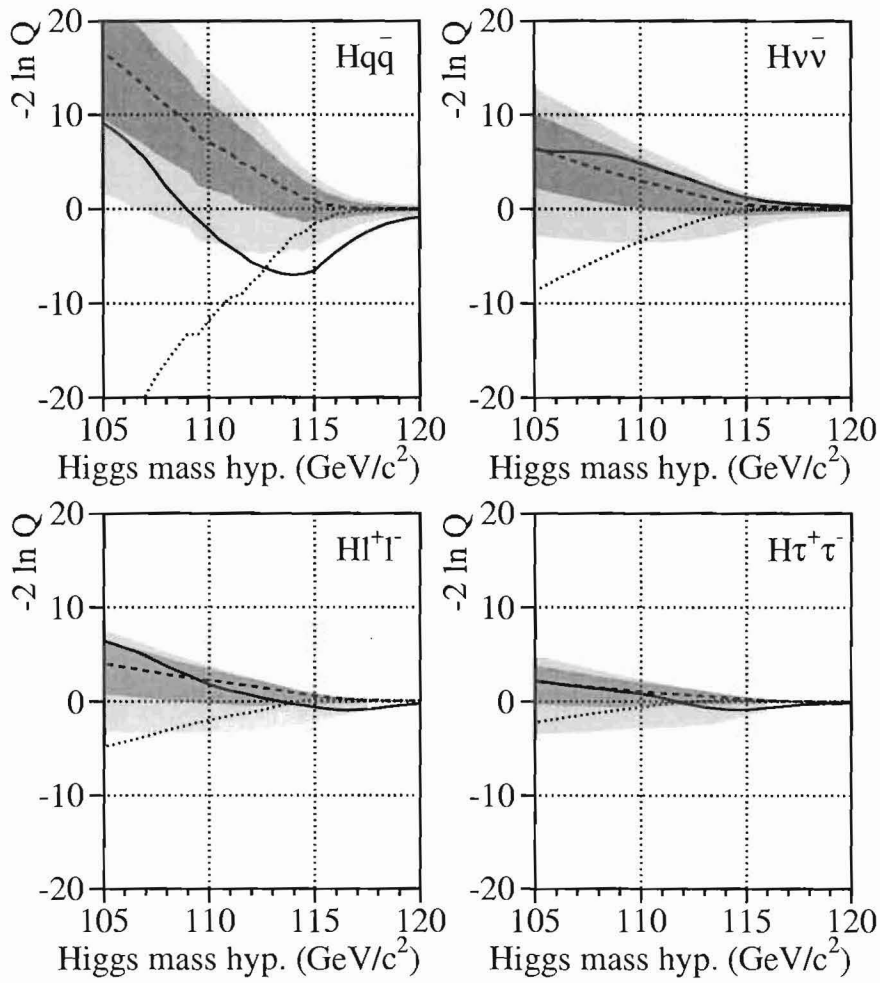

Figure 7.4: Values of $-2\ln Q$ for individual ALEPH final state search channels plotted as a function of the Higgs boson mass hypothesis. The dashed line descending from the top shows the median expected values for a dataset due to background-only production, and the flanking dark and light gray bands represent the 68% and 95% excursions from the median. The values for the observed dataset are plotted as a solid line. The dotted line ascending from the bottom shows the median expected values for simulated datasets due to signal+background production, with the generated Higgs mass equal to the Higgs mass hypothesis.

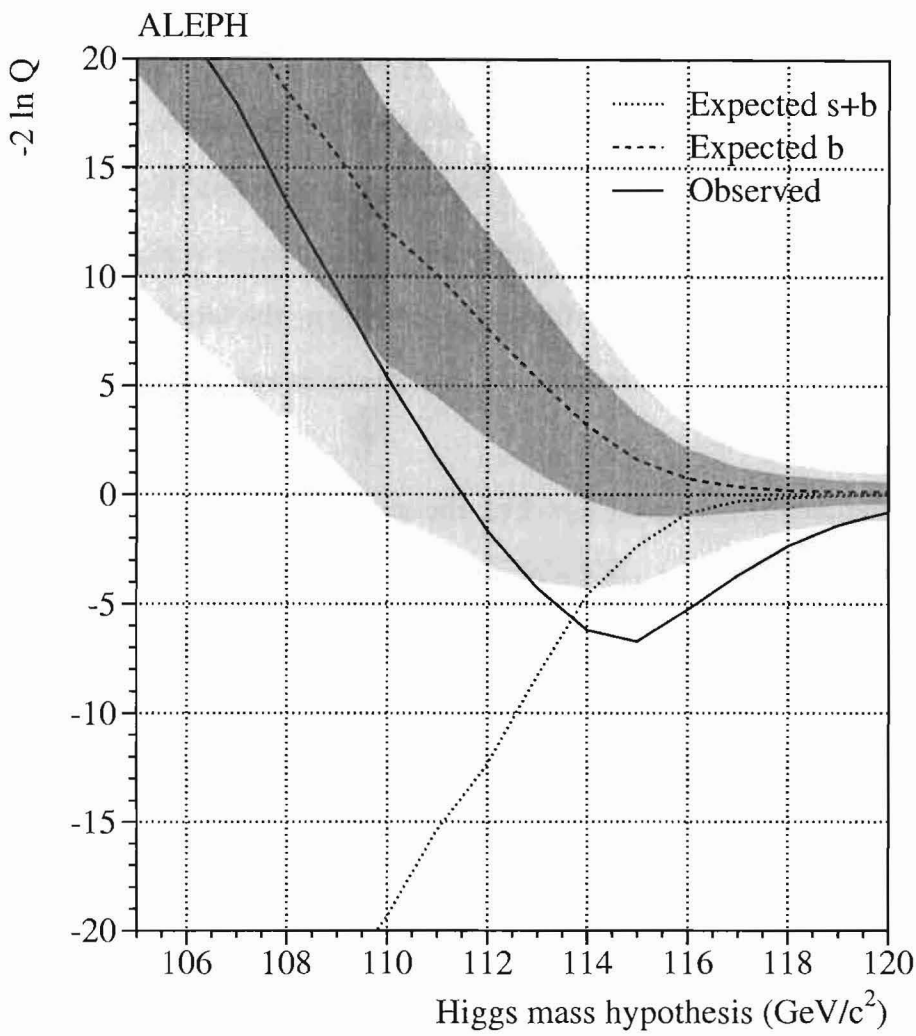

Figure 7.5: The combined log likelihood ratio $-2\ln Q$ plotted as a function of the Higgs boson mass hypothesis. The values for the observed ALEPH dataset, plotted as a solid line, reach a global minimum for a Higgs boson mass hypothesis of 115 GeV/c^2.

of an excess, the $1 - c_b$ value is identified as the area in the tails of the normal distribution. (By this definition, $1-c_b = 5.7\times10^{-7}$ corresponds to a 5σ excess [1, 66].)

The value of $1 - c_b$ at a given mass hypothesis gives only the probability that the background-only distribution account for the observed likelihood ratio at that mass. The number of mass hypotheses tested which are already experimentally excluded or beyond the experimental sensitivity should somehow be taken into account. Studies by the LEP Higgs Working Group have shown the correction factor to c_b due to this "look-elsewhere" effect is roughly the width of the search region divided by the Higgs signal mass resolution [71]. For this search, then, the factor is close to 1; the calculated c_b for a single Higgs boson mass hypothesis is representative of the c_b for the experiment as a whole.

For the combined Higgs boson searches, the minimum value of $1 - c_b$ is 2.4×10^{-3} at a mass hypothesis $m_{\mathrm{H}} = 117\,\mathrm{GeV}/c^2$. Such a probability is equivalent to an excursion of 3.0 normal standard deviations. While the hypothesis of background-only production is therefore unlikely, the observed dataset is also more signal-like than the median expected from signal+background production, as shown in Fig. 7.7. The mass hypothesis at which the minimum occurs depends both on the observed value of the likelihood ratio and the width of the expected background-only distribution. The narrower width of the expected background-only distribution in the $117\,\mathrm{GeV}/c^2$ mass hypothesis, stemming from a smaller HZ cross section, compensates for the more extreme observed likelihood ratio value in the $115\,\mathrm{GeV}/c^2$ hypothesis.

The final reprocessing of the year 2000 data has not changed significantly the minimum value of $1 - c_b$ with respect to the result obtained with online processing and published in Ref. [58]. In addition, a set of parallel analyses using cuts-based selections for the $\mathrm{Hq\bar{q}}$ and $\mathrm{H}\nu\bar{\nu}$ final states [54] observes a 3.3σ excess, despite sacrificing sensitivity by using only one discriminant variable in the likelihood ratio calculation.

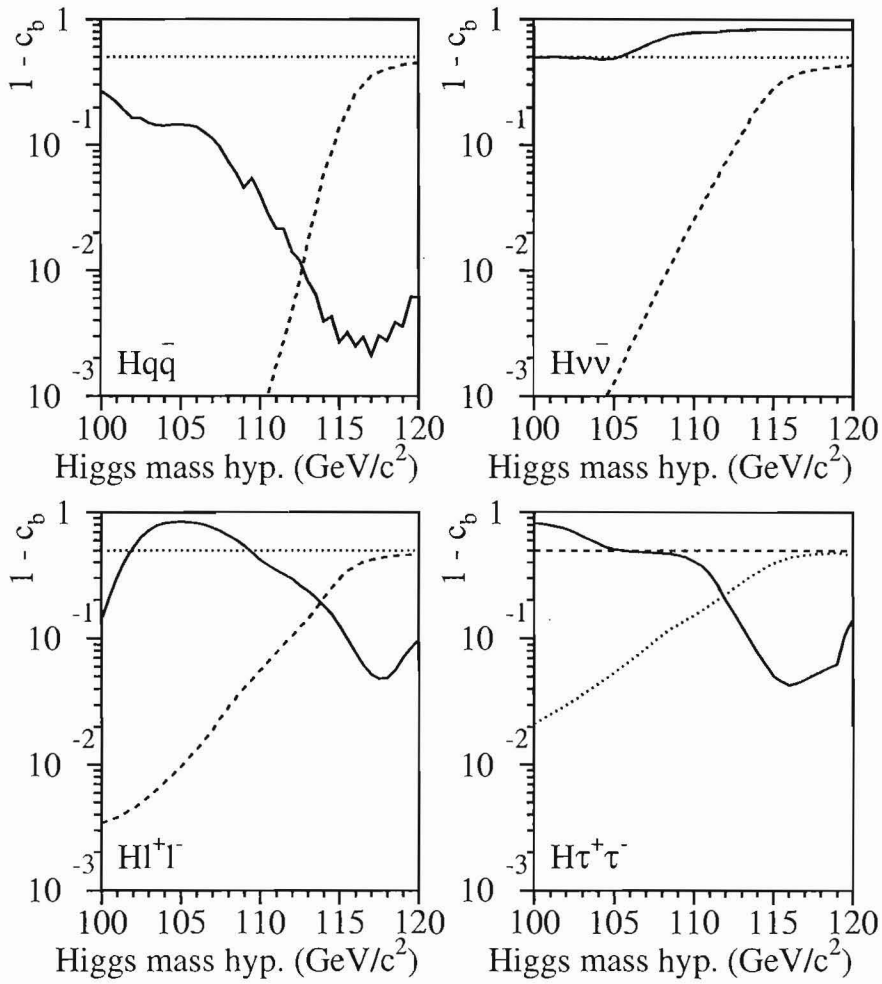

Figure 7.6: Confidence integrals for the background-only production hypothesis for different ALEPH search channels as a function of Higgs boson mass hypothesis. The solid line shows the confidence integral for the background-only hypothesis calculated from the observed dataset. The dotted line at top represents the median confidence integral expected for the background-only dataset (equal to 0.5 by construction since half of the expected distribution is more signal-like than the median), while the dashed line illustrates the median confidence integral expected for datasets with combined signal and background production.

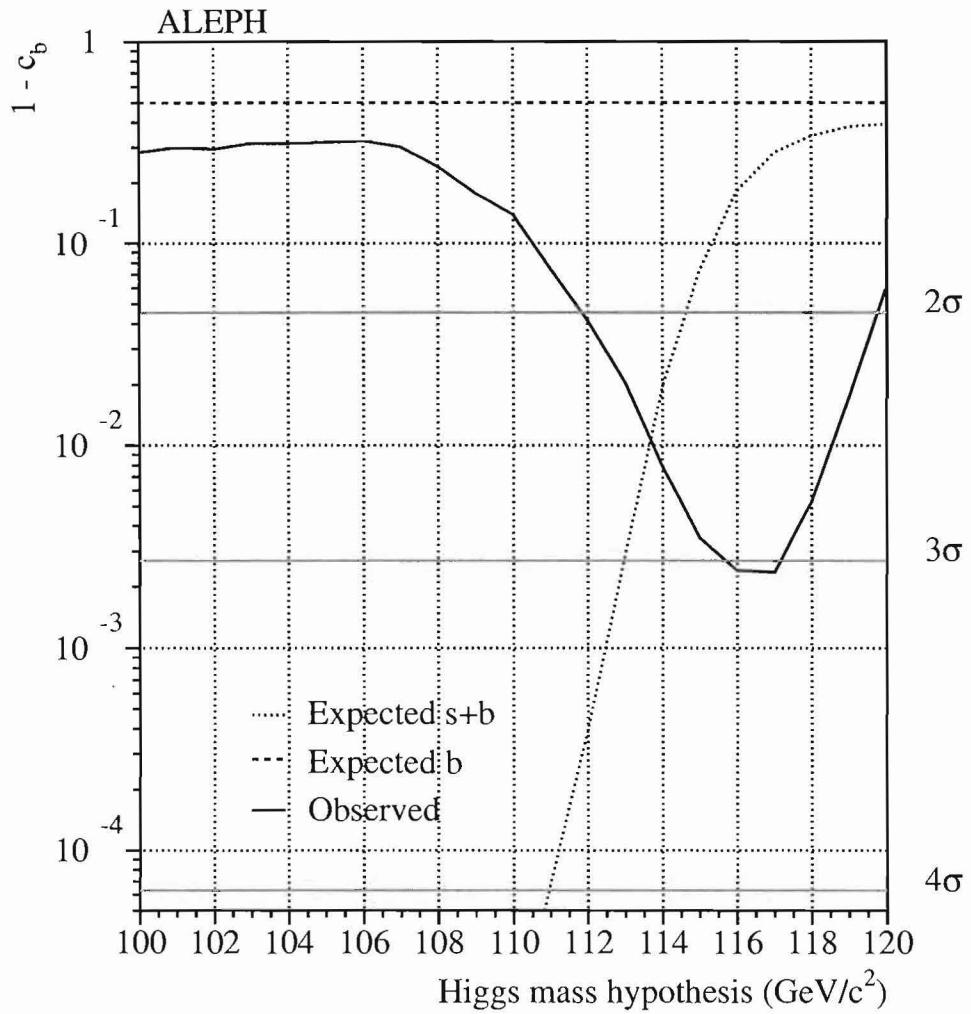

Figure 7.7: Combined confidence integral for the background-only production hypothesis as a function of Higgs boson mass hypothesis. The complement of the confidence integral is plotted to make the excursions more clear. Results from the observed ALEPH dataset are plotted as a solid line. The median expected results from a background-only distribution are plotted as a dashed line, and the median expected results from a signal+background distribution are plotted as a dotted line. On the right side, normal standard deviation equivalents are associated to values of $1 - c_b$.

The overlap of candidates between the cuts and neural network selections is large; both select the same three high-weight four-jet candidates.

7.5 Higgs Boson Mass Limit Calculations

Although the calculations described above give confidence integrals for the background-only and signal+background hypotheses, they cannot give a confidence integral for the signal hypothesis by itself because it is impossible to obtain a signal-only ensemble distribution. After all, if signal and background could be perfectly discriminated, the data analysis would separate the two. In the end, fluctuations in signal production and background production are entangled in c_{s+b}. For example, if the number of candidates observed is much less than the number expected due to background-only production, then even a signal hypothesis of zero events expected could be excluded, based on a downward fluctuation of the background.

The signal estimator method [72] is used as an *ad hoc* approximation to calculate c_s from the confidence integrals c_{s+b} and c_b:

$$c_s \equiv c_{s+b} + (1 - c_b)e^{-s}.$$

By design, the signal estimator formula, while accounting for possible fluctuations in background contribution to the observed dataset, is conservative with $c_s > c_{s+b}$. In particular, for zero events observed, the c_s value is independent of the expected number of background. The advantage of the method, over the one described in Ref. [73], is that the signal estimator c_s more nearly approaches c_{s+b}, making it a closer approximation for calculating exclusion limits. Technically, the construction imposes a physical boundary on the number of signal events in the observed sample, specifically

$n_s^{\text{obs}} \geq 0$. Even though the c_s calculated in this way is not strictly a confidence integral as previously defined, it serves as an approximation to the confidence integral which might be obtained from a signal-only (background-free) distribution.

Given the confidence integral c_s for a specific signal hypothesis, that hypothesis will be defined as being excluded at $1 - c_s$ confidence level (CL) [65]. Although the likelihood ratio is effective in testing a single signal production hypothesis at a time, nothing prevents testing in series a number of distinct signal production hypotheses, each corresponding to a different Higgs boson mass. In this case, the 95% CL lower limit on the Higgs boson mass is the high end of the range of mass hypotheses which are excluded to at least 95% CL. (This definition of a limit is different from the frequentist usage of confidence intervals because its false exclusion rate is lower than the rate implied by the confidence level [66, 74].)

The observed exclusion limit is supplemented by the expected exclusion limit, based on the median confidence integral obtained in a set of background-only thought experiments. Since a search, in the absence of signal, should exclude as large a mass range as possible, the expected limit is useful as a measure of the power of the search.

The exclusion of the signal hypothesis over a range of Higgs boson mass hypotheses is shown in Fig. 7.8 for each of the four final state analyses and in Fig. 7.9 for the combined analyses. The gap between the expected and observed exclusion curves in the $\mathrm{Hq\bar{q}}$ channel is due to the observed excess; the gap in the $\mathrm{H}\nu\bar{\nu}$ channel is due to an observed deficit. Table 7.1 summarizes the 95% CL exclusions from the individual searches and from their combination.

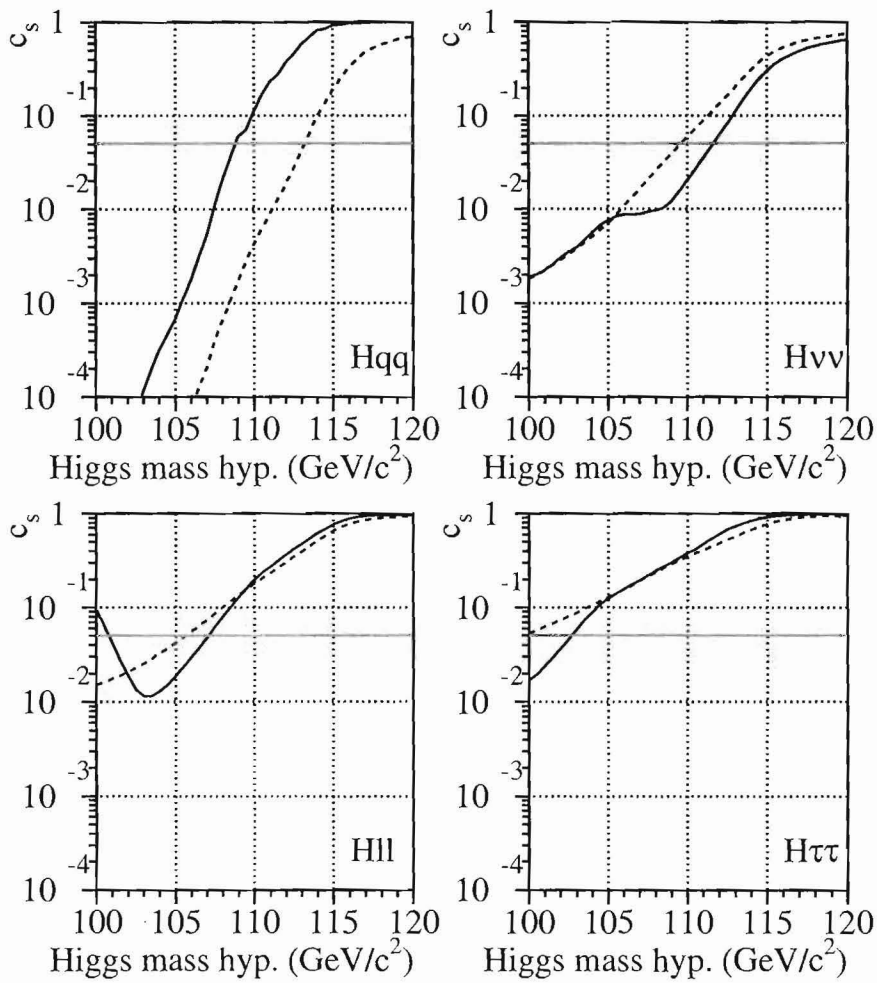

Figure 7.8: Signal hypothesis exclusion, computed with the signal estimator method, for different Higgs boson mass hypotheses in the individual ALEPH search channels. The observed and expected confidence integrals are plotted as solid and dashed lines, respectively. The 95% confidence level limit is defined as the crossing point of the confidence integral curve and the solid horizontal line at 0.05.

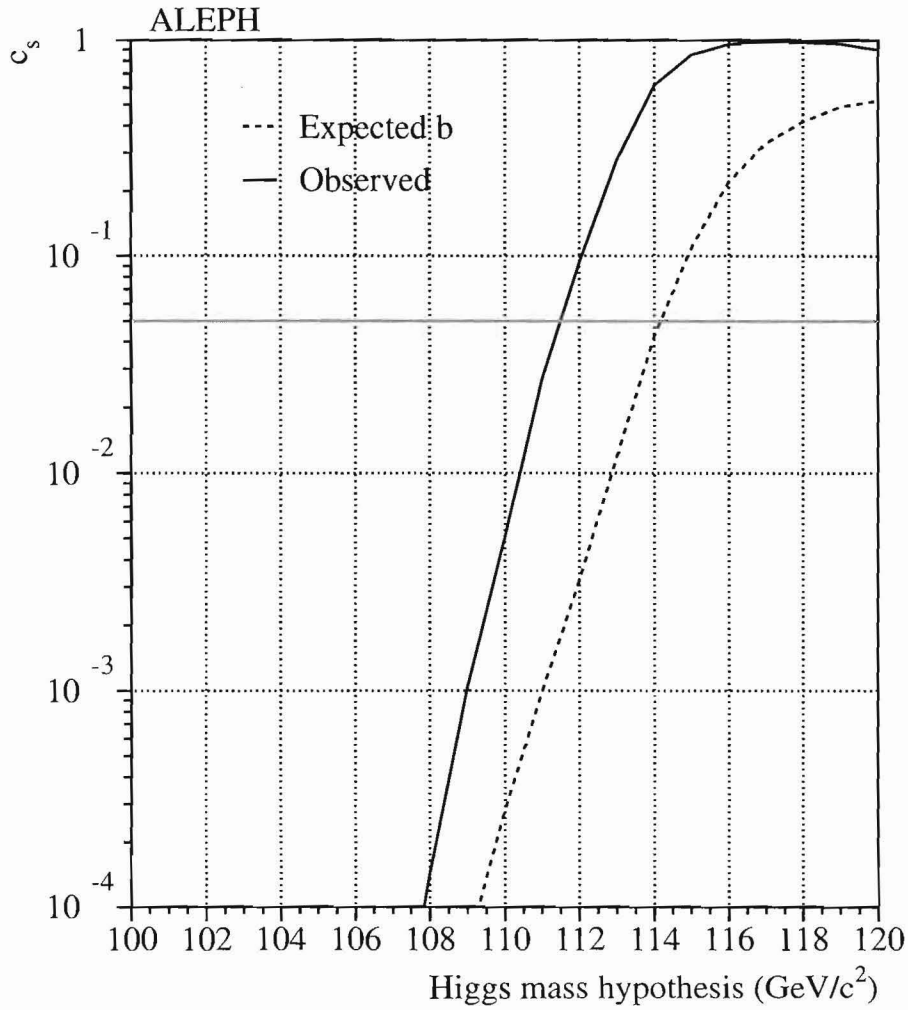

Figure 7.9: Signal hypothesis exclusion, computed with the signal estimator method, from combined ALEPH results for different Higgs boson mass hypotheses. The observed and expected confidence integrals are plotted as solid and dashed lines, respectively.

Channel	Limits (GeV/c^2)	
	Expected	Observed
$\mathrm{Hq\bar{q}}$	113.2	108.8
$\mathrm{H}\nu\bar{\nu}$	109.6	111.6
$\mathrm{H}\ell^+\ell^-$	105.6	107.1
$\mathrm{H}\tau^+\tau^-$, $\tau^+\tau^-\mathrm{q\bar{q}}$	99.8	102.7
Combined	114.2	111.5

Table 7.1: Higgs boson mass 95% confidence level exclusion limits for individual searches and for combined searches.

7.6 Effects of Statistical and Systematic Uncertainties

The confidence exclusion results presented in this chapter include the effects of systematic uncertainties, calculated using the prescription advocated by Cousins and Highland [75]. This approach calculates the convolution of a Gaussian uncertainty function with the expected number of signal and background events before constructing the experiment test statistic probability density function. Under such treatment, the effect of the systematic uncertainties on the combined ALEPH exclusion limit is less than 100 MeV/c^2.

An indicative, but non-rigorous, parallel approach seeks to calculate the effect of systematic uncertainties on the observed significance for $m_{\mathrm{H}} = 116\,\mathrm{GeV}/c^2$. As a result, this study of uncertainties focuses on search channels which select one or more high-weight candidates with reconstructed Higgs boson masses between 114 and 118 GeV/c^2. For each source of uncertainty, the expected number of signal and background events in this interval are recalculated using the high and low excursions about the nominal value. The confidence integral c_b is then reevaluated at $m_{\mathrm{H}} = 116\,\mathrm{GeV}/c^2$ for the two excursions, and the effect of the uncertainty is defined as half the differ-

ence between the new significances. The list of known systematic uncertainties and their effects on the observed significance is summarized in Table 7.2.

Systematic Uncertainty	Effect (σ)
$\mathrm{Hq\bar{q}}$ 2b MC statistics	± 0.068
$\mathrm{Hq\bar{q}}$ 4b MC statistics	± 0.025
$\mathrm{H}\ell^+\ell^-$ MC statistics	± 0.024
$\mathrm{H}\tau^+\tau^-$ MC statistics	± 0.015
b tagging ($\mathrm{b\bar{b}}$)	± 0.024
b tagging (udsc)	± 0.077
jet energy & angle	± 0.054
gluon splitting	± 0.042
α_s value	± 0.056
other $\mathrm{Hq\bar{q}}$	± 0.052
other $\mathrm{H}\ell^+\ell^-$	± 0.026

Table 7.2: Effects of selected systematic uncertainties on the observed significance. The effect from each source is obtained by calculating a new expected number of events in a mass window centered at $m_{\mathrm{H}} = 116\,\mathrm{GeV}/c^2$ and using that number to reevaluate the confidence integral c_b.

Each channel has its own uncertainties on the expected number of events due to limited statistics within the defined mass window in the simulated dataset. Uncertainties on b tagging distributions for b quarks and for light quarks are estimated by reweighting the tagging neural network output in simulation to match the output in data. Measured jet energies and jet angles in simulation are smeared by an amount equal to the ALEPH energy flow parametrization error [30]. The gluon splitting rate and α_s are varied within the reported errors around the measured values. Uncertainty in other $\mathrm{Hq\bar{q}}$ 2b and $\mathrm{H}\ell^+\ell^-$ selection variables are also included. (The $\mathrm{Hq\bar{q}}$ 4b and $\mathrm{H}\tau^+\tau^-$ selection variables are correlated, if not identical, to the b tagging output and jet measurement already mentioned.)

Although these numbers give some indication of the relative sensitivity of the observed excess to various uncertainties, the sum in quadrature is an overestimate of

the effect of the systematic uncertainties. The Cousins-Highland method remains the most rigorous approach to calculating the effect of uncertainties when computing the confidence integral and derived results.

Chapter 8

Summary and Outlook

The observation of an excess in the ALEPH search for the Higgs boson contributes to an excess for the combined LEP search and has interesting implications for future Higgs boson searches.

8.1 Combined Results of Higgs Searches at LEP

Each of the four collaborations at LEP searches for the Higgs boson in multiple final states. The combination of the independent results is mathematically trivial when the likelihood ratio is used as a test-statistic. Although the final LEP results have not yet been combined, a preliminary combination completed in November 2000 used 96% of the collected data [76]. The combined negative log-likelihood ratio curve and its accompanying background compatibility curve from that time are shown in Fig. 8.1. The minimum of the negative log-likelihood ratio distribution occurs for a Higgs boson mass hypothesis of $115\,\mathrm{GeV}/c^2$, and the value of the observed minimum matches the value expected from Higgs boson production at that mass. The compatibility $(1 - c_b)$ of the observed data with the background-only hypothesis at $115\,\mathrm{GeV}/c^2$ is 0.4%,

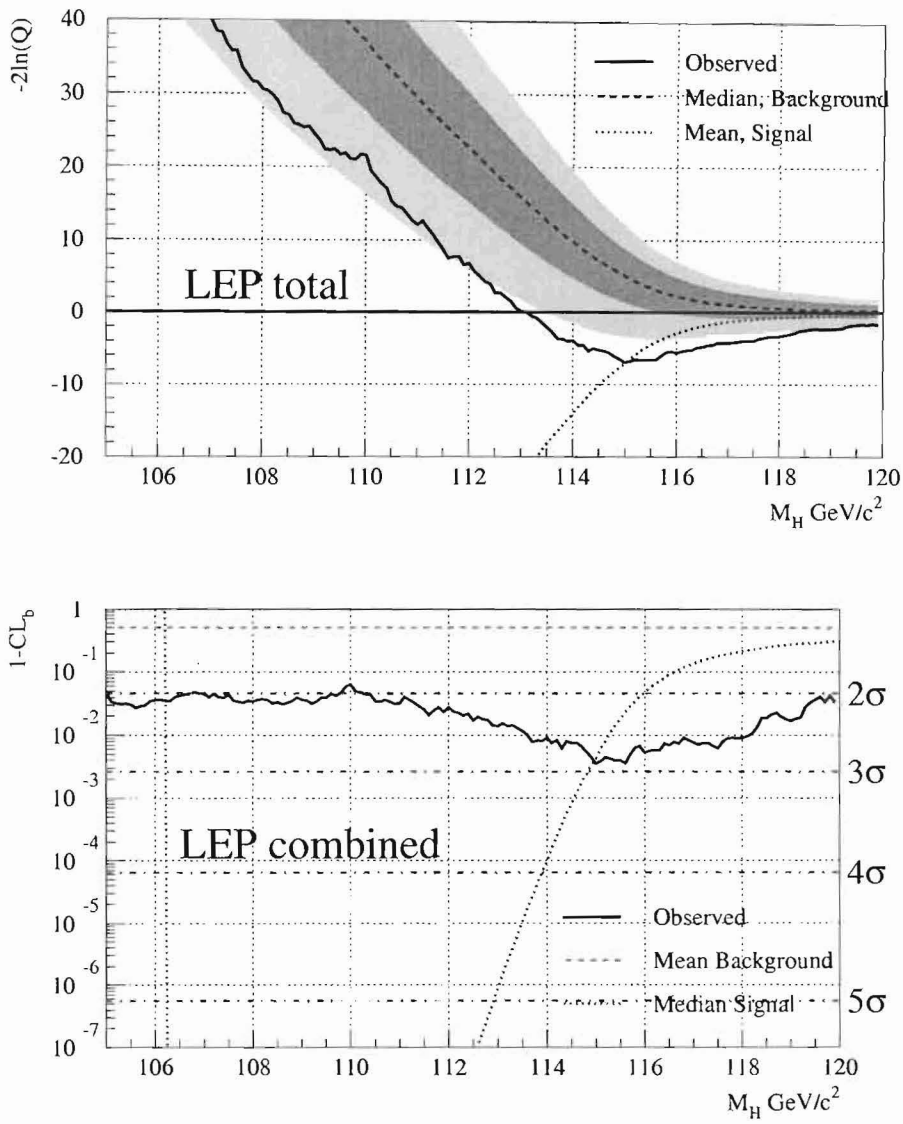

Figure 8.1: Preliminary results from combined LEP Higgs boson searches. At top, the negative log-likelihood ratio as a function of the Higgs boson mass hypothesis. The shaded 68% and 95% compatibility bands flank the expectation from the background-only hypothesis, and the dashed line is the expectation when signal is added. At bottom, the confidence in the background-only hypothesis as a function of the Higgs boson mass hypothesis. The dashed lines indicate Gaussian equivalents for excesses above the expected background rate. The result from the observed dataset is the thick solid line [77].

which corresponds to a 2.9σ Gaussian equivalent excess above the background rate. Using the alternative c_s prescription outlined in Ref. [66], Higgs boson masses below $113.5\,\mathrm{GeV}/c^2$ are excluded at 95% confidence level with the LEP combined data, while the median expected limit in the absence of signal is $115.3\,\mathrm{GeV}/c^2$.

8.2 Future Higgs Boson Searches

Higgs boson search results in the near future will come from experiments at two high energy hadron colliders, the Tevatron and the LHC.

8.2.1 Higgs Boson Searches at the Tevatron

The upgraded Tevatron at Fermi National Accelerator Laboratory has begun colliding 1 TeV proton and antiproton beams inside the CDF and DØ detectors. The planned increase in luminosity with respect to Run I will give the Tevatron the potential to discover a light Higgs boson in Run II.

Although the dominant Higgs production mechanism at the Tevatron is gluon fusion, hadronic jet production overwhelms the simple $\mathrm{gg} \to \mathrm{H} \to \mathrm{b\bar{b}}$ signal channel. For a Higgs boson with a mass less than $130\,\mathrm{GeV}/c^2$, the $\mathrm{p\bar{p}} \to \mathrm{HW}$ and $\mathrm{p\bar{p}} \to \mathrm{HZ}$ production channels appear to be most promising because the combination of leptons and missing E_T make background rejection easier in the $\ell^+\ell^-\mathrm{b\bar{b}}$, $\ell^-\bar{\nu}\mathrm{b\bar{b}}$, and $\nu\bar{\nu}\mathrm{b\bar{b}}$ final states. A recent study indicates that $\mathrm{t\bar{t}H} \to \mathrm{W^+\bar{b}W^-b\bar{b}}$ may also be observable when one W decays leptonically [78].

A Higgs boson with mass between 130 and $180\,\mathrm{GeV}/c^2$ decays predominantly to $\mathrm{W^+W^-}$. As a result, the most sensitive channel is $\mathrm{gg} \to \mathrm{H} \to \mathrm{WW^*}$; the corresponding final states $\ell^-\bar{\nu}\ell^+\nu$ and $\ell^+\ell^-\mathrm{q\bar{q}}$ are easily distinguished from the jet background by their leptons.

The current Tevatron schedule calls for an integrated luminosity of $2\,\mathrm{fb}^{-1}$ per detector by 2003 and $15\,\mathrm{fb}^{-1}$ per detector by 2007. Figure 8.2 shows the expected sensitivity of the combined CDF and DØ searches to standard model Higgs boson production. With $2\,\mathrm{fb}^{-1}$, the Tevatron experiments will have the possibility to ex-

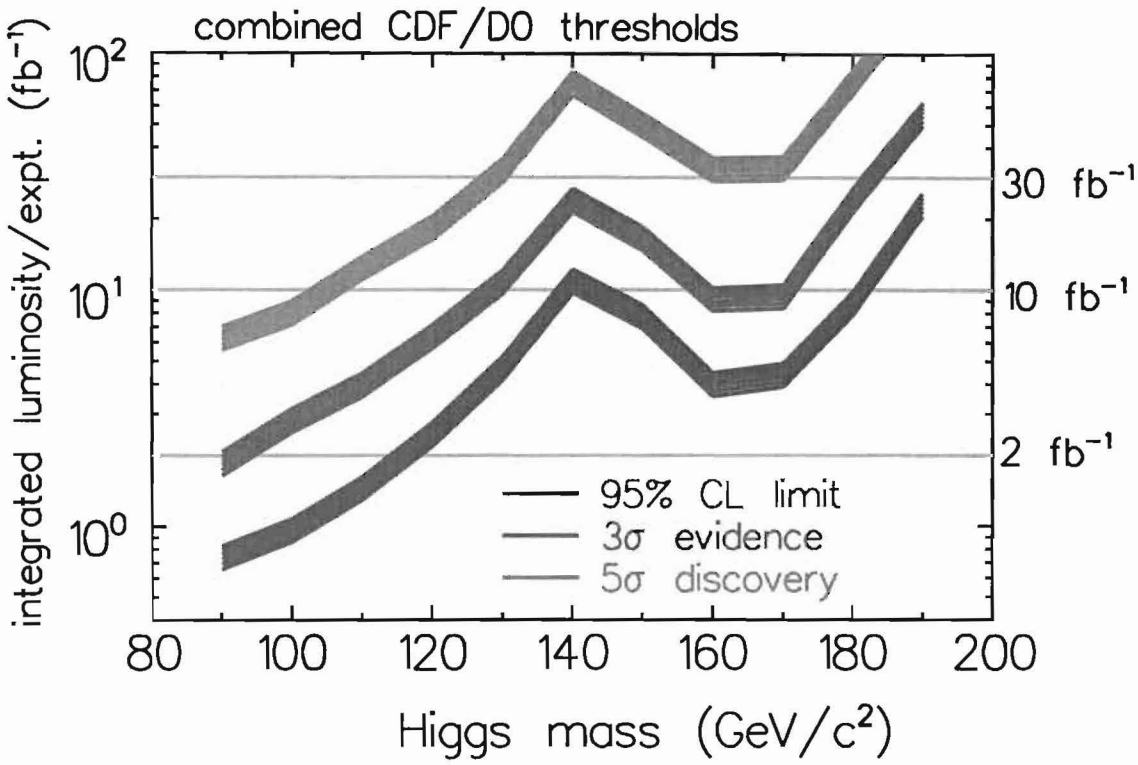

Figure 8.2: Integrated luminosity per experiment required to exclude at 95% confidence level or discover at 3σ or 5σ a Higgs boson with a given mass [79]. These results represent the combined statistical power of the CDF and DØ Higgs searches.

clude, at 95% confidence level, Higgs boson masses up to $115\,\mathrm{GeV}/c^2$; with $15\,\mathrm{fb}^{-1}$, Higgs bosons in the same mass range can be discovered with 5σ significance, or all masses up to $180\,\mathrm{GeV}/c^2$ can be excluded [79]. If the Higgs boson mass is in fact above this range, then a Higgs boson discovery is still possible at the LHC.

8.2.2 Higgs Boson Searches at the LHC

The Large Hadron Collider (LHC) at CERN will be a proton-proton collider with a center-of-mass energy of 14 TeV. The high planned LHC luminosities of 10^{33} to $10^{34}\,\mathrm{cm}^{-2}\mathrm{s}^{-1}$, although experimentally challenging for the ATLAS and CMS detectors, will make possible a Higgs boson discovery with only one full year of data [80, 81]. The copious number of Higgs bosons produced will make the LHC well-suited to further studies of the Higgs boson's properties.

The chief advantage of the LHC luminosity is that even rare signal processes contribute a significant number of events. For a Higgs boson with mass less than $130\,\mathrm{GeV}/c^2$, the clean signature of $\mathrm{H} \to \gamma\gamma$ is one possible discovery channel, whether the Higgs boson itself is produced via gluon fusion or vector boson fusion. At very low masses, the search for H production proceeds much like the one at the Tevatron.

For $m_{\mathrm{H}} > 130\,\mathrm{GeV}/c^2$, the channel $\mathrm{gg} \to \mathrm{H} \to \mathrm{ZZ}^* \to \ell^+\ell^-\ell^+\ell^-$ features a final state with very low background contribution. Most of the LHC discovery potential comes from this "gold-plated" channel. The signal of Higgs boson production with a mass near $2m_{\mathrm{Z}}$ would be eclipsed by the ZZ continuum background, so the $\mathrm{H} \to \mathrm{WW}^* \to \ell^+\nu\ell^-\bar{\nu}$ channel is used to supplement the search for masses between 150 and $190\,\mathrm{GeV}/c^2$.

The LHC schedule calls for first beams in 2006 and a physics run with $10\,\mathrm{fb}^{-1}$ delivered luminosity in 2007. Figure 8.3 shows the expected discovery significance for ATLAS and CMS combined. Ironically, the LHC experiments are least sensitive to Higgs boson production at masses near $115\,\mathrm{GeV}/c^2$. Nevertheless, an integrated luminosity of $10\,\mathrm{fb}^{-1}$ per experiment will suffice for a 5σ discovery at any Higgs boson mass between $115\,\mathrm{GeV}/c^2$ and $1\,\mathrm{TeV}/c^2$.

If the standard model Higgs boson is not produced at LHC with mass less than

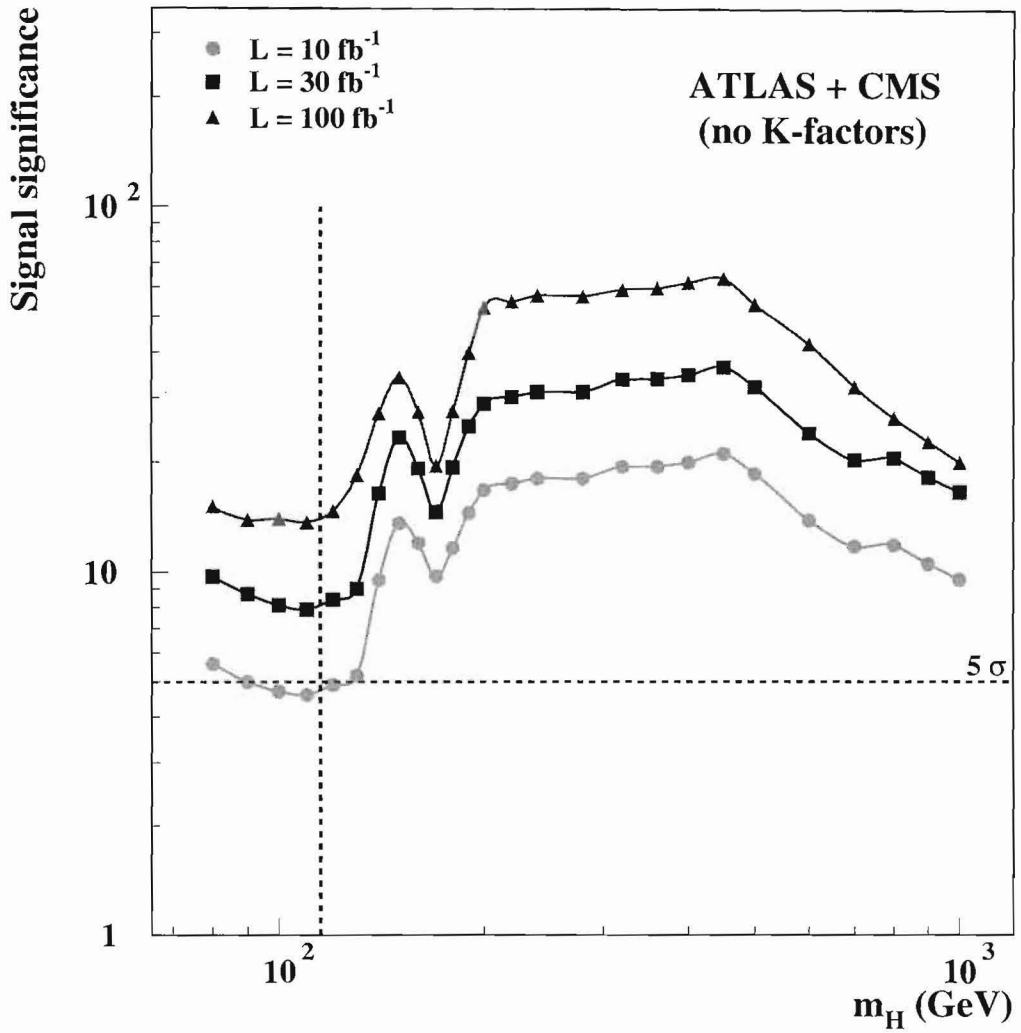

Figure 8.3: LHC combined discovery significance as a function of the Higgs boson mass for various integrated luminosities per experiment [82].

$1\,\mathrm{TeV}/c^2$, then a new theory of electroweak symmetry breaking, different from the Higgs mechanism, may be required.

8.3 Conclusion

Although the results using data from the ALEPH detector are tantalizingly consistent with expectations from a Higgs boson of mass $115\,\mathrm{GeV}/c^2$, the small expected number of signal events, even from the four LEP experiments combined, makes it impossible to claim unambiguous evidence for the Higgs boson.

The exploration of electroweak symmetry breaking, particularly the search for the Higgs boson, remains a primary objective of the worldwide high energy physics program for the next decade. More data from experiments at the Tevatron and the LHC will be needed to determine whether this observation of an excess is the result of a statistical fluctuation or the first sign of direct production of the standard model Higgs boson.

Appendix A

Confidence Level Calculations using the Fourier Transform

When the likelihood ratio is used as a test statistic, the experiment test statistic distribution may be calculated analytically with the Fourier transform. The most dramatic advantage of the analytic method over the toy Monte Carlo method is the increase in calculation speed.

A.1 Ensemble Test Statistic Distributions via Fourier Transform

One way to form an test statistic for an ensemble of events is to generate a large number of toy Monte Carlo experiments, each experiment having a number of events generated from a Poisson distribution. Another way is to compute analytically the probability density function of the ensemble test statistic given the probability density function of the event test statistic. The discussion of this section pursues the latter approach.

The likelihood ratio test statistic is a multiplicative test statistic; the test statistic for an ensemble of events is formed by multiplying the individual event test statistics. Alternatively, the logarithms of the test statistics may be summed. In the following derivation, $F = \ln E$, where E is the likelihood ratio test statistic

$$E = C\frac{\mathcal{L}_{s+b}}{\mathcal{L}_b}.$$

Because the constant factor C is present in the test statistic for every event, it does not affect the power of the likelihood ratio test, which is used to order events from signal-like to background-like. In this construction, C is chosen to be e^s, where s is the expected number of signal events, for the sake of clarity.

For an experiment with 0 events observed, the test statistic is trivial:

$$\begin{aligned} E &= e^s \frac{e^{-(s+b)}}{e^{-b}} = 1 \\ F &= 0 \\ \rho_0(F) &= \delta(F), \end{aligned}$$

where b is the expected number of background events. The function $\rho_0(F)$ is the probability density function in F for experiments with 0 observed events.

For an experiment with exactly one event, the test statistic is, using the reconstructed Higgs mass m as a single discriminant variable,

$$\begin{aligned} E &= e^s \frac{e^{-(s+b)}\left[sf_s(m) + bf_b(m)\right]}{e^{-b}\left[bf_b(m)\right]} \\ F &= \ln \frac{sf_s(m) + bf_b(m)}{bf_b(m)}, \end{aligned}$$

and the probability density function in F is defined as $\rho_1(F)$.

For an experiment with exactly two events, the test statistics of the two events are multiplied to form the ensemble test statistic. (For simplicity, it is assumed in this derivation that there is only one type of signal process and one type of background process.) If the reconstructed Higgs masses of the two events are m_1 and m_2, then

$$\begin{aligned} E &= \frac{[sf_s(m_1) + bf_b(m_1)]\,[sf_s(m_2) + bf_b(m_2)]}{[bf_b(m_1)]\,[bf_b(m_2)]} \\ F &= \ln \frac{sf_s(m_1) + bf_b(m_1)}{bf_b(m_1)} + \ln \frac{sf_s(m_2) + bf_b(m_2)}{bf_b(m_2)}. \end{aligned}$$

The probability density function for exactly two particles $\rho_2(F)$ is simply the convolution of $\rho_1(F)$ with itself:

$$\begin{aligned} \rho_2(F) &= \iint \rho_1(F_1)\rho_1(F_2)\delta(F - F_1 - F_2)dF_1 dF_2 \\ &= \rho_1(F) \otimes \rho_1(F). \end{aligned}$$

The generalization to the case of n events is straightforward and encouraging:

$$\begin{aligned} E &= \prod_{i=1}^{n} \frac{sf_s(m_i) + bf_b(m_i)}{bf_b(m_i)} \\ F &= \sum_{i=1}^{n} \ln \frac{sf_s(m_i) + bf_b(m_i)}{bf_b(m_i)} \\ \rho_n(F) &= \int \cdots \int \prod_{i=1}^{n} [\rho_1(F_i)dF_i]\,\delta\left(F - \sum_{i=1}^{n} F_i\right) \\ &= \underbrace{\rho_1(F) \otimes \cdots \otimes \rho_1(F)}_{n \text{ times}}. \end{aligned}$$

Next, the convolution of $\rho_1(F)$ is rendered manageable by an application of the relationship between the convolution and the Fourier transform. If $A(F) = B(F) \otimes C(F)$, then the Fourier transforms of A, B, and C satisfy $\overline{A(G)} = \overline{B(G)} \cdot \overline{C(G)}$. This

allows the convolution to be expressed as a simple power

$$\overline{\rho_n(G)} = \left[\overline{\rho_1(G)}\right]^n .$$

Note this equation holds even for $n = 0$, since $\overline{\rho_0(G)} = 1$. For any practical computation, the analytic Fourier transform may be approximated by a numerical Fast Fourier Transform (FFT).

The above relation can be used to determine $\rho_{s+b}(F)$ and $\rho_b(F)$, the expected distributions for ensembles of signal+background events and of background-only events. The probability density function for an experiment test statistic with s expected signal and b expected background events is

$$\rho_{s+b}(F) = \sum_{n=0}^{\infty} e^{-(s+b)} \frac{(s+b)^n}{n!} \rho_n(F),$$

where n is the number of events observed. Upon Fourier transformation, this becomes

$$\begin{aligned}
\overline{\rho_{s+b}(G)} &= \sum_{n=0}^{\infty} e^{-(s+b)} \frac{(s+b)^n}{n!} \overline{\rho_n(G)} \\
&= \sum_{n=0}^{\infty} e^{-(s+b)} \frac{(s+b)^n}{n!} \left[\overline{\rho_1(G)}\right]^n \\
&= e^{-(s+b)} \sum_{n=0}^{\infty} \frac{\left[(s+b)\overline{\rho_1(G)}\right]^n}{n!} \\
\overline{\rho_{s+b}(G)} &= e^{(s+b)\left[\overline{\rho_1(G)}-1\right]}
\end{aligned}$$

The function $\rho_{s+b}(F)$ may then be recovered by using the inverse transform. In general, this relation, which holds for any multiplicative test statistic, means that the probability density function for an arbitrary number of expected signal and background events may be calculated analytically once the probability density function of

the test statistic is known for a single event.

Two examples provide practical proof of the principle. For the first, assume a hypothetical test statistic results in an event test statistic probability density function of simple Gaussian form

$$\rho_1(F) = \frac{1}{\sigma\sqrt{2\pi}} e^{-\frac{(F-\mu)^2}{2\sigma^2}},$$

where $\sigma = 0.2$ and $\mu = 2.0$. With $s + b = 20.0$, both the FFT method and the toy Monte Carlo method are used to evolve the event test statistic probability density function to an experiment test statistic probability density function. The agreement between the two methods (Fig. A.1) is striking, but the higher precision of the FFT method is apparent, even when compared to 1 million toy Monte Carlo experiments. The periodic structure is due to the discrete Poisson distribution being convolved with a relatively narrow event test statistic probability function. In particular, the peak at $\ln E = 0$ corresponds to the probability that exactly zero events be observed ($e^{-(s+b)} = 2.1 \times 10^{-9}$). The precision of the toy Monte Carlo method is limited by the number of Monte Carlo experiments, while the precision of the FFT method is limited only by the precision of the numerical integration.

For the second example, the probability density function of a typical non-Gaussian test statistic is calculated for an experiment with $s = 5$ and $b = 3$ expected events (Fig. A.2). Again, the two methods agree well in regions where the toy Monte Carlo method is useful.

A.2 Combination of Search Channels

Consider one channel having k types of signal events and l types of background events. The number of each type of event is denoted by u_i, $(i = 1, 2, \ldots, k + l)$. Then the

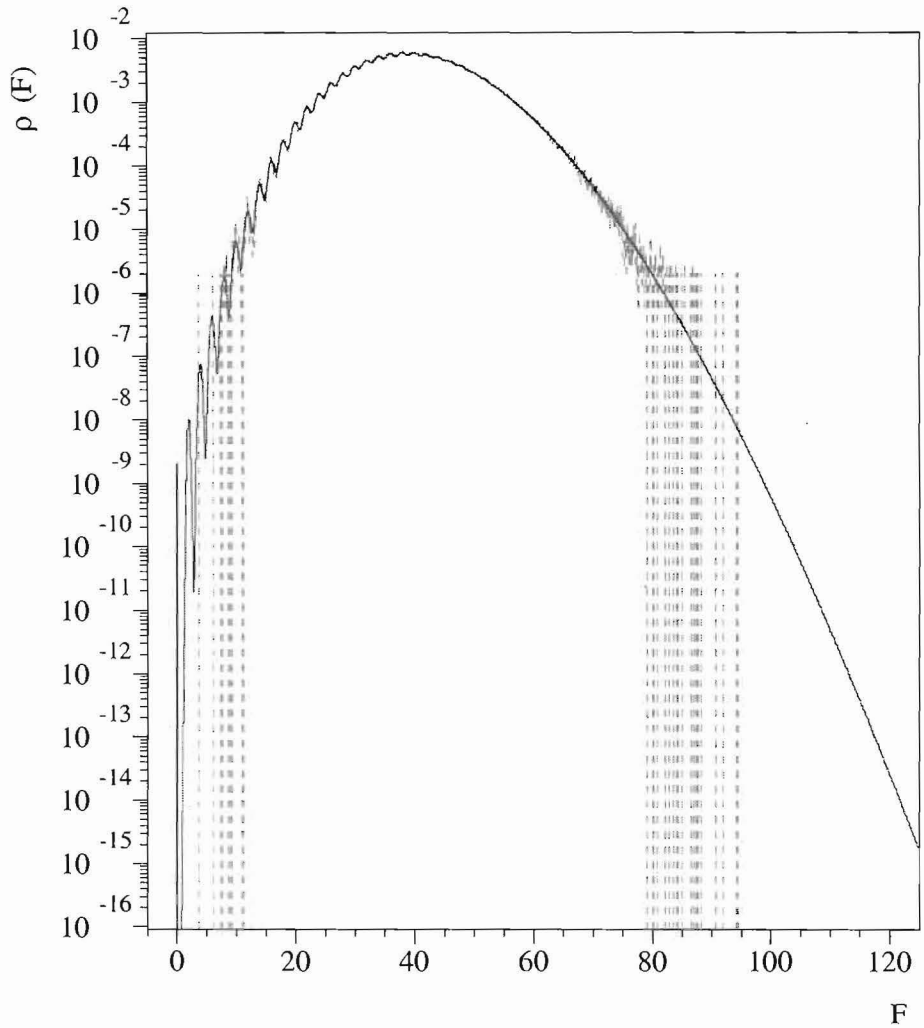

Figure A.1: The experiment test statistic probability density function for a Gaussian-distributed event test statistic distribution. The solid line is calculated with the FFT method, and the dashed line is calculated with the toy Monte Carlo method. Error bars associated with the Monte Carlo method are due to limited Monte Carlo statistics.

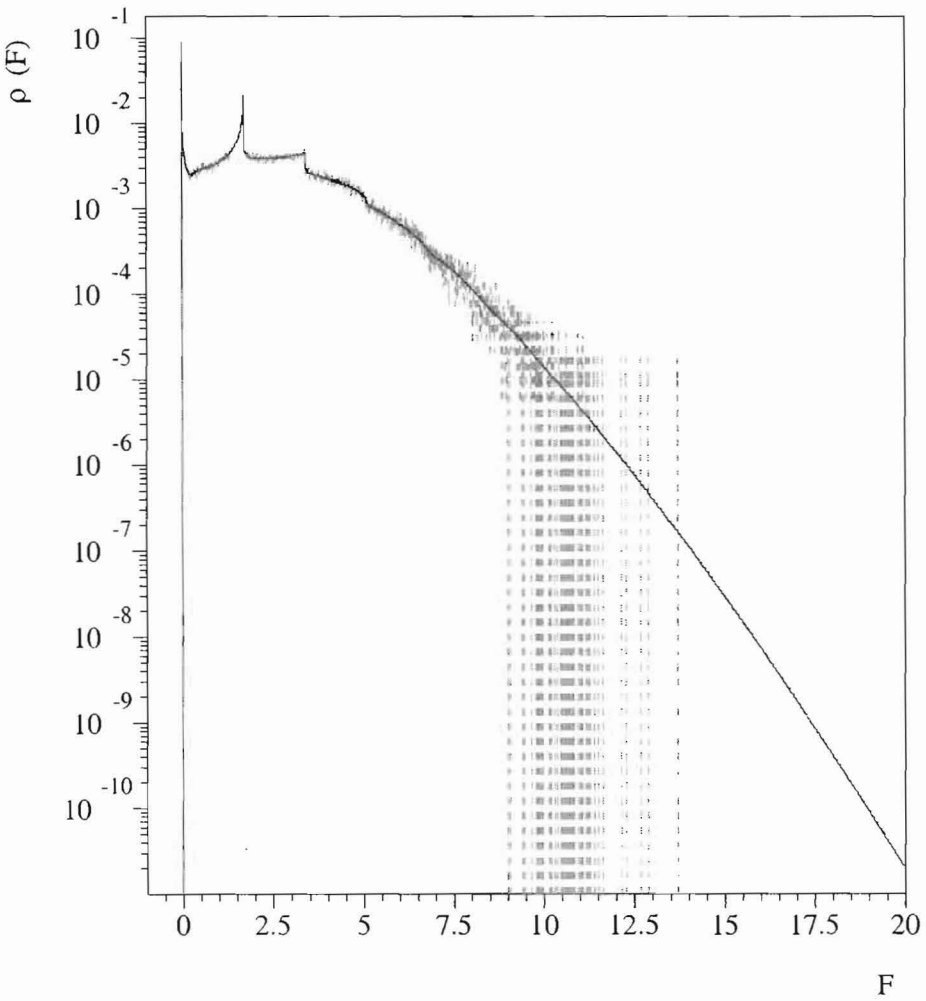

Figure A.2: The experiment test statistic probability density function for a typical non-Gaussian event test statistic distribution. The solid line is calculated with the FFT method, and the dashed line is calculated with the toy Monte Carlo method.

Fourier transform of the experiment test statistic's density function is calculated using the previous results:

$$\overline{\rho(G)} = e^{\sum_{i=1}^{k+l} u_i \left[\overline{\rho_{1,i}(G)} - 1\right]}$$

where $\overline{\rho_{1,i}(G)}$ is the transformed density function for one event of the ith type. The combination of all search channels uses the same method, with each channel described as a set of signal and background types.

Due to the strictly multiplicative nature of the test statistic, this combination method is internally consistent. No matter how subsets of the combinations are rearranged (*i.e.*, combining channels in different orders, combining different subsets of data runs), the result of the combination does not change.

A.3 Discussion on Systematic Uncertainties

When the likelihood ratio is used as a test statistic, the systematic uncertainty on the confidence level is due to the uncertainties on numbers of signal and background events expected and the distributions of the discriminant variables. Since the distributions are nothing more than the density of signal and background events in the discriminant variable space, we focus only on the uncertainty due to uncertainties on background and signal numbers.

If the uncertainties follow a Gaussian distribution with a correlated error matrix

$$S_{ij} = \langle (u_i - \langle u_i \rangle)(u_j - \langle u_j \rangle) \rangle$$

between the $k + l$ types of events, then the uncertainty on the experiment test statis-

tic's density function may be calculated analytically as

$$\overline{\rho_{\text{sys}}(G)} = e^{\sum_{i=1}^{k+l}\langle u_i\rangle\left[\overline{\rho_{1,i}(G)}-1\right]+\frac{1}{2}\sum_{i,j}\left[\overline{\rho_{1,i}(G)}-1\right]S_{ij}\left[\overline{\rho_{1,j}(G)}-1\right]}.$$

In general, if the resolution function can be constructed by combining several Gaussian distributions, the systematic uncertainty on the likelihood ratio distribution can be calculated analytically.

A.4 Summary

The analytic confidence level calculation with a multiplicative test statistic makes possible studies that might have otherwise been too CPU-intensive with the toy MC method. These include studies of improvements in the event selections, of various working points, and of effects from systematic errors. A precise calculation also makes possible rejection of null hypotheses at the level necessary for discovery.

Bibliography

[1] D.E. Groom *et al.* (Particle Data Group), Euro. Phys. J **C15** (2000) 1.

[2] S. Glashow, Nucl. Phys. **22** (1961) 579;

A. Salam, in *Elementary Particle Theory*, ed. N. Svartholm, (Almqvist and Wiksells, Stockholm, 1968);

S. Weinberg, Phys. Rev. Lett. **19** (1967) 1264.

[3] V.D. Barger and R.J.N. Phillips, *Collider Physics*, (Addison-Wesley, Redwood City, CA, 1987).

[4] P.W. Higgs, Phys. Lett. **12** (1964) 132; Phys. Rev. Lett. **13** (1964) 508; Phys. Rev. **145** (1966) 1156;

F. Englert and R. Brout, Phys. Rev. Lett. **13** (1964) 321;

G.S. Guralnik, C.R. Hagen, and T.W.B. Kibble, Phys. Rev. Lett. **13** (1964) 585.

[5] C. Quigg, *Gauge Theories of the Strong, Weak, and Electromagnetic Interactions*, (Benjamin/Cummings, Menlo Park, 1983).

[6] J. Goldstone, Nuovo Cimento **19** (1961) 154.

[7] N. Cabbibo, Phys. Rev. Lett. **10** (1963) 531.

[8] M. Kobayashi and T. Maskawa, Prog. Theor. Phys. **49** (1973) 652.

[9] B.W. Lee, C. Quigg, and H.B. Thacker, Phys. Rev. **D16** (1977) 1519.

[10] R. Jacobsen, "Top Mass from Electroweak Measurements," presented at the XXIX Rencontres de Moriond, "QCD and Hadronic Interactions," Meribel, France, March 9-26, 1994; CERN-PPE/94-97.

[11] M. Veltman, Acta Phys. Polon. **B8** (1977) 475.

[12] E. Tournefier for the LEP Electroweak Working Group, "Electroweak fits and the Higgs likelihood," presented at the XXXVIme Rencontres de Moriond, Moriond, France, March 11-17, 2001.

[13] B. Pietrzyk, "The global fit to electroweak data," presented at International Conference of High Energy Physics (ICHEP2000), Osaka, Japan, July 27 - August 2, 2000; LAP-EXP-00.06.

[14] ALEPH, DELPHI, L3, and OPAL Collaborations (LEP working group for Higgs boson searches), "Search for Higgs bosons: Preliminary combined results using LEP data collected at energies up to 202 GeV," CERN-EP/2000-055 (2000, unpublished).

[15] J. Guimaraes da Costa for the CDF Collaboration, "Standard Model Higgs Combined Results from CDF," presented at the Meeting of the Division of Particles and Fields (DPF 2000) of the American Physical Society, Columbus, OH, August 9-12, 2000.

[16] F. Abe *et al.* (CDF Collaboration), Phys. Rev. Lett. **81** (1998) 5748.

[17] J. Ellis, M.K. Gaillard, and D.V. Nanopoulos, Nucl. Phys. **B106** (1976) 292;

B.L. Ioffe and V.A. Khoze, Sov. J. Part. Nucl. **9** (1978) 50;

J.D. Bjorken, "Weak Interaction Theory and Neutral Currents," in *Proceedings of the 1976 SLAC Summer Inst. on Particle Physics*, ed. M. Zipf, SLAC report 198 (1977) 1.

[18] W. Kilian, M. Kramer, and P.M. Zerwas, Phys. Lett. **B373** (1996) 135; "Higgsstrahlung and vector boson fusion in e^+e^- collisions," hep-ph/9605437 (1996).

[19] P. Janot, "The HZHA Generator" in *Physics at LEP2*, eds. G. Altarelli, T. Sjöstrand, and F. Zwirner, CERN Yellow Report 96-01 (1996), Vol. 2, p. 309. For HZHA03, see http://alephwww.cern.ch/~janot/Generators.html.

[20] E. Gross, B.A. Kniehl, and G. Wolf, Z. Phys. **C63** (1994) 417; Erratum *ibid.* **C66** (1995) 321.

[21] A. Blondel *et al.* (LEP Energy Working Group), Eur. Phys. J. **C11** (1999) 573.

[22] L. Arnaudon *et al.* (LEP Energy Working Group), Z. Phys. **C66** (1995) 45.

[23] The LEP Energy Working Group, "Evaluation of the LEP centre-of-mass energy for data taken in 2000," LEP Energy Working Group report 01/01 (2001, unpublished).

[24] "TESLA Technical Design Report," eds. F. Richard *et al.*, DESY 2001-011, ECFA 2001-209 (2001).

[25] NLC Collaboration, "2001 Report on the Next Linear Collider," ed. N. Phinney, FERMILAB-CONF-01/075-E, LBNL-PUB-47935, SLAC-R-571, UCRL-ID-144077 (2001).

[26] C.M. Ankenbrandt *et al.*, "Status of Muon Collider Research and Development and Future Plans," BNL-65623, FERMILAB-PUB-98/179, LBNL-41935 (1998).

[27] D. Creanza *et al.*, Nucl. Instrum. Methods **A409** (1998) 157.

[28] The ALEPH Handbook, Vol. 2, ed. C. Bowdery, (CERN, Geneva, 1997).

[29] The ALEPH Handbook, Vol. 1, ed. C. Bowdery, (CERN, Geneva, 1995).

[30] D. Buskulic *et al.* (ALEPH Collaboration), Nucl. Instrum. Methods **A360** (1995) 481.

[31] W.R. Leo, *Techniques for nuclear and particle physics experiments: A how-to approach*, (Springer, Berlin, 1994).

[32] S. Jadach *et al.*, "Event Generators for Bhabha Scattering" in *Physics at LEP2*, eds. G. Altarelli, T. Sjöstrand, and F. Zwirner, CERN Yellow Report 96-01 (1996), Vol. 2, p. 229.

[33] J. Knobloch and E. Lançon, "Julia User's Guide and ALEPH Programmer's Hints," ALEPH internal report ALEPH 94-151 (1994, unpublished).

[34] R. Frühwirth, Nucl. Instrum. Methods **A262** (1987) 444.

[35] S. Jadach, B.F.L. Ward, and Z. Wąs, Comp. Phys. Commun. **79** (1994) 503.

[36] D. Bardin *et al.*, in *Physics at LEP200 and Beyond*, eds. J. Blümlein and T. Riemann (North-Holland, Amsterdam, 1994), p. 148.

[37] M. Skrzypek, S. Jadach, W. Płaczek, and Z. Wąs, Comput. Phys. Commun. **94** (1996) 216.

[38] T. Sjöstrand, Comput. Phys. Commun. **82** (1994) 74;
T. Sjöstrand, *The PYTHIA 5.7 and JETSET 7.4 Manual*, LU TP 95-20 and CERN TH 7112-93 (unpublished).

[39] Based on cross section calculations presented in S. Ambrosiano and B. Mele, Nucl. Phys. **B374** (1992) 3.

[40] R. Brun *et al.*, CERN-DD/78-2 (1978, unpublished);
R. Brun *et al.*, CERN-DD/EE/84-1 (1984, unpublished);
`http://wwwinfo.cern.ch/asd/geant/`

[41] D. Buskulic *et al.* (ALEPH Collaboration), Nucl. Instrum. Methods **A346** (1994) 461.

[42] S.R. Armstrong, Ph.D. dissertation, University of Wisconsin-Madison (1998).

[43] S.R. Armstrong, presentation to the ALEPH Higgs Task Force on Jan. 21, 1999 (unpublished).

[44] D. Buskulic *et al.* (ALEPH Collaboration), Phys. Lett. **B313** (1993) 535.

[45] D. Buskulic *et al.* (ALEPH Collaboration), Phys. Lett. **B322** (1994) 441.

[46] L. Bellantoni *et al.*, Nucl. Instrum. Methods **A310** (1991) 618.

[47] C. Peterson, T. Rögnvaldsson, and L. Lönnblad, Comput. Phys. Commun. **81** (1994) 185.

[48] W.J. Stirling *et al.*, J. Phys. G: Nucl. Part. Phys. **17** (1991) 1567;
S. Catani *et al.*, Phys. Lett. **B269** (1991) 432.

[49] A. Tilquin, "Constrained fit and Initial State Radiation in Four Jet Events at LEPII," ALEPH internal report ALEPH 95-129 (1995, unpublished).

[50] B. Tuchming, presentation to the ALEPH Higgs Task Force, Sept. 30, 1999 (unpublished).

[51] B. Tuchming, "A four-variable neural network for b-tagging. Application to the search for $hA \to b\bar{b}b\bar{b}$ at $\sqrt{s} = 189\,\mathrm{GeV}$," ALEPH internal report ALEPH 99-040 (1999, unpublished).

[52] B. Fabbro, "Linear discriminant analysis with stepwise method. Application for MSSM Higgs boson search in the $hA \to b\bar{b}$ channel at LEP2," ALEPH internal report ALEPH 97-012 (1997, unpublished).

[53] A. Zell *et al.*, *"SNNS - Stuttgart Neural Network Simulator User Manual, Version 4.0"*, University of Stuttgart, Institute for Parallel and Distributed High Performance Computing (IPVR), Department of Computer Science, Report 6/95 (1995).

[54] R. Barate *et al.* (ALEPH Collaboration), Euro. Phys. J **C17** (2000) 223.

[55] H. Drevermann, D. Kuhn, and B.S. Nilsson, "Event Display: Can We See What We Want To See?," CERN/ECP 95-25 (1995, unpublished).
See also `http://alephwww.cern.ch/DALI/` .

[56] S. Armstrong *et al.*, "Studies of Higgs candidates with masses around $114\,\mathrm{GeV}/c^2$ in four-jet events at $\sqrt{s} > 205\,\mathrm{GeV}$ using neural network techniques," ALEPH internal report ALEPH 2000-079 (2000, unpublished).

[57] J. Kennedy, presentation to the ALEPH Higgs Task Force on Apr. 4, 2001 (unpublished).

[58] R. Barate *et al.* (ALEPH Collaboration), Phys. Lett. **B495** (2000) 1.

[59] O. Buchmuller, "$e^+e^- \to HZ \to b\bar{b}q\bar{q}$: A Kinematic Point of View," ALEPH internal report ALEPH 2000-087 (2000, unpublished).

[60] C. Loomis and M. Kado, "Preliminary Studies and New Preselection for the 189 GeV $H\nu\bar{\nu}$ Search," ALEPH internal report ALEPH 98-087 (1998, unpublished).

[61] W. Bartel *et al.* (JADE Collaboration), Z. Phys. **C33** (1986) 23.

[62] J. Kile and M. Kado, "New $H\nu\bar{\nu}$ selection with Neural Networks," ALEPH internal report ALEPH 2000-048 (2000, unpublished).

[63] J. Boucrot *et al.*, "Search for Neutral Higgs at LEP 200" in *Proceedings of ECFA Workshop on LEP200*, eds. A. Böhm and W. Hoogland, CERN Report 87-08 (1987), p. 312.

[64] T.C. Greening, Ph.D. dissertation, University of Wisconsin-Madison (1999).

[65] P. Janot and F. Le Diberder, Nucl. Instrum. Methods **A411** (1998) 449.

[66] A. Read, "Modified Frequentist Analysis of Search Results (The CL_s Method)," in *Workshop on Confidence Limits*, eds. F. James, L. Lyons, Y. Perrin, CERN Yellow Report 2000-005 (2000), p. 81.

[67] S.S. Wilks, *Mathematical Statistics*, (Princeton University Press, Princeton, NJ, 1946).

[68] K.S. Cranmer, Comput. Phys. Commun. **136** (2001) 198.

[69] A.L. Read, Nucl. Instrum. Methods **A425** (1999) 357.

[70] H. Hu and J. Nielsen, "Analytic Confidence Level Calculations Using the Likelihood Ratio and Fourier Transform," in *Workshop on Confidence Limits*, eds. F. James, L. Lyons, Y. Perrin, CERN Yellow Report 2000-005 (2000), p. 109.

[71] ALEPH, DELPHI, L3, and OPAL Collaborations (LEP working group for Higgs boson searches), "Searches for Higgs bosons: Preliminary combined results using LEP data collected at energies up to 209 GeV," ALEPH 2000-074 CONF 2000-051, DELPHI 2000-158 CONF 447, L3 Note 2600, OPAL Technical Note TN661 (2000, unpublished).

[72] S. Jin and P. McNamara, Nucl. Instrum. Methods **A462** (2001) 561.

[73] O. Helene, Nucl. Instrum. Methods **212** (1983) 319.

[74] B.P. Roe, *Probability and Statistics in Experimental Physics*, (Springer-Verlag, New York, 1992).

[75] R.D. Cousins and V.L. Highland, Nucl. Instrum. Methods **A320** (1992) 331.

[76] LEP Higgs Working Group, "Standard Model Higgs Boson at LEP: Results with the 2000 Data, Request for Running in 2001." `http://lephiggs.web.cern.ch/LEPHIGGS/papers/doc_nov3_2000.ps`

[77] P. Igo-Kemenes, "Status of Higgs Boson Searches," presentation to the CERN LEP Experiments Committee, Nov. 3, 2000 (unpublished).

[78] J. Goldstein *et al.*, Phys. Rev. Lett. **86** (2001) 1694.

[79] M. Carena *et al.*, "Report of the Tevatron Higgs Working Group," FERMILAB Conf 00/279 T, `hep-ph/0010338` (2000).

[80] ATLAS Collaboration, "ATLAS Detector and Physics Performance Design Report," LHCC 99-14/15 (1999, unpublished).

[81] CMS Collaboration, "CMS Technical Proposal," CERN/LHCC 94-38 (1994, unpublished).

[82] F. Gianotti (private communication).